The Effects of Mechanical Coupling on the Electrical Impedance of MEMS Resonators for UHF Filter Applications.

by

Luke A. Hohreiter

B.S., Mechanical Engineering
United States Air Force Academy, 2002

Submitted to the Department of Mechanical Engineering

in Partial Fulfillment of the Requirements for the Degree of

Master of Science in Mechanical Engineering

at the

Massachusetts Institute of Technology

June 2004

Signature of Author_____

Department of Mechanical Engineering
May 7, 2004

Certified by_____

Amy E. Duwel
Charles Stark Draper Laboratory
Thesis Supervisor

Certified by_____

Gang Chen
Associate Professor of Mechanical Engineering
Thesis Advisor

Accepted by _____

Ain A. Sonin
Chairman, Committee on Graduate Studies
Department of Mechanical Engineering
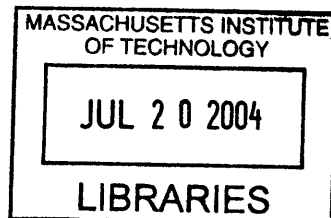
BARKER

The Effects of Mechanical Coupling on the Electrical Impedance of MEMS Resonators for UHF Filter Applications

by

Luke A. Hohreiter

Submitted to the Department of Mechanical Engineering
on May 7, 2004, in Partial Fulfillment of the Requirements for the
Degree of Master of Science in Mechanical Engineering

Abstract

This thesis presents finite elements based simulations of electromechanical transfer functions for resonator and filter geometries. These Finite Element Analysis (FEA) simulations are performed using the ANSYS software and demonstrate the significance of mechanical coupling between MEMS longitudinal-mode bar (L-Bar) resonators. An analytical model and equivalent circuit are derived for a single L-Bar resonator. The analytical derivation is validated with an FEA model having the same material parameters and boundary conditions. The center frequency and resonant impedance produced by the FEA model are within 1% of the analytical values. A boundary condition study is undertaken to determine the sensitivity of the L-Bar resonator model to changes in the peripheral geometry and displacement constraints. A comparison of FEA results indicates that a simple resonator model with only tether supports yields impedance and center frequency values comparable to those of more complex geometries. When compared to initial experimental results from an actual resonator, the simulated electrical output corresponds well to the actual transfer function. This study also introduces a method for calculating the parameters of the resonator's equivalent circuit model from simulated (or measured) transfer function data. The method is tested on simulation data for which a mechanical Quality factor is designated. Comparing the prescribed mechanical Q to the extracted circuit Q provides a consistency check for the technique. The parameter extraction technique is a useful first attempt to devise a comprehensive method for determining circuit parameters that will reliably reproduce the transfer function of an actual resonator. Finally, a new resonator topology is presented that employs mechanical coupling between L-Bar resonators to improve upon the output of a single bar and create alternative configurations for filter design at Draper. The new coupled bar geometry can be configured as either a single-port resonator or a multi-port filter. The benefits of mechanical coupling are investigated for both configurations. In discussion of future work, optimized filter parameters are presented, along with suggestions for achieving these values.

Technical Supervisor: Amy E. Duwel
Title: MEMS Group Leader

Thesis Supervisor: Gang Chen
Title: Associate Professor of Mechanical Engineering

[THIS PAGE INTENTIONALLY LEFT BLANK]

Acknowledgements

[THIS PAGE INTENTIONALLY LEFT BLANK]

Contents

List of Figures

List of Tables

[THIS PAGE INTENTIONALLY LEFT BLANK]

Chapter 1

Introduction and Qualitative Analysis of Resonator

1.1 Introduction

The MEMS group at Draper Laboratory has developed a longitudinal-mode bar (L-Bar) resonator for use in wireless communication applications such as ultra-high frequency (UHF, 300 MHz – 3 GHz) filters and oscillators [5]. The L-Bar resonator is designed to be the primary component in an RF channel-select filter comprised of MEMS parts and fully integrated on a CMOS chip [9]. The purpose of this study is to present simulated electromechanical transfer functions of individual resonators as well as filters. Furthermore, this work also investigates mechanically coupled resonators and their use in filter designs.

First, in the remaining sections of Ch. 1, background for coupled MEMS resonators is briefly reviewed. A qualitative investigation of Draper's L-Bar resonator is also presented. This investigation introduces the single and coupled model geometries, describing their characteristic mode shapes and frequency range. Ch. 2 focuses on an analytical derivation of the resonator bar's mechanical behavior and electrical transfer function. Ch. 3 continues the quantitative analysis by comparing the analytical model to an equivalent Finite Element Analysis (FEA) geometry. Transfer functions are obtained for both models and the results are discussed. In Ch. 4, a boundary condition study is undertaken to qualify the FEA model presented in Ch. 1. The primary objective of this case study is to determine the range of error associated with neglecting the full substrate and packaging in the electromechanical simulations.

Ch. 5 introduces a method for extracting the circuit model parameters of a resonator from measured data and tests the method on various simulated transfer functions. Ch. 6 introduces and expounds upon a new resonator topology that utilizes the benefits of mechanical coupling to

produce a more advantageous filter configuration. Finally, Ch. 7 provides a summary of the work presented in the study including conclusions and suggestions for future filter design.

1.2 Other Work in Coupled MEMS Resonators

The work of other groups on coupled MEMS resonators is reviewed now in order to formulate a context for the contributions of this thesis. Many different coupled resonator topologies have been developed for use in MEMS filter design. These topologies are characterized by a wide variety of coupling mechanisms and operational frequency ranges. Each design is electrically driven by either capacitive or piezoelectric actuation. This section presents four examples of actual coupled MEMS resonator configurations, followed by a brief comparison to Draper's design.

1.2.1 Mechanically Corner-Coupled, Square Microresonator

The corner-coupled microresonator is presented in [6] primarily as a filter component that offers a reduced motional resistance as compared to a stand-alone square resonator. The resistance of the device is decreased by placing the mechanically coupled resonators in a parallel electrical configuration, thus creating multiple paths for current to flow. As the design name indicates, the coupling mechanism of the device is characterized by short, stiff stubs that connect the individual microresonators at their corners. The primary design in [6] is comprised of a parallel array of three corner-coupled resonators actuated and sensed capacitively. Rigid mechanical connections are used between the resonators in order to separate the primary flexural modes as much as possible. Furthermore, unwanted filter modes are then "suppressed by imposing properly phased ac forces on constituent resonators [to] emphasize phasings associated with [the] desired mode, while counteracting all others" [6]. For this topology, the desired mode is that characterized by an in-phase displacement of all the resonators. In the ideal case, when all the coupled resonators have the same (uncoupled) resonance frequency, the in-phase mode is well isolated and the other primary modes are suppressed. However, with as small as a .01%

14

mismatch in uncoupled resonant frequency, simulations show that the combined output of the parallel resonators is compromised significantly.

A center frequency of approximately 64 MHz and Quality factor of 10,900 is measured for a three-resonator coupled configuration designed and fabricated in $POCl_3$-doped polysilicon. Furthermore, with a 52 V dc-bias applied to the device, the transmission of the in-phase mode is approximately -47 dB, corresponding to a measured resonant impedance of 7.7 kΩ. Each of the constituent resonators has square dimensions with a side length of 16 μm and a thickness of 2 μm. The resonators are anchored at the center and capacitively actuated by triangular electrodes positioned .18 μm below the array.

1.2.2 Programmable MEMS Bandpass Filter

The next example is a folded-beam comb-transduced coupled resonator that employs external control voltage to "vary spring constants [and] obtain a bandpass filter whose center frequency and bandwidth are programmable" [3]. The folded-beam resonators are connected by a square-truss coupling spring and the device vibrates parallel to the substrate. The resonators are comprised of polycrystalline silicon. Key dimensional parameters include the following: 2 μm thick structural layer, coupling beam length of 175 μm, and tuning finger gap spacing of 2 μm. Using a 10 V dc-bias and a Q of 20, an FEA simulation yields a center frequency of approximately 21 kHz with an insertion loss of about 2 dB. The source and load resistances used in the simulation are not specified.

The filter is capacitively actuated and tuned using a comb-configuration of parallel plate structures. As a result, the filter center frequency and the mechanical coupling between the resonators can be varied by modifying the tuning finger overlap capacitance. For no dc-bias applied to the filter, the nominal bandwidth is 1.05 kHz. For an 11 V range in tuning voltage, theoretical calculations and FEA simulations show that the bandwidth (i.e. coupling) increases approximately 14% to a value of 1.2 kHz. Furthermore, for a 16 V range, about a 1.3% tuning range is achieved for the center frequency.

15

1.2.3 Two-Resonator High Frequency (HF) Micromechanical Filter

In [1], Nguyen introduces a coupled (HF) flexural-mode micromechanical filter. The filter is comprised of two clamped-clamped beam resonators coupled mechanically by a soft spring. As in the other designs, the filter is capacitively actuated and sensed. "Conductive strips underlie the central regions of each resonator and serve as capacitive transducer electrodes positioned to induce resonator vibration in a direction perpendicular to the substrate" [1]. For resonator beams 40.8 μm in length, the operational frequency of the filter is 8.71 MHz. The length of the coupling spring is maintained at the calculated quarter-wavelength value, and the mechanical coupling is varied by changing the location of the spring connection along the resonator beams. "Low-velocity" coupling is used to achieve small percent bandwidths while maintaining reasonable coupling spring dimensions. This "low-velocity" method is accomplished by moving the coupling location away from the center of the beam (i.e. point of highest velocity) and closer to the anchors.

For an "8.71 MHz low velocity, coupled micromechanical filter constructed of phosphorous-doped polysilicon," a percent bandwidth of .23% is achieved with an insertion loss less than 2 dB and passband rejection exceeding 35 dB. It is important to note, however, that these results are obtained using a dc-bias of 35 V and source/load resistor values on the order of 12 kΩ.

1.2.4 Bulk Acoustic Wave (BAW) Coupled Resonator Filter

Bulk acoustic wave devices such as the stacked crystal filter (SCF) are advantageous because of their high operational frequency range and wide bandwidth capabilities. In [7], Lakin presents results for both a conventional SCF and a new BAW device referred to as a Coupled Resonator Filter (CRF). A CRF has virtually the same design as a typical SCF, but is amended to include a "sequence of nominal quarter wavelength thick layers whose transmission response is designed to allow optimum resonator coupling" [7]. Both the SCF and CRF are fabricated upon "a limited bandwidth reflector array that attenuates spurious responses" [8] occurring above and below the primary thickness mode. The tight mechanical coupling between resonators in a SCF design restricts the realizable filter bandwidth by limiting the effectiveness of the piezoelectric

transducer. Using electrical means to decrease the coupling between the resonators are advantageous in certain applications, but such methods normally require a larger filter size than is desirable for fully integrated designs [8]. As a result, [7] suggests the implementation of layers between the resonators to adjust the acoustic coupling and control the filter bandwidth.

Experimental results are presented for a CRF made of Aluminum Nitride (AlN) and designed to operate at resonant frequency of 1960 MHz. The 3 dB bandwidth of the device is about 67 MHz with an insertion loss of 2.8 dB. This bandwidth is 3.6% of the center frequency, making it suitable for RF communication applications. The out of band attenuation is approximately 40 dB. Adjustments to the thickness of the electrodes can be employed to shift the operational frequency, while bandwidth can be manipulated by modifying the number and thickness of the coupling layers.

1.2.5 Draper's Coupled Resonator Design

The coupled resonator design being developed at Draper Laboratory has a monolithic crystal filter structure. The individual resonator bars are coupled by tethers and the device is driven by piezoelectric actuation. Like the design in [7], Draper's coupled resonator exploits the properties of bulk acoustic waves propagating through the material. However, rather than thickness modes, these waves produce longitudinal displacement of the bar transverse to the thickness. Coupling in the device can be varied by changing the tether dimensions (i.e. length, width, etc). The resonator bars and support tethers are configured in a sandwich orientation of metal-piezoelectric-metal. The piezoelectric material is Aluminum Nitride, and the two metal layers are Nickel and Molybdenum.

Experimental results for Draper's coupled resonator are not yet available, but finite element simulations indicate that the device's operational frequency is in the UHF range, significantly higher than the other designs presented. Furthermore, simulated transfer functions of FEA and circuit models show that filter bandwidth could be tunable in a range of .25-1.5 % of the center frequency. Based on testing of single resonators, the Quality factor of initial coupled designs is

not expected to be within the desired range (i.e. 10^4). However, Q values of 10^4 should be achievable in future designs

Assuming the desired resonator Q can be obtained, Draper's coupled device offers significant advantages over the other designs presented in this section. First, with Q values of 10^4, Draper's coupled resonator can achieve resonant impedances below 200 Ω, making impedance matching with front end circuit elements feasible. Secondly, because the device uses piezoelectric actuation, no dc-bias is required to achieve reduced impedance at resonance. Furthermore, Draper's design operates under linear conditions and thus, has the capability to handle a wide range of power inputs. As a result, the selectivity (or Q) versus power tradeoff characterizing many other MEMS devices is not applicable to Draper's design. Finally, because the device is fabricated using photolithography and laser trimming, frequency tuning of the individual resonators is greatly facilitated.

1.3 Single Mechanical Modes

1.3.1 Description of Bar Geometry

While a variety of resonator topologies are being fabricated and tested, this study is limited primarily to a resonator bar geometry having a length of 6 μm. A resonator of this size possesses a longitudinal natural frequency on the order of 1 GHz, making it a suitable geometry for UHF filter applications. The full set of physical dimensions for the resonator is the following: length = 6 μm, width = 3 μm, and thickness = .5 μm. The also includes support tethers that connect the resonator to the substrate. Figure 1.1 shows the initial model geometry.
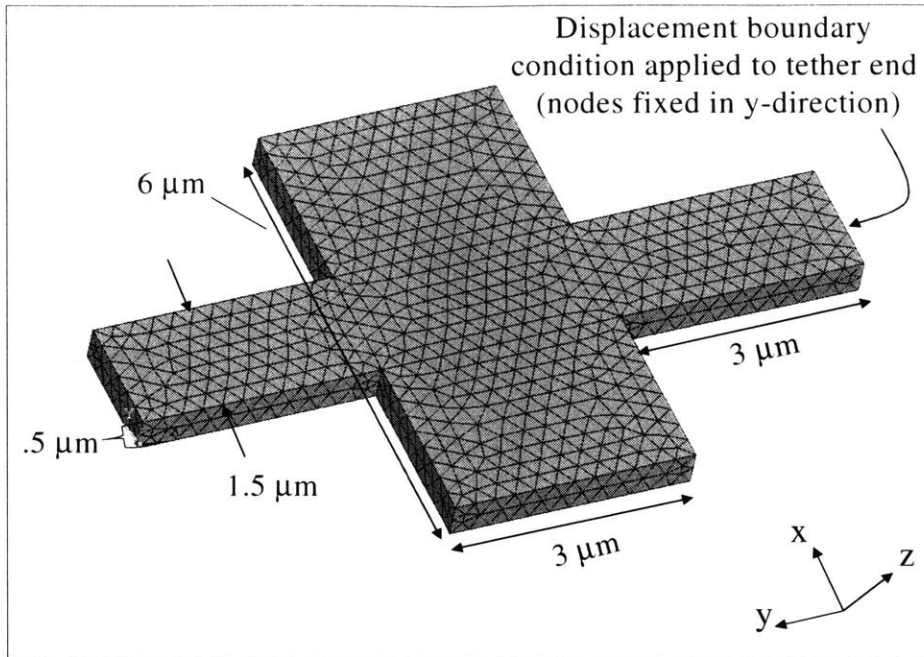
Figure 1.1: Resonator geometry with tether supports. Cartesian coordinate system (x, y, z) is used in the figure. These coordinates are analogous to the unit vectors (x_1, x_2, and x_3) used in later sections.

Based on previous analysis and general engineering guidelines for the construction of resonator geometries, a length of 3 μm is initially chosen for the tether supports. This length is measured from the edge of the resonator to the end of the tether as shown in the figure above. For a resonator topology of this size, the tether length of 3 μm corresponds approximately to a quarter wavelength at the device's longitudinal natural frequency.

1.3.2 Longitudinal Mode Shape and Frequency

In order to gain insight into the mode shapes and modal frequencies associated with the L-Bar resonator, a qualitative investigation using FEA methods is performed on the geometry of Fig. 1.1. The specific goal of this preliminary analysis is to obtain information about the motion and general frequency range of the longitudinal mode. An actual resonator has multiple layers of material. However, to simplify the modeling process, the FEA geometry is comprised entirely of Aluminum Nitride (AlN). The metal electrodes used to actuate the device have been neglected. As shown in Fig. 1.1, the boundary conditions are applied to the cross-sectional face of the tether

ends and mimic an infinite condition. The modal analysis for the single mechanical model produces a longitudinal center frequency of approximately 840 MHz. Figure 1.2 illustrates the general motion of the longitudinal mode shape of the resonator.
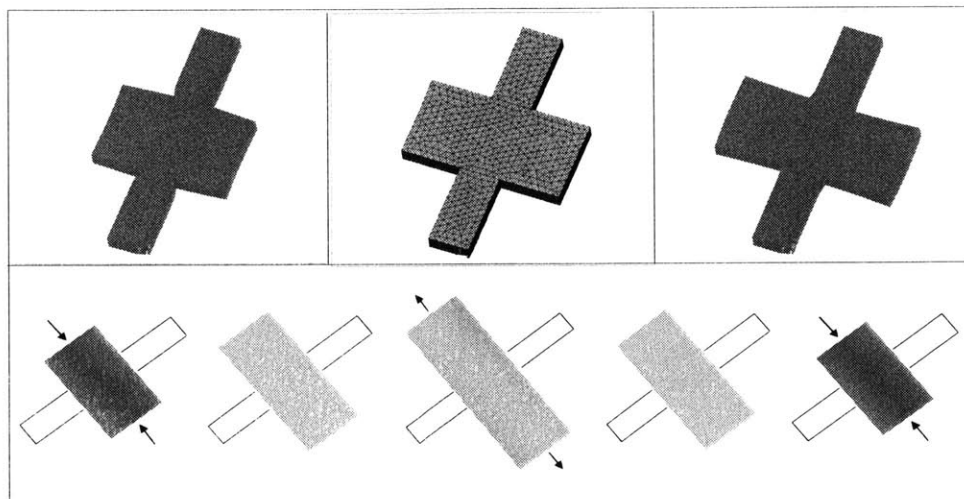
Figure 1.2: Stages of longitudinal mode shape. Top row: steps of FEA animation; Bottom row: 2-D illustration of one longitudinal cycle

From left to right, Fig. 1.2 details the variation in time of the longitudinal mode shape. At this lowest order longitudinal mode, a node of zero displacement forms at the middle of the bar and the structure compresses and stretches sinusoidally about this point. With the general mode shape and center frequency range of the single resonator bar established, we can begin to investigate combining, or coupling, individual bars to create various filter topologies.

1.4 Coupled Mechanical Modes

1.4.1 Coupled Resonator Theory

In the electrical domain, a single resonator bar with a metal-piezoelectric-metal configuration behaves like a capacitor over a wide band of frequencies. However, at the longitudinal resonance frequency, its impedance characteristic departs from that of a normal passive circuit element. The mechanical resonance dominates its electrical response close to the natural

frequency, resulting in a significant decrease in the bar's impedance over this range. This impedance drop corresponds to a large accumulation of charge on the metal electrodes, and because the forcing function is sinusoidal, current is produced in the device.

When single resonators are combined to create a filter, the impedance drops of the resonators must occur simultaneously for the filter to function properly. By assuming that the impedance drop of the electrically coupled resonators will coincide precisely, the designer presupposes that the fabrication processes being employed are virtually ideal. However, creating two identical resonators is virtually impossible due to limitations on the accuracy of current fabrication methods. These methods, while relatively advanced, do not possess the precision needed to guarantee that tolerance errors will not occur. Presently, the only way to ensure that the dual resonators have identical center frequencies and matching resonant responses is to couple them mechanically as well as electrically. If the structures are not coupled mechanically, even an extremely small error in fabrication can cause a significant discrepancy between the individual resonant frequencies.

For this reason, it is important to gain intuition for the sensitivity of longitudinal center frequency to variations in resonator length. If the effect is large, meaning that a small variation in resonator length produces a large shift in the center frequency of the longitudinal mode, then the need for mechanically coupled resonators is justified. In order to observe this "sensitivity," a set of mechanical simulations is performed in which the length of the resonator in Fig. 1.1 is varied to mimic the effect of fabrication errors. Furthermore, a graph showing the difference in center frequency values is shown as Figure 1.3.

Center Frequency vs. Resonator Length
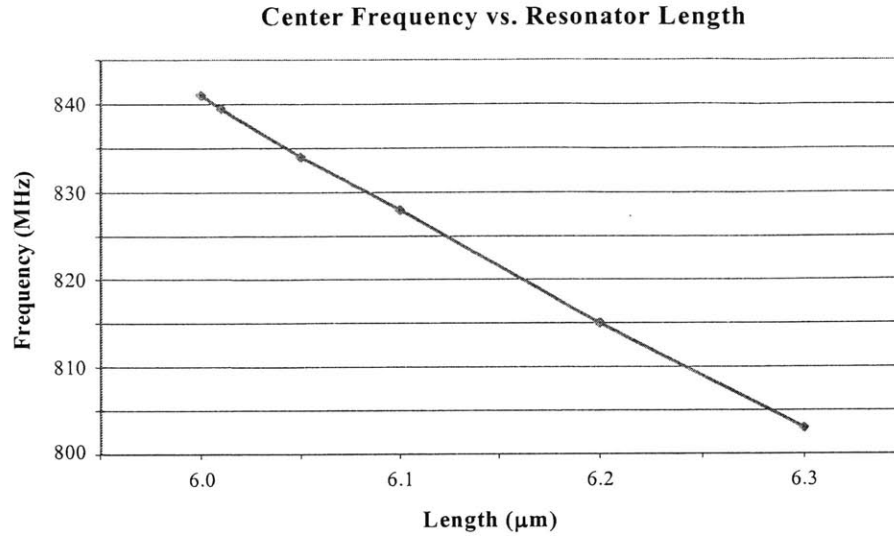
Figure 1.3: Graph of center frequency change with variation of resonator length (μm)

The plot illustrates that, as resonator length varies, the center frequency shifts rapidly away from the standard value associated with the 6 μm bar. From the graph, we observe that with a discrepancy in length as small as a .1 μm, the center frequency can be expected to shift about 1.5 % from its original value. This discrepancy value is significant because it represents the approximate tolerance of current fabrication methods for the RF resonator. The frequency shift of 1.5% is important because the 3 dB bandwidth of a high Q (i.e. 10^4) MEMS resonator is typically on the order of kHz. A response bandwidth of this size is over a hundred times smaller than the MHz range shift associated with tolerance errors. This relationship indicates that with even the smallest fabrication error, the transfer function of a mechanically uncoupled filter will most likely show two distinct frequency responses in its impedance characteristic.

1.4.2 Effect of Frequency Shift on an Uncoupled Filter

Based on the sensitivity of center frequency to changes in resonator length, mechanical coupling of resonator pairs is crucial in MEMS filter design. For example, without mechanical coupling, the electrical output of a filter using parallel resonators breaks down quickly as resonant frequency mismatch increases. The objective of placing two resonators electrically in parallel is to decrease the insertion loss of the filter component by increasing the paths through which current can flow. Once again, this concept holds only if the resonant frequencies of the

22

combined resonators are matched. For non-identical resonators in parallel, the impedance characteristics would be observed electrically as two distinct passbands in the frequency domain, thus compromising the filter's transmission. Consequently, from a qualitative standpoint, coupling individual resonators mechanically creates a filter component which is potentially more robust to fabrication errors. In later sections, both FEA and circuit simulation data are provided to illustrate the difference in robustness between the coupled and uncoupled filter topologies.

1.4.3 Coupled Resonator Geometry

With the importance of a coupled resonator configuration established, the qualitative investigation will now shift focus toward gaining insight into the mechanical behavior of such a device. Like a single resonator, the basic geometry of the coupled bar is characterized by the resonators and their supporting tethers. The primary modification associated with the mechanically connected geometry is the presence of a coupling tether that physically joins the resonators, creating a new single structure. This modified geometry is shown in Figure 1.4.
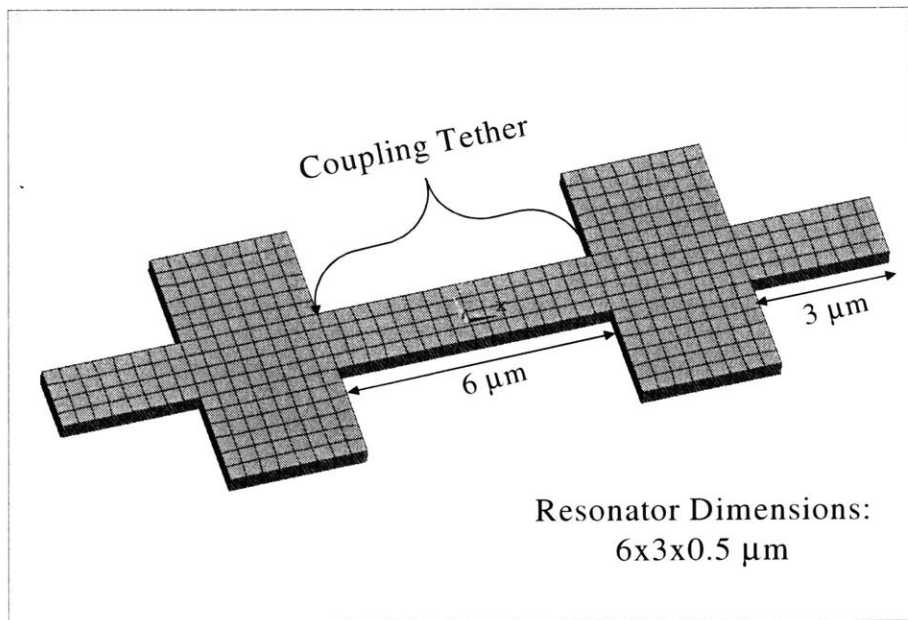
Figure 1.4: Mechanically coupled resonator bar.

In order to maintain continuity with the single resonator model, the outside tethers of the coupled design are also 3 μm. Maintaining a constant outside tether length helps to ensure that the qualitative case study does not increase in complexity too rapidly. Thus, while the value for the outside tether length has not been thoroughly optimized, a length of 3 μm is chosen so that key features of the single and coupled geometries correspond to each other. The coupling tether, labeled in the Fig. 1.4, has a length of 6 μm, an initial value chosen based on symmetry. A key modification made to the coupled model is the change in mesh characteristics from tetrahedral to block elements. For a simple rectangular geometry, block elements, having a sufficient mesh density, tend to solve such a model more efficiently and with comparable accuracy.

1.4.4 In-Phase and Out-of-Phase Longitudinal Modes

Because the coupled model is comprised of two resonators, which both contribute to the overall motion of the system, there is a need to address two distinct kinds of longitudinal modes – in-phase and 180 degrees out-of-phase. While the center frequency of a coupled model is largely dependent on its material properties (i.e. density and stiffness), the mode shapes of the two primary longitudinal modes depend mainly on the amount of coupling between the resonators. An effective method for varying the coupling is to modify the length of the coupling tether.

In order to investigate the sensitivity of the mode shapes to changes in coupling tether length, a series of FEA simulations are performed and the resulting mode shapes are observed. Sensitivity refers to the amount the mode shapes differ from the longitudinal motion of a single bar as a result of a change in coupling tether length. Furthermore, a "clean" mode shape will be defined as one which exhibits displacement primarily along the length of the resonator, with no flexural or twisting components present in the overall deformation. Figure 1.5 shows in-phase and out-of-phase mode shapes for coupling tether lengths of 3, 6, and 9 μm.
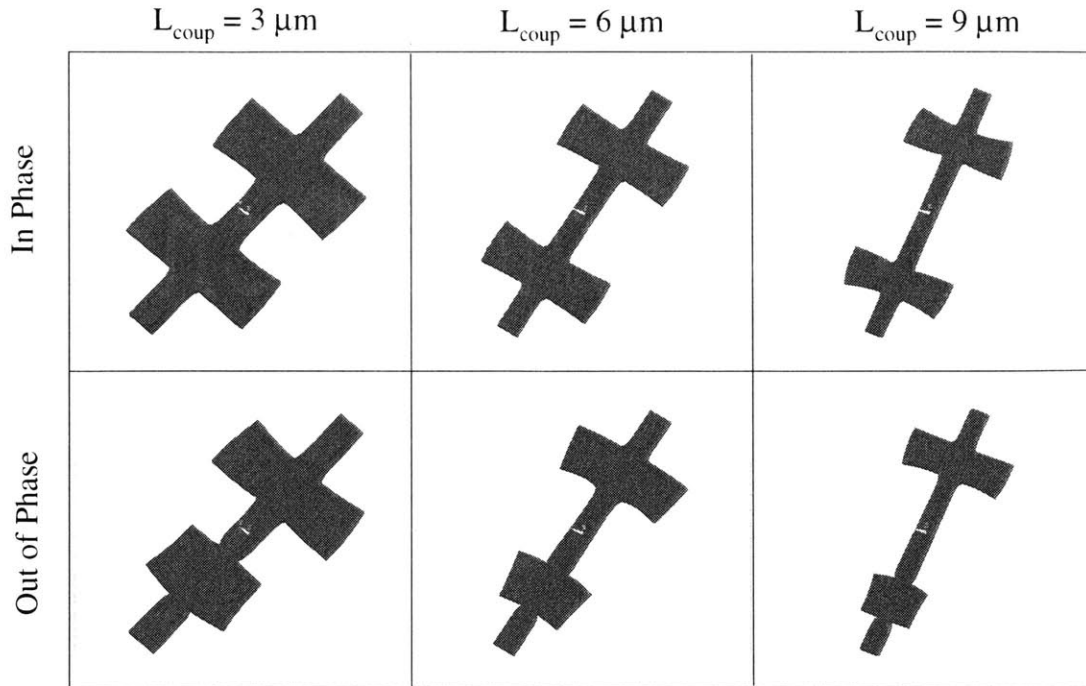
Figure 1.5: In-phase and out-of-phase mode shapes (Top row: In, Bottom row: Out)

Looking first at the top row of illustrations in Fig. 1.5, we observe that the resonator with a coupling (or inside) tether length of 6 μm has the cleanest in-phase mode shape. As the coupling tether length departs from a value of 6 μm, we observe a more polluted in-phase mode in which the longitudinal motion is mixed with an in-plane twisting. This twisting is undesirable for any coupled configuration, but particularly adverse for a parallel resonator topology. In theory, additional twisting or flexing will cancel a portion of the total charge accumulated on the electrode surface. A cancellation of charge will then, in turn, decrease the filter response at the in-phase resonant frequency. If the response of the device degrades, the signal passed by the filter decreases, thus compromising its effectiveness.

The illustrations in the bottom row of Fig. 1.5 indicate that, regardless of the coupling tether length, a certain degree of twisting will always be present in the out-of-phase mode shape. However, because the parallel configuration suppresses the electrical contribution of this mode, the extra motion is not as detrimental to the filter transfer function. In the out-of-phase mode, as one resonator stretches, the other compresses, and thus, the net charge accumulated on the electrodes is minimal. In the ideal case, the net charge produced by the out-of-phase mode is

zero. With a twisting component added, the cancellation may not be complete, but any net charge produced will most likely be negligible. With respect to a series or multi-port circuit topology, little can be determined about the effect of these non-idealities from a purely qualitative analysis. A quantitative, electromechanical analysis using piezoelectric finite elements is necessary to confirm their impact.

Chapter 2

Analytical Derivation: Single Electromechanical Model

2.1 Constitutive Equations

All modal and harmonic analyses in this study are performed using the FEA software, ANSYS [see Appendix]. ANSYS is employed because it possesses a group of "coupled field" element types specifically designed to simulate the electromechanical behavior of a piezoelectric material. Although ANSYS automatically solves the piezoelectric constitutive equations which characterize the behavior of AlN, it is important to understand how a corresponding mathematical model is set up, constrained and solved. This analytical model then becomes a benchmark for a full finite elements study. The following analysis corresponds closely to the derivation included in [2] and is included in this study for completeness.

The general constitutive equations for a piezoelectric material are written in matrix form below [2].

$$
\begin{bmatrix} T_1 \\ T_2 \\ T_3 \\ T_4 \\ T_5 \\ T_6 \end{bmatrix} = \begin{bmatrix} c_{11} & c_{12} & c_{13} & 0 & 0 & 0 \\ c_{21} & c_{22} & c_{23} & 0 & 0 & 0 \\ c_{31} & c_{32} & c_{33} & 0 & 0 & 0 \\ 0 & 0 & 0 & c_{44} & 0 & 0 \\ 0 & 0 & 0 & 0 & c_{55} & 0 \\ 0 & 0 & 0 & 0 & 0 & c_{66} \end{bmatrix} \begin{bmatrix} S_1 \\ S_2 \\ S_3 \\ S_4 \\ S_5 \\ S_6 \end{bmatrix} - \begin{bmatrix} 0 & 0 & e_{31} \\ 0 & 0 & e_{32} \\ 0 & 0 & e_{33} \\ 0 & e_{24} & 0 \\ e_{15} & 0 & 0 \\ 0 & 0 & 0 \end{bmatrix} \begin{bmatrix} E_1 \\ E_2 \\ E_3 \end{bmatrix} \qquad (2.1.1)
$$

$$\begin{bmatrix} D_1 \\ D_2 \\ D_3 \end{bmatrix} = \begin{bmatrix} 0 & 0 & 0 & 0 & e_{15} & 0 \\ 0 & 0 & 0 & e_{24} & 0 & 0 \\ e_{31} & e_{32} & e_{33} & 0 & 0 & 0 \end{bmatrix} \begin{bmatrix} S_1 \\ S_2 \\ S_3 \\ S_4 \\ S_5 \\ S_6 \end{bmatrix} + \begin{bmatrix} \varepsilon_{11} & 0 & 0 \\ 0 & \varepsilon_{22} & 0 \\ 0 & 0 & \varepsilon_{33} \end{bmatrix} \begin{bmatrix} E_1 \\ E_2 \\ E_3 \end{bmatrix} \qquad (2.1.2)$$

where $[T]$ = stress matrix, $[c]$ = stiffness matrix, $[S]$ = strain matrix, $[e]$ = piezoelectric constant matrix, $[E]$ = electric field matrix, $[D]$ = electrical displacement matrix, and $[\varepsilon]$ = dielectric constant matrix.

Eq. (2.1.1) illustrates the relationship between stress, strain and electric field, while (2.1.2) shows the connection between electrical displacement (i.e. accumulation of charge on the electrodes), strain and electric field. The $[e]$ matrix holds the piezoelectric constants which mathematically couple stress in the structure to the output charge. For Draper's L-Bar resonator, the primary independent variables are displacement and electric potential. The displacement of the resonator determines the stress and strain in the bar. When the resonator vibrates at its longitudinal natural frequency, the longitudinal displacement of the bar is large, causing an increase in stress and strain. For a piezoelectric material such as AlN, the amplified displacement also causes a significant accumulation of charge on the metal electrodes lining the top and bottom surfaces of the resonator. When the displacement varies sinusoidally with time, an output current is produced at resonance, and the resonator's impedance decreases. In order to make the resonator vibrate at its resonant frequency, an AC voltage is applied to the bar. If the displacement and potential are assumed to have the same sinusoidal variation (e.g. $e^{-i\omega t}$), the time dependence falls out of the constitutive equations and the problem becomes essentially static in nature. In order to transform (2.1.1) and (2.1.2) into the desired form, with stress and charge written in terms of displacements, u_i, and potential,Φ, the following relationships are established.

$$S_{ij} = \frac{1}{2}\left(\frac{\partial u_i}{\partial x_j} + \frac{\partial u_j}{\partial x_i} \right) = \frac{1}{2}\left(u_{i,j} + u_{j,i} \right) \qquad (2.1.3)$$

$S_1 = S_{11};\quad S_2 = S_{22};\quad S_3 = S_{33};$

$$S_4 = 2S_{23} = 2S_{32}; \quad S_5 = 2S_{13} = 2S_{31}; \quad S_6 = 2S_{12} = 2S_{21}$$

and

$$E_1 = -\frac{\partial \Phi}{\partial x_1}; \quad E_2 = -\frac{\partial \Phi}{\partial x_2}; \quad E_3 = -\frac{\partial \Phi}{\partial x_3} \qquad (2.1.4)$$

Substituting (2.1.3) and (2.1.4) back into the constitutive equations gives,

$$
\begin{bmatrix} T_1 \\ T_2 \\ T_3 \\ T_4 \\ T_5 \\ T_6 \end{bmatrix}
=
\begin{bmatrix}
c_{11} & c_{12} & c_{13} & 0 & 0 & 0 \\
c_{21} & c_{22} & c_{23} & 0 & 0 & 0 \\
c_{31} & c_{32} & c_{33} & 0 & 0 & 0 \\
0 & 0 & 0 & c_{44} & 0 & 0 \\
0 & 0 & 0 & 0 & c_{55} & 0 \\
0 & 0 & 0 & 0 & 0 & c_{66}
\end{bmatrix}
\begin{bmatrix}
u_{1,1} \\ u_{2,2} \\ u_{3,3} \\ u_{2,3}+u_{3,2} \\ u_{1,3}+u_{3,1} \\ u_{1,2}+u_{2,1}
\end{bmatrix}
+
\begin{bmatrix}
0 & 0 & e_{31} \\
0 & 0 & e_{32} \\
0 & 0 & e_{33} \\
0 & e_{24} & 0 \\
e_{15} & 0 & 0 \\
0 & 0 & 0
\end{bmatrix}
\begin{bmatrix}
\dfrac{\partial \Phi}{\partial x_1} \\ \dfrac{\partial \Phi}{\partial x_2} \\ \dfrac{\partial \Phi}{\partial x_3}
\end{bmatrix}
\qquad (2.1.5)
$$

$$
\begin{bmatrix} D_1 \\ D_2 \\ D_3 \end{bmatrix}
=
\begin{bmatrix}
0 & 0 & 0 & 0 & e_{15} & 0 \\
0 & 0 & 0 & e_{24} & 0 & 0 \\
e_{31} & e_{32} & e_{33} & 0 & 0 & 0
\end{bmatrix}
\begin{pmatrix}
u_{1,1} \\ u_{2,2} \\ u_{3,3} \\ u_{2,3}+u_{3,2} \\ u_{1,3}+u_{3,1} \\ u_{1,2}+u_{2,1}
\end{pmatrix}
-
\begin{bmatrix}
\varepsilon_{11} & 0 & 0 \\
0 & \varepsilon_{22} & 0 \\
0 & 0 & \varepsilon_{33}
\end{bmatrix}
\begin{bmatrix}
\dfrac{\partial \Phi}{\partial x_1} \\ \dfrac{\partial \Phi}{\partial x_2} \\ \dfrac{\partial \Phi}{\partial x_3}
\end{bmatrix}
\qquad (2.1.6)
$$

Utilizing (2.1.5) and (2.1.6) as a foundation, it is possible to derive the electrical transfer characteristics of the L-Bar resonator. First, force balance is applied to the stress-strain relation of (2.1.5) in order to determine the acoustic wave equation for the structure. Furthermore, because longitudinal waves in the x-direction (along the length of the resonator) are of interest, assumptions related to the motion of the bar and the boundary conditions are made to simplify the analysis. Secondly, a modified Laplace's equation is derived from the charge-potential relation of (2.1.6). The wave equation combined with the modified Laplace's equation represents a set of coupled equations describing the electromechanical behavior of the resonator. The solution to the wave equation is determined by the magnitude and frequency of the electric

potential applied to the bar. Furthermore, the mechanical displacement described by the wave equation drives the electric potential generated in the piezoelectric material. In most cases, the fully coupled equations cannot be solved analytically. However, useful results can be obtained by employing an iterative approach. This approach is characterized by one-way electromechanical coupling between the applied voltage and the bar's displacement. In other words, the effects of reverse coupling, which account for the influence of the mechanical displacement on the electric potential, are neglected, and simplified first order solutions are obtained [2].

2.2 Force Balance

Force balance is applied by setting the first spatial derivative of the stress defined in (2.1.5) equal to the bar's vibrational inertia, producing the following equation.

$$
\begin{bmatrix} \rho\ddot{u}_1 \\ \rho\ddot{u}_2 \\ \rho\ddot{u}_3 \end{bmatrix} = \begin{bmatrix} \dfrac{\partial}{\partial x_1} & 0 & 0 & 0 & \dfrac{\partial}{\partial x_3} & \dfrac{\partial}{\partial x_2} \\ 0 & \dfrac{\partial}{\partial x_2} & 0 & \dfrac{\partial}{\partial x_3} & 0 & \dfrac{\partial}{\partial x_1} \\ 0 & 0 & \dfrac{\partial}{\partial x_3} & \dfrac{\partial}{\partial x_2} & \dfrac{\partial}{\partial x_1} & 0 \end{bmatrix} \begin{pmatrix} T_1 \\ T_2 \\ T_3 \\ T_4 \\ T_5 \\ T_6 \end{pmatrix} \tag{2.2.1}
$$

Because the longitudinal mode is of interest, we assume that the above equation has no dependence on the lateral component (i.e. x_2 direction), and thus all displacements (u_2) and displacement gradients ($u_{i,2}$) in the x_2 direction are neglected. Applying these simplifications to (2.1.1), three stress equations remain.

$$
T_1 = c_{11}u_{1,1} + c_{13}u_{3,3} + e_{31}\Phi_{,3} \tag{2.2.2}
$$

$$
T_3 = c_{31}u_{1,1} + c_{33}u_{3,3} + e_{33}\Phi_{,3} \tag{2.2.3}
$$

$$
T_5 = c_{55}(u_{1,3} + u_{3,1}) + e_{15}\Phi_{,1} \tag{2.2.4}
$$

Applying a stress free boundary condition to the top and bottom faces of the bar and neglecting any x_1-x_3 shear components, the following must hold on the x_3 boundaries.

$$T_3 = 0 \text{ at } x_3 = \pm a$$

(2.2.5)

$$T_5 = 0 \text{ at } x_3 = \pm a$$

Furthermore, in order to focus on the lowest longitudinal modes, we assume the inertia in the x_3 direction to be approximately zero, expressed below as

$$\rho \ddot{u}_3 \approx 0$$

(2.2.6)

Utilizing the simplified conditions above and noting that the spatial derivatives of T_3 and T_5 at the boundaries are also zero, one force balance equation remains.

$$\rho \ddot{u}_1 = T_{1,1} = c_{11} u_{1,11} + c_{13} u_{3,31} + e_{31} \Phi_{,31} \quad \text{where } u_{i,ij} = \frac{\partial^2 u_i}{\partial x_i \partial x_j}$$

(2.2.7)

Using the stress relations established by (2.2.5) and solving for the $u_{3,3}$ component in (2.2.3), a relationship is obtained for the displacement gradients through the length and thickness of the bar.

$$u_{3,3} = -\frac{1}{c_{33}} [c_{31} u_{1,1} + e_{33} \Phi_{,3}]$$

(2.2.8)

Substituting (2.2.8) into (2.2.7), we obtain an equation for the longitudinal inertia in terms of the 2nd spatial derivatives of u_1 and Φ.

$$\rho \ddot{u}_1 = \left[c_{11} - \frac{c_{13}^2}{c_{33}} \right] u_{1,11} + \left[e_{31} - \frac{c_{13} e_{33}}{c_{33}} \right] \Phi_{,31}$$

(2.2.9)

31

Eq. (2.2.9) represents the acoustic wave equation for the longitudinal modes in the x_1 direction. The presence of the Φ term in the wave equation indicates that the displacement of the resonator is coupled to the electrostatic potential.

2.3 Maxwell's Equations

The general Maxwell equation (i.e. differential form of Gauss' Law for electricity) states that the divergence of electrical displacement through the surface of a material equals the free charge density within the material. Written symbolically, Gauss' Law is

$$\nabla \cdot D = \rho \tag{2.3.1}$$

where ρ = free charge density, and D = electrical displacement. For a linear isotropic dielectric D can be expressed as εE, where E is electric field and ε is the relative permittivity of the material. AlN is a good electrical insulator, thus the free charge density is assumed to be zero. Applying this approximation, (2.3.1) becomes

$$\nabla \cdot D = 0 \tag{2.3.2}$$

(2.3.2) is the electrostatic equation that will be coupled with the wave equation to obtain an electrical transfer function for the resonator. Substituting (2.1.2) into (2.3.2) and recalling that there is no x_2 dependence, we are left with the following two equations

$$D_1 = e_{15}(u_{1,3} + u_{3,1}) - \varepsilon_{11}\Phi_{,1} \tag{2.3.3}$$

$$D_3 = e_{31}u_{1,1} + e_{33}u_{3,3} - \varepsilon_{33}\Phi_{,3} \tag{2.3.4}$$

Again, applying the boundary conditions specified in (2.2.5) to (2.2.4), we define the counterpart of (2.2.8) as

$$u_{3,1} = -u_{1,3} - \frac{e_{15}}{c_{55}} \Phi_{,1}$$ (2.3.5)

Substituting the (2.2.8) and (2.3.5) into the electric displacement equations of (2.3.3) and (2.3.4), and applying the constitutive relation of (2.3.2), we arrive at a modified Laplacian equation relating the potential in the bar to the vibrational displacement. The displacement of the bar at resonance serves as the driving force for the resonator's electrical output. This relationship is stated as

$$\left[\varepsilon_{11} + \frac{e_{15}^2}{c_{55}} \right] \Phi_{,11} + \left[\varepsilon_{33} + \frac{e_{33}^2}{c_{33}} \right] \Phi_{,33} = \left[e_{31} - \frac{e_{33}c_{31}}{c_{33}} \right] u_{1,31}$$ (2.3.6)

2.4 Coupled Electromechanical System of Equations

The piezoelectric interaction between the applied potential and the displacement of the bar can be summarized by the following two coupled equations:

$$\rho \ddot{u}_1 - \left[c_{11} - \frac{c_{13}^2}{c_{33}} \right] u_{1,11} = \left[e_{31} - \frac{c_{13}e_{33}}{c_{33}} \right] \Phi_{,31}$$ (2.2.9)

$$\left[\varepsilon_{11} + \frac{e_{15}^2}{c_{55}} \right] \Phi_{,11} + \left[\varepsilon_{33} + \frac{e_{33}^2}{c_{33}} \right] \Phi_{,33} = \left[e_{31} - \frac{e_{33}c_{31}}{c_{33}} \right] u_{1,31}$$ (2.3.6)

The x_1-x_3 coupling denoted by the mixed partial derivatives of both displacement and potential terms (i.e. $u_{1,31}$ and $\Phi_{,31}$) creates difficulties when attempting to solve the system of equations simultaneously. As a result, an iterative approach employing certain assumptions to simplify the

problem is required to arrive at an analytical solution. Because the modified Laplacian relation described by (2.3.6) is a linear, non-homogeneous, 2nd order differential equation, the solution for the potential can be split up into two parts: homogeneous and non-homogeneous – which can then be solved separately. The solution for the potential will be written as

$$\Phi = \Phi^{BC} + \Phi''$$ (2.4.1)

Applying (2.4.1) to (2.2.9), we arrive at the separated form of the wave equation

$$\rho \ddot{u}_1 - \left[c_{11} - \frac{c_{13}^2}{c_{33}} \right] u_{1,11} = \left[e_{31} - \frac{c_{13} e_{33}}{c_{33}} \right] \left(\Phi^{BC} + \Phi'' \right)_{,31}$$ (2.4.2)

Taking the coefficients on the left hand side of (2.3.6) to be approximately equal and defining them as one effective value, ε_{eff}, the homogeneous equation can be stated as

$$\varepsilon_{eff} \nabla^2 \Phi^{BC} = 0$$ (2.4.3)

where Φ^{BC} represents the boundary condition contribution to the potential, assuming a voltage-biased system in which voltage inputs are applied on the boundary. The non-homogeneous, or particular solution, constitutes the driven contribution to the potential and has no boundary conditions associated with it. Once again, using an effective coefficient, the driven potential can be expressed as

$$\varepsilon_{eff} \nabla^2 \Phi'' = \left[e_{31} - \frac{e_{33} c_{31}}{c_{33}} \right] u_{1,31}$$ (2.4.4)

where $\Phi'' = 0$ on the boundary and is directly proportional to the product of the displacement, $u_{1,31}$, and its corresponding piezoelectric coefficients on the right hand side of the equation. With respect to the method of actuation – in this case, by AC voltage inputs – Φ^{BC} naturally represents the forward coupling of potential to displacement in the bar. With the boundary condition

34

contribution defined in this way, the driven contribution to the potential, Φ'', can then be defined as the reverse coupling between the voltage biased displacement and the additional potential it produces. Since Eq. (2.4.4) is a linear system driven by strain (derivatives of u_j), a proportional relationship exists between Φ'' and the displacement. Therefore, because the displacements in the bar are known to be small, the Φ'' potential produced by the piezoelectric response of the bar is also a small quantity. As a result, to first order, we neglect the reverse coupling contribution to the potential in the bar, realizing that it only produces a small change in the longitudinal natural frequency of the resonator. Applying this simplification, we are left with one-way coupling between the applied AC voltage on the boundary and the resulting sinusoidal displacement of the bar. As a result, the potential in the bar arises solely from the inputs at the boundary and (2.4.2) simplifies to

$$\rho \ddot{u}_1 - \left[c_{11} - \frac{c_{13}^2}{c_{33}} \right] u_{1,11} = \left[e_{31} - \frac{c_{13}e_{33}}{c_{33}} \right] \Phi^{BC}{}_{,31} \tag{2.4.5}$$

In other words, the modified Laplace's equation in (2.4.4) is solved by the potential, Φ^{BC}, prescribed on the boundary of the bar. Due to the piezoelectric characteristics of the bar, this voltage input drives the acoustic wave equation above, producing sinusoidal displacements and an output current.

2.5 Electrostatic Solution

Because one-way coupling between the voltage inputs and the displacements of the resonator are a reasonable first order approximation, the electrostatic solution is reduced to the homogeneous part of the modified Laplace's equation and written as

$$\varepsilon_x \frac{\partial^2 \Phi}{\partial x^2} + \varepsilon_z \frac{\partial^2 \Phi}{\partial z^2} = 0 \tag{2.5.1}$$

35

where ε_x and ε_z are defined in (2.3.6) as

$$\varepsilon_x = \varepsilon_{11} + \frac{e_{15}^2}{c_{55}} \qquad (2.5.2)$$

$$\varepsilon_z = \varepsilon_{33} + \frac{e_{33}^2}{c_{33}} \qquad (2.5.3)$$

$\Phi(x, z = 2a) = f(x,t)$

$x = L$

$z = 2a$

$z = 0$

$\Phi(x, z = 0) = 0$

$x = 0$

z

y

x

** Bar is infinite in x-direction
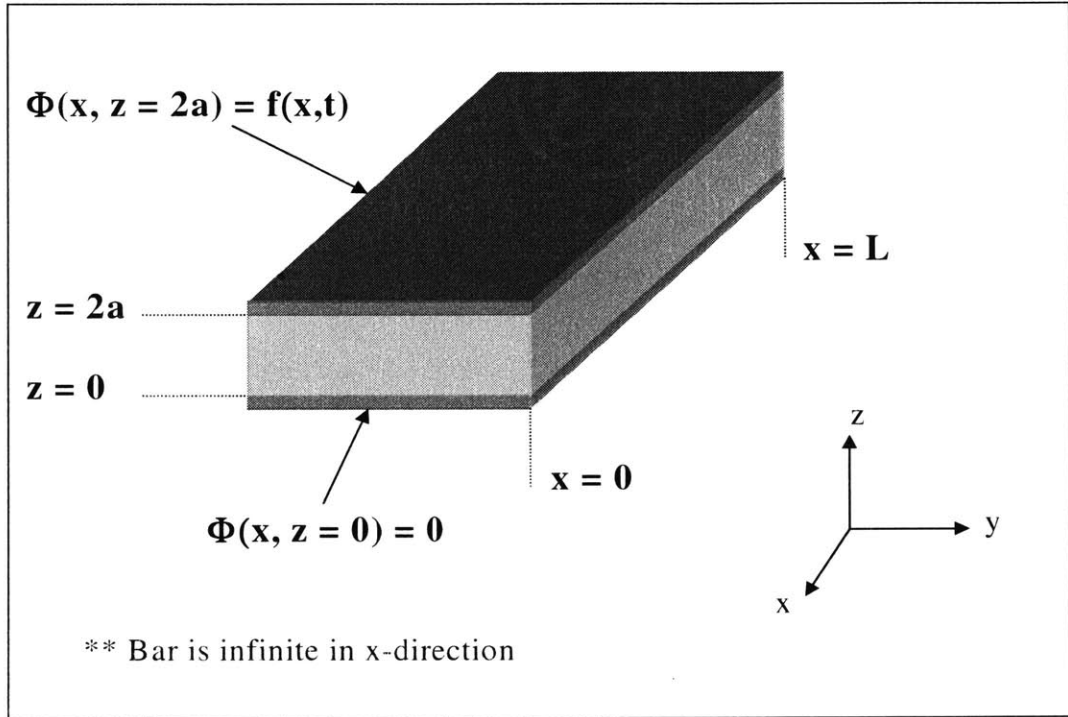
Figure 2.1: Piezoelectric resonator bar with spatial and potential boundary conditions.

Applying the one-way coupling approximation, (2.4.1) is now simplified to

$$\Phi = \Phi^{BC} + \Phi'' \cong \Phi^{BC} \qquad (2.5.4)$$

As in the mechanical analysis, we neglect any x_2 dependence, assuming uniformity of both displacement and potential in the x_2-direction. As illustrated in the figure above, the electrostatic boundary conditions are applied on the top and bottom surfaces of the bar, thus simulating the

existence of electrodes. These boundary conditions prescribe voltage inputs on the electrodes and are expressed in the following form.

$$\Phi(x, z = 0) = 0 \qquad\qquad (2.5.5)$$

$$\Phi(x, z = 2a) = f(x,t) \qquad\qquad (2.5.6)$$

In order to simplify the problem solving process from a mathematical standpoint, the bar will be assumed infinite in the x-direction. However, to account for the bar's actual finite length, an assumption is made about the limit of the potential function, $f(x,t)$, which captures the nature of Φ as we move away from the origin – $x \rightarrow \pm \infty$. If we assume that as $x \rightarrow \pm \infty$, $f(x,t) \rightarrow 0$, implied boundary conditions exist that define the limits of the potential, Φ, in the x-direction. This assumption allows for the bar to be both mechanically infinite and electrically finite at the same time. These implied boundary conditions can be expressed as

$$\lim_{x \rightarrow \pm \infty} \Phi(x, z = 0) = 0 \qquad\qquad (2.5.7)$$

Using Eq. (2.5.1) as a starting point, the electrostatic solution is determined by employing Fourier analysis. First, we transform (2.5.1) from the spatial to the frequency domain, solve the infinite series in the frequency domain, and finally, transform the result back to the spatial domain to maximize the applicability of the solution.

Let the Fourier transform and inverse transform be defined as the following

$$\Psi(k_x, z) = \frac{1}{2\pi} \int_{-\infty}^{\infty} \Phi(x,z) e^{ik_x x} dx = \Im_x\{\Phi\} \qquad\qquad (2.5.8)$$

$$\Phi(x,z) = \int_{-\infty}^{\infty} \Psi(k_x, z) e^{-ik_x x} dk_x = \Im_x^{-1}\{\Psi\} \qquad\qquad (2.5.9)$$

where k_x is the transform variable. Evaluating the first and second terms of (2.5.1), we arrive at the following expressions.

$$1^{st} \text{ Term: } \varepsilon_x \frac{\partial^2 \Phi}{\partial x^2} \rightarrow \int_{-\infty}^{\infty} \Psi(k_x, z) \cdot (-\varepsilon_x k_x^2) e^{-ik_x x} dk_x$$

$$2^{nd} \text{ Term: } \varepsilon_z \frac{\partial^2 \Phi}{\partial z^2} \rightarrow \int_{-\infty}^{\infty} (\varepsilon_z) \frac{\partial^2 \Psi(k_x, z)}{\partial z^2} \cdot e^{-ik_x x} dk_x$$

In the first term, the exponential expression is the only part with an x dependence, and therefore can be evaluated independently adding $-\varepsilon_x k_x^2$ to the integrand. Similarly, the Fourier transform, $\Psi(k_x, z)$, is the only part of the second term which has a z-dependence and, as a result, the 2nd partial derivative with respect to z can be applied to the transform alone. Combining the terms and distributing yields the Fourier transform of (2.5.1) expressed in the frequency domain

$$\int_{-\infty}^{\infty} \left[-\varepsilon_x k_x^2 \Psi(k_x, z) + \varepsilon_z \frac{\partial^2 \Psi(k_x, z)}{\partial z^2} \right] e^{-ik_x x} dk_x = 0 \qquad (2.5.10)$$

For all non-zero dk_x, the *RHS* of (2.5.10) is equal to zero if the argument inside the integral equals zero. Therefore, the following differential equation must hold.

$$\varepsilon_z \frac{\partial^2 \Psi}{\partial z^2} - \varepsilon_x k_x^2 \Psi = 0 \qquad (2.5.11)$$

The roots of the differential equation above are calculated by solving

$$m^2 - \frac{\varepsilon_x}{\varepsilon_z} k_x^2 = 0 \qquad (2.5.12)$$

The roots of (2.5.12) are expressed as

$$m = \pm k_x \sqrt{\frac{\varepsilon_x}{\varepsilon_z}} \qquad (2.5.13)$$

Finally, the general solution follows naturally as

$$\Psi(k_x, z) = a(k_x)e^{zk_x\sqrt{\frac{\varepsilon_x}{\varepsilon_z}}} + b(k_x)e^{-zk_x\sqrt{\frac{\varepsilon_x}{\varepsilon_z}}} \qquad (2.5.14)$$

With the general solution determined, the specific solution relating to the bar resonator is found by applying the boundary conditions shown in Fig. 2.1. The boundary conditions are prescribed on the top and bottom surfaces of the bar corresponding to the electrode positions in the actual device. As shown in Figure 2.1, at $z = 0$, $\Phi = 0$, and from (2.5.8) we know that $\Psi = 0$. Therefore, applying this condition to (2.5.14), we find the following relationship for the frequency dependent coefficients.

$$a(k_x) = -b(k_x) \qquad (2.5.15)$$

Substituting this relationship back into the general solution, we now express the transform equation as

$$\Psi(k_x, z) = a(k_x)\left[e^{zk_x\sqrt{\frac{\varepsilon_x}{\varepsilon_z}}} - e^{-zk_x\sqrt{\frac{\varepsilon_x}{\varepsilon_z}}} \right] = a(k_x)2\sinh\left[zk_x\sqrt{\frac{\varepsilon_x}{\varepsilon_z}} \right] \qquad (2.5.16)$$

Furthermore, at $z = 2a$, we know that $\Phi = f(x)$. Using this second condition, we solve for the lone coefficient, $a(k_x)$. Applying the boundary condition for the top electrode and recalling that $\Psi = \Im_x\{\Phi\}$ yields the following equation for $a(k_x)$

$$a(k_x) = \frac{\Im_x\{f(x)\}}{2\sinh\left[2ak_x\sqrt{\frac{\varepsilon_x}{\varepsilon_z}} \right]} \qquad (2.5.17)$$

and Eq. (2.5.16) becomes

$$\Psi(k_x, z) = \frac{2\sinh\left[zk_x\sqrt{\dfrac{\varepsilon_x}{\varepsilon_z}}\right]}{2\sinh\left[2ak_x\sqrt{\dfrac{\varepsilon_x}{\varepsilon_z}}\right]}\,\mathfrak{I}_x\{f(x)\} \qquad (2.5.18)$$

With the infinite series solved in the frequency domain, the final step is to transform the solution back to the spatial domain to better understand the electromechanical characteristics of the bar from a physical standpoint. This final solution is found by taking the inverse transform of the *RHS* of (2.5.18), giving the following equation.

$$\Phi(x, z) = \mathfrak{I}_x^{-1}\left\{\frac{2\sinh\left[zk_x\sqrt{\dfrac{\varepsilon_x}{\varepsilon_z}}\right]}{2\sinh\left[2ak_x\sqrt{\dfrac{\varepsilon_x}{\varepsilon_z}}\right]}\right\} * f(x) = \mathfrak{I}_x^{-1}\{\Psi\} \qquad (2.5.19)$$

In order to check the solution above, we substitute $z = 2a$ and $z = 0$ into (2.5.19) and find that the solutions for Φ match the boundary conditions - $\Phi(x, 2a) = f(x)$ and $\Phi(x, 0) = 0$. At this point, the constraints on the final equation are further specified by applying the approximation that the length of the bar is much larger than is thickness – expressed by the inequality, $x \gg 2a$. This is a reasonable approximation because the resonator's length to height ratio ranges from *10* to *60*. Assuming this approximation holds, the solution for the potential in the spatial domain is linear through the thickness of the bar. In order to show this relationship, (2.5.19) is non-dimensionalized by rescaling the transform variable, k_x. We create a non-dimensional parameter, k, which is equal to the ratio $k_x/2a$ and substitute this value into (2.5.19). The new equation becomes

$$\Phi(x, z) = \mathfrak{I}_x^{-1}\left\{\frac{2\sinh\left[\dfrac{z}{2a}k\sqrt{\dfrac{\varepsilon_x}{\varepsilon_z}}\right]}{2\sinh\left[k\sqrt{\dfrac{\varepsilon_x}{\varepsilon_z}}\right]}\right\} * f(x) \qquad (2.5.20)$$

40

We then make the critical assumption that $k \ll 1$ and $\varepsilon_x \sim \varepsilon_z$. While the latter is simply a numerical approximation that is easily justified, the former is not obvious and requires a more detailed explanation. The inequality above can also be expressed as $k_x \ll 1/2a$. Recalling that, in the electromagnetic (EM) frequency domain, k_x is equal to the inverse of the wavelength, the relationship can be written yet another way as $\lambda \gg 2a$, thus indicating that the wavelength of an EM wave in the resonator is much larger than the bar's thickness. This relationship can be validated by calculating a typical wavelength for an electromagnetic wave traveling through the bar and then comparing it to the value of $2a$. Because the operational frequency range of the resonator is known, an approximate wavelength value can be determined by employing the relationship between the wavelength and frequency of an electromagnetic wave - $c_{mat} = \lambda f$, where c_{mat} is the electromagnetic wave speed in the material, and frequency is measured in Hz. Typically, the electromagnetic wave speed for a given material depends on its relative dielectric constant and is calculated according to the equation

$$c_{mat} = \frac{c}{\sqrt{\varepsilon_r}}, \; where \; c = 3.8x10^8 \; m/s \tag{2.5.21}$$

For AlN, the relative dielectric constant is 9.5, making c_{mat} approximately equal to a value of $9.73x10^7$ m/s. Therefore, considering a sinusoidal driving frequency of 1 GHz, the corresponding wavelength of an electromagnetic wave produced in the bar is on the order of .1 meters. Comparing this wavelength with the value of $2a$, which is on the order of a micron, we find that the wavelength of an EM wave in the resonator is much greater than the characteristic dimension of the bar. As a result, the assumption that $\lambda \gg 2a$ is a valid one. Furthermore, because $k \ll 1$ indicates the same relationship, we utilize it to simplify (2.5.20) to the following

$$\Phi(x, z) = \mathfrak{F}_x^{-1}\left\{\frac{z}{2a}\right\} * f(x) = f(x)\frac{z}{2a} \tag{2.5.22}$$

recalling that, in general, for $\eta \ll 1$, $sinh(\eta) \approx \eta$. For a bar with a high aspect ratio (length/thickness), the potential function is approximated as having a linear variation through the thickness described by Equation (2.5.22). According to (2.5.22), the potential varies linearly

from zero on the bottom electrode to the function $f(x)$ on the top electrode. This condition assumes that the electric field produced between the electrodes is generally uniform and neglects the effects of fringing fields at the edges. The fringing fields can be ignored because the high aspect ratio of the bar's geometry. This geometric characteristic makes it possible to employ the parallel plate approximation, which is only valid for structures whose length and width are much larger than its thickness.

2.6 Mechanical Resonance: Time and Spatial Solutions

With the electrostatic solution solved and simplified to a convenient form, we determine the mechanical solution. This is accomplished by employing Eqs (2.2.9) and (2.5.22), which describe the longitudinal inertia of the bar and the linear relationship for the potential through the thickness. Recalling that (2.2.9) is simplified to the form

$$\rho \ddot{u}_1 - \left[c_{11} - \frac{c_{13}^2}{c_{33}} \right] u_{1,11} = \left[e_{31} - \frac{c_{13}e_{33}}{c_{33}} \right] \Phi_{,31} \tag{2.2.9}$$

The potential term on the left side is written as

$$\Phi_{,31} = \frac{f_{,1}}{2a} \tag{2.6.1}$$

Also, for simplicity, the coefficients in (2.2.9) are defined more concisely as

$$c_o = c_{11} - \frac{c_{13}^2}{c_{33}} \tag{2.6.2}$$

$$e_o = e_{31} - e_{33} \frac{c_{13}}{c_{33}} \tag{2.6.3}$$

Because (2.2.9) is a linear differential equation, separation of variables is used to solve for the function that describes the longitudinal displacement, $u(x,t)$.

$$u(x,t) = \sum_{n=-\infty}^{\infty} A_n(t) \cdot X_n(x) \qquad (2.6.4)$$

The longitudinal displacement has both a time and spatial dependence. However, because of linearity, the function described by (2.6.4) is accurately represented as the product of two individual functions, one with only a time dependence and the other with only a spatial dependence. Furthermore, summation operator is present in the displacement function, because the solution is actually an infinite series of all the normal modes of the bar. In order to find the complete set of eigenvectors for the structure, we consider the unforced wave equation. Applying the simplifications noted above, the unforced form of (2.2.9) becomes

$$\sum_n \rho \ddot{A}_n \cdot X_n - \sum_n c_o A_n \cdot X_n'' = 0 \qquad (2.6.5)$$

Separating variables, time dependent variables are set equal to their spatial counterparts, and the unforced wave equation is expressed in the form

$$\frac{\ddot{A}_n}{A_n} = \frac{c_o}{\rho} \frac{X_n''}{X_n} \qquad (2.6.6)$$

Because the LHS of (2.6.6) is dependent solely on time and the RHS has only a spatial dependence, their common solution must be a constant, having neither a time nor a spatial dependence of its own. If we define this constant as $-\omega_n{}^2$, we know that ω_n represents the natural frequency of mode n and are now able to determine the eigenvalues of the infinite series. We first solve the time dependent problem, which has the same solution for both a continuous and a lumped mass-spring model. Because the time solution is consistent between the models, we solve the simpler system. Figure 2.2 illustrates the mass-spring system with its key features labeled.

43

Rigid Support

Spring Stiffness - k

Lumped Mass

M — x = 0
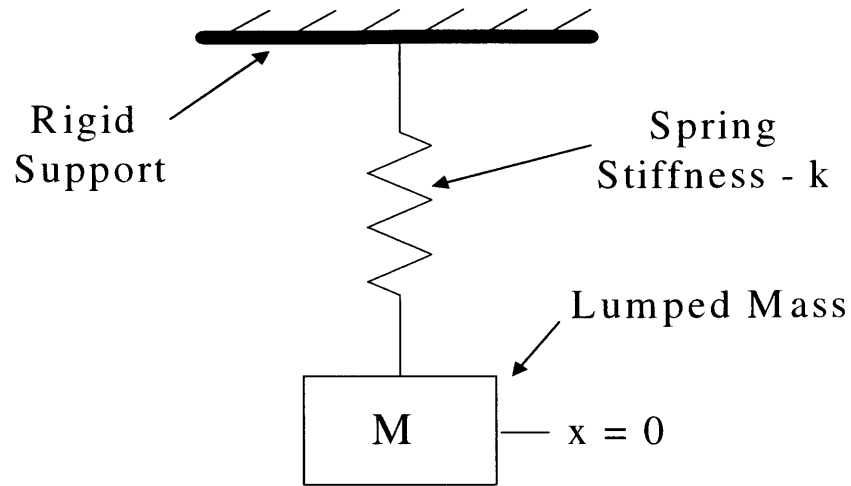
Differential Equation of Motion:

$$M\,\ddot{x} + kx = 0$$

Figure 2.2: Lumped parameter mass-spring model

The equation of motion for the mass-spring system is written as

$$M\,\ddot{x} + kx = 0 \tag{2.6.7}$$

Solving for the roots (ω_n, where n = 1, 2, 3,...) of this differential equation, we find they are expressed as

$$\omega_n^{\,2} = \frac{k}{M} \tag{2.6.8}$$

The solution to (2.6.7) is straightforward and well known in the form

$$x_n(t) = a_n \cos(\omega_n t) + b_n \sin(\omega_n t) \tag{2.6.9}$$

and with respect to Eq (2.6.6) for the continuous model, the solution above becomes

$$A_n(t) = l_n \cos(\omega_n t) + m_n \sin(\omega_n t) \tag{2.6.10}$$

where the constants l_n and m_n are chosen to satisfy initial conditions. With the time solution determined, we now shift focus to the spatial component of the wave equation. Recalling the relationship established between the time and spatial domains in (2.6.6), the spatial equation can be written as

$$X_n'' = -\omega_n^2 \frac{\rho}{c} X_n \tag{2.6.11}$$

Once again, the solution is relatively straightforward and is simply the summation of the infinite cosine series over all possible n. Below are the solution and the applicable free-free boundary conditions. A free-free condition is imposed by prescribing zero strain at the ends of the bar.

$$X_n(x) = \cos\left(\omega_n \sqrt{\frac{\rho}{c}} \cdot x\right) \tag{2.6.12}$$

$$X_n'(x = 0) = X_n'(x = L) = 0 \tag{2.6.13}$$

Applying the boundary conditions above and solving for ω_n, the natural frequency and final solution to the longitudinal wave equation are

$$\omega_n = \frac{n\pi}{L} \sqrt{\frac{c}{\rho}} \tag{2.6.14}$$

$$u(x,t) = \sum_{n=-\infty}^{\infty} \cos\left(\frac{n\pi}{L} x\right) \cdot \left[l_n \cos(\omega_n t) + m_n \sin(\omega_n t)\right] \tag{2.6.15}$$

45

The solution above is for the unforced eigenvalue problem. In order to solve the driven wave equation, a forcing term is be added to (2.6.5). For our bar, the forcing function is defined as $f(x,t)$. However, according to (2.6.1), the function which drives the bar is expressed in terms of $f_{,1}$, the first spatial derivative of $f(x,t)$. Therefore, the driving force is designated as $f_{,1}(x,t)$, which is again represented as the product of a time and spatial function summed over all n. The forcing function and driven wave equation are then written as

$$f_{,1}(x,t) = \sum_{n=-\infty}^{\infty} F_n(t) \cdot X_n(x) \tag{2.6.16}$$

$$\rho \ddot{A}_n \cdot X_n - c_o A_n \cdot X_n'' = \frac{e_o}{2a} F_n X_n \tag{2.6.17}$$

where $2a$ is again defined as the thickness of the bar, and e_o is the simplified piezoelectric constant described by Equation (2.6.3). As with the unforced eigenvalue problem, (2.6.17) is manipulated so that all time and spatial variables are grouped separately on opposite sides of the equation. Furthermore, we also assume the separation constant to be the same. As a result, we arrive at the following separated differential equation for the forced problem.

$$\frac{\ddot{A}_n}{A_n} - \frac{e_o}{2a\rho} \frac{F_n}{A_n} = \frac{c_o}{\rho} \cdot \frac{X_n''}{X_n} = -\omega_n^2 \tag{2.6.18}$$

As before, the time domain problem is solved first. However, unlike the unforced case, in order to accurately represent the time-dependent behavior of the driven resonator, we add a modal damping term, γ_n. This damping term is expressed as a function of the modal center frequency.

$$\gamma_n = \frac{\omega_n}{Q} \tag{2.6.19}$$

where Q denotes the Quality factor of the resonator. Focusing only on the time dependent side of (2.6.18), adding the damping, and rearranging terms, we arrive at the equation governing the time domain response of the forced problem.

$$\ddot{A}_n + \gamma_n \dot{A}_n + \omega_n^2 A_n = \frac{e_o}{2a\rho} F_n \qquad\qquad (2.6.20)$$

Converting (2.6.20) from the time to the frequency domain and solving, the following relationship is obtained.

$$\frac{A_n(s)}{F_n(s)} = \frac{e_o / 2a\rho}{s^2 + \gamma_n s + \omega_n^2} \qquad\qquad (2.6.21)$$

The spatial solution is the same as that determined earlier for the unforced problem.

$$X_n = \cos\left(\frac{n\pi}{L}x\right) \qquad\qquad (2.6.22)$$

As (2.6.16) indicates, the spatial function for the driving force (i.e. $f_{,1}(x,t)$) matches that of the unforced problem. In reality, the spatial function can be any infinite series, but the cosine form seems to be the most logical and convenient choice.

The time-dependent component of the driving force, $F_n(t)$, represents the projection of the driving force, $f_{,1}(x,t)$, onto the individual modes. The driving force, of course, is directly related to the potential on the bar. Specifically, it is proportional to the first spatial derivative of the potential function. This potential function was defined earlier in (2.5.6) as the boundary condition prescribed on the bar's top electrode. In practice, $f(x,t)$ does not have a spatial dependence along the bar, because the electrode is assumed to be a perfect conductor and thus, equi-potential. As a result, the actual function describing the potential across the top electrode is

$$f(x,t) = V_o(t) * [u(x) - u(x - L)] \qquad\qquad (2.6.23)$$

where $V_o(t)$ is the time-dependent magnitude of the AC input voltage used to drive the bar. The $u(x)$ functions are mathematical conventions used to describe the shape of $f(x,t)$. In words, the

47

function is described as: $f(x,t)$ is equal to $V_o(t)$ from $0 < x < 6$ μm, and otherwise equal to zero. For mathematical convenience, we would like to express $f(x,t)$ as an infinite Fourier series. However, because the function is not periodic, it is not possible to reproduce it by these means. This fact notwithstanding, if we assume the equi-potential range to be part of an infinite periodic square wave, the mathematical representation becomes much more straightforward. Therefore, we choose to define $f(x,t)$ in the following way.

$$f(x,t) = \sum_{n=-\infty}^{\infty} a_n(t) \cdot \sin\left(\frac{n\pi}{L}x\right)$$
(2.6.24)

where a_n is the Fourier coefficient for the series and represents the weighting factor that determines contribution of each term to the sum. This coefficient is solved for according to

$$a_n(t) = \frac{2}{L}\int_0^L V_o(t) \cdot \sin\left(\frac{n\pi}{L}x\right) dx$$
(2.6.25)

Solving (2.6.25) and substituting back into (2.6.24), the sine series for $f(x,t)$ is written as

$$f(x,t) = \frac{2V_o(t)}{\pi} \sum_{n=-\infty}^{\infty} \frac{1}{n}\left(1 - (-1)^n\right) \cdot \sin\left(\frac{n\pi}{L}x\right)$$
(2.6.26)

This is the sine series that reproduces the function $f(x,t)$, describing the potential along the length of the top electrode - $0 < x < 6$ μm. A graphical approximation of the Fourier sum in this range is shown in Figure 2.3.

48

Normalized Potential vs Position
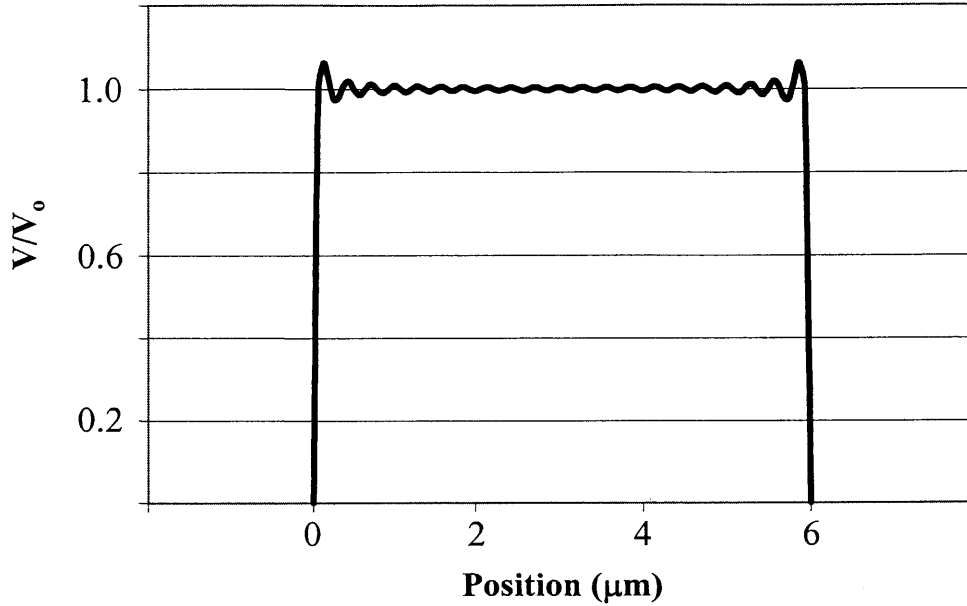
Figure 2.3: Graphical approximation of square function $f(x,t)$ reproduced by Fourier sine series.

Equation (2.6.26) describes the potential function only. However, in order to determine the total displacement solution, we need to obtain the expression for the magnitude, $F_n(t)$, of the forcing function, written as $f_{,1}(x,t)$ and defined by (2.6.16). Noting that the expression $1-(-1)^n$ reduces the potential function to an odd sine series, we solve for the forcing function by taking the first spatial derivative of (2.6.26). The result of this operation yields

$$f_{,1}(x,t) = \frac{4V_o(t)}{L} \sum_{n=-\infty}^{\infty} \cos\left(\frac{n\pi}{L}x\right), \; where \; n = 1,3,5,... \tag{2.6.27}$$

Comparing the equation above to (2.6.16), we find that the cosine term in the summation argument matches the spatial solution of the unforced problem. Therefore, we further deduce that the expression outside the argument must be equal to $F_n(t)$. To match the form of (2.6.21), we convert from the time to the frequency domain, and $F_n(s)$ is expressed as

$$F_n(s) = \frac{4V_o(s)}{L} \tag{2.6.28}$$

49

Using the equation for $F_n(s)$, we substitute back into (2.6.21) to solve for the frequency dependent displacement coefficient. Solving for $A_n(s)$, we arrive at the following result.

$$A_n(s) = \frac{2e_o}{a\rho L} \cdot \frac{V_o(s)}{s^2 + \gamma_n s + \omega_n{}^2} \qquad (2.6.29)$$

Finally, to obtain the total displacement solution, we introduce the expression for $A_n(s)$ into Eq (2.6.4), and the frequency dependent form of the displacement equation, $u(x,s)$, becomes

$$u(x,s) = \frac{2e_o}{a\rho L} \cdot \cos\left(\frac{\pi}{L}x\right) \cdot \frac{V_o(s)}{s^2 + \gamma_n s + \omega_n{}^2} \qquad (2.6.30)$$

where the n term has been assigned a value of unity in order to isolate the primary longitudinal mode.

2.7 Electrical Transfer Function

We now return to Gauss' Law describing the relation between the free charge density, ρ, and the electrical displacement, D_3, normal to the interface of the dielectric and the electrode. The boundary condition prescribed at this interface is written below and constitutes a reduced form of (2.3.1), applicable specifically to the geometry and coordinate system of interest.

$$- D \cdot \hat{z} = -D_3 = \rho \qquad (2.7.1)$$

To find the electromechanical transfer function of the bar, we calculate the output charge resulting from the sinusoidal input voltage, $V_o(s)$. This charge is determined by integrating the normal component of the electrical displacement, D_3, over the total electrode area. The current is then calculated by taking the time derivative of the total charge. The current, or admittance of the bar, is solved for according to

$$I = \dot{Q} = \frac{\partial}{\partial t}\left(\int\limits_{\substack{dA \\ (electrode)}} -D_3\, dA \right)$$

(2.7.2)

Recalling the assumption that piezoelectric coupling between the input voltage and bar displacement is in one direction only, D_3 is defined according to the constitutive equations.

$$D_3 = e_0 u_{1,1} - \varepsilon_z \Phi_{,3}$$

(2.7.3)

where ε_z and e_o are defined by (2.5.3) and (2.6.3), respectively, as the more compact form of the material property coefficients. By substituting the total displacement and potential solutions into (2.7.3), we obtain D_3 as expressed in the frequency domain.

$$D_3(x,s) = -\frac{2e_o^2 \pi}{a\rho L^2}\cdot \sin\left(\frac{\pi}{L}x\right)\cdot \frac{V_o(s)}{s^2 + \gamma_n s + \omega_n^2} - \frac{\varepsilon_z}{2a}\cdot V_o(s)$$

(2.7.4)

$\Phi_{,3}$ is replaced by the quotient of the potential function, $V_o(s)$, and the thickness, $2a$. Furthermore, we return to the original definition of $f(x,t)$ as defined by (2.6.23). Continuing to use the Fourier sine series representation would create difficulty when taking the area integral to find the current. Therefore, the current calculation is simplified by setting $f(x,t)$ equal to $V_o(t)$ and converting the differential area, dA, to a constant width, w, multiplied by dx. Then, solving (2.7.2), a relationship for the current output due to the input voltage is obtained and written as

$$I = \frac{4we_o^2}{a\rho L}\cdot \frac{sV_o(s)}{s^2 + \gamma_n s + \omega_n^2} + \frac{\varepsilon_z wL}{2a}sV_o(s)$$

(2.7.5)

51

2.8 Equivalent Circuit Model

From (2.7.4), the bar's impedance characteristic versus frequency is calculated by Ohm's relation, $V_o(s)/I$. This impedance looks similar to that of an *RLC* circuit in parallel with a single parallel plate capacitor. In this configuration, the parallel capacitance is simply defined by

$$C_o = \frac{\varepsilon_z wL}{2a} \tag{2.8.1}$$

In order to determine the values of the equivalent *RLC* circuit, we manipulate the circuit's transfer function to match the coefficient of the first term in (2.7.4). The original transfer function and its manipulated form are defined below.

$$Z_{RLC} = sL + R + \frac{1}{sC} = \frac{s^2LC + sRC + 1}{sC} \tag{2.8.2}$$

$$\frac{1}{Z_{RLC}} = \frac{\dfrac{s}{L}}{s^2 + (R/L)s + \dfrac{1}{LC}} \tag{2.8.3}$$

Using Ohm's Law, we draw the connection between the current defined by (2.7.5) and the equivalent circuit. With the parallel term already accounted for by (2.8.1) we arrive at the following relationship

$$I = \left[\frac{1}{L} \frac{s}{s^2 + (R/L)s + \dfrac{1}{LC}} \right] V_o(s) = \left[\frac{4we_o^2}{a\rho L} \frac{s}{s^2 + \gamma_n s + \omega_n^2} \right] V_o(s) \tag{2.8.4}$$

Matching terms between the two current equations, the motional inductance can be expressed as

52

$$L = \frac{a\rho L}{4we_o^2} \qquad (2.8.5)$$

The other circuit parameters are then represented in terms of L, recalling the equations for ω_n and γ_n, as defined by (2.6.14) and (2.6.19).

$$C = \frac{1}{\omega_1^2 L} = \frac{4we_o^2}{a\rho L} \cdot \frac{L^2\rho}{\pi^2 c_o} = \frac{4we_o^2 L}{a\pi^2 c_o} \qquad (2.8.6)$$

$$R = \gamma_1 L = \frac{\omega_1}{Q} \frac{a\rho L}{4we_o^2} = \sqrt{c_o\rho} \frac{a\pi L}{4we_o^2 Q} \qquad (2.8.7)$$

With the equivalent *RLC* circuit parameters defined, we determine the total transfer function describing the impedance characteristic of the *6x3x0.5* μm bar. Below is a schematic showing the bar geometry and equivalent circuit topology.
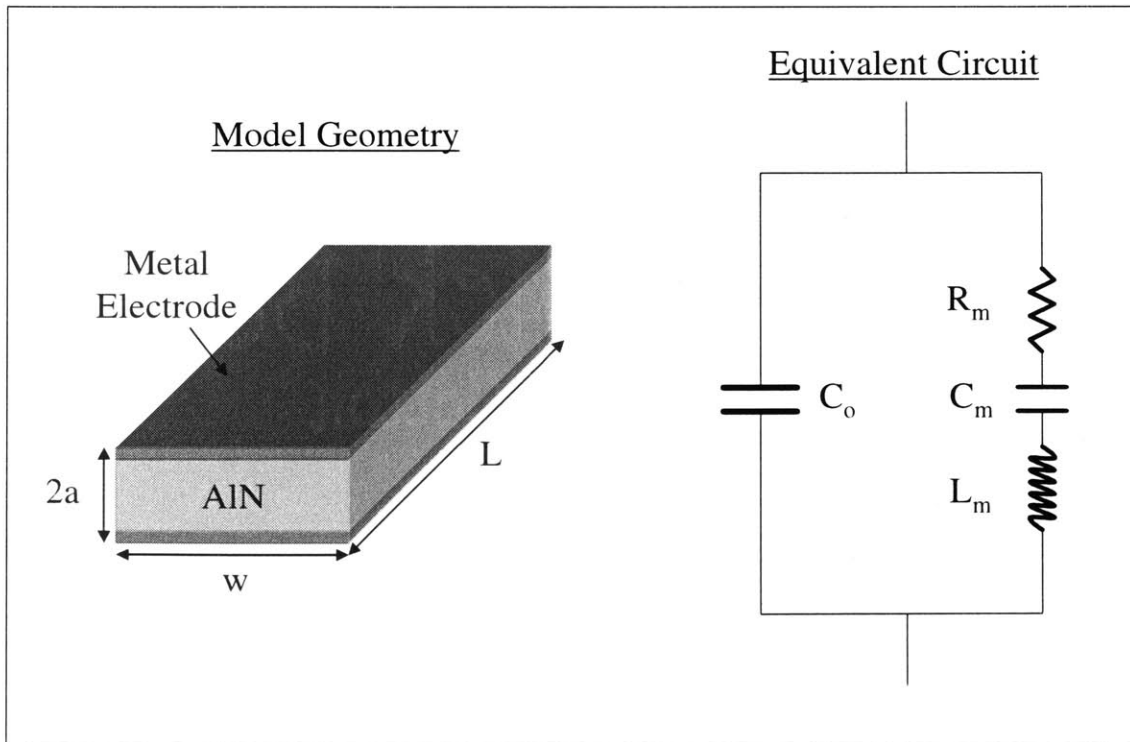
Figure 2.4: AlN piezoelectric longitudinal bar and its equivalent RLC circuit

Using the circuit parameters defined by Equations (2.8.4), (2.8.5), and (2.8.6) as well as the material properties of AlN, we obtain the relationship between impedance and frequency for the resonator. The material property values used for this analytical analysis are listed in Table 2.1.

Material Parameter	Symbol (Units)	Value
Density	ρ (kg/m^3)	3300
Stiffness Constant	c_o (N/m^2)	3.09e11
Dielectric Constant	ε_z (F/m)	9.02e-11
Piezoelectric Constant	e_o (C/m^2)	-1.051

Table 2.1: AlN material property values used for the equivalent circuit model

As specified earlier, the dimensions of the longitudinal bar are

$$L = 6 \ \mu m, \quad w = 3 \ \mu m, \quad 2a = 0.5 \ \mu m$$

These dimensional parameters yield the following values for R, L, C and C_o of the equivalent circuit

$$\frac{\omega_l}{2\pi} = \frac{1}{2L}\sqrt{\frac{c}{\rho}} = 805.8 \ \text{MHz} \qquad C_o = \frac{\varepsilon_z wL}{2a} = 3.246 \ \text{fF}$$

$$R = \sqrt{c_o \rho} \ \frac{a\pi L}{4we_o^2 Q} = 1891 \ \Omega \qquad L = \frac{a\rho L}{4we_o^2} = 3.735 \times 10^{-4} \ \text{H}$$

$$C = \frac{4we_o^2 L}{a\pi^2 c_o} = .104 \ \text{fF}$$

These circuit parameters produce the impedance transfer function shown in Figure 2.5. For $Q = 1000$, the impedance of the bar drops to approximately 1890 Ω at the longitudinal resonance, corresponding to the R value of the equivalent circuit.

Impedance vs Frequency
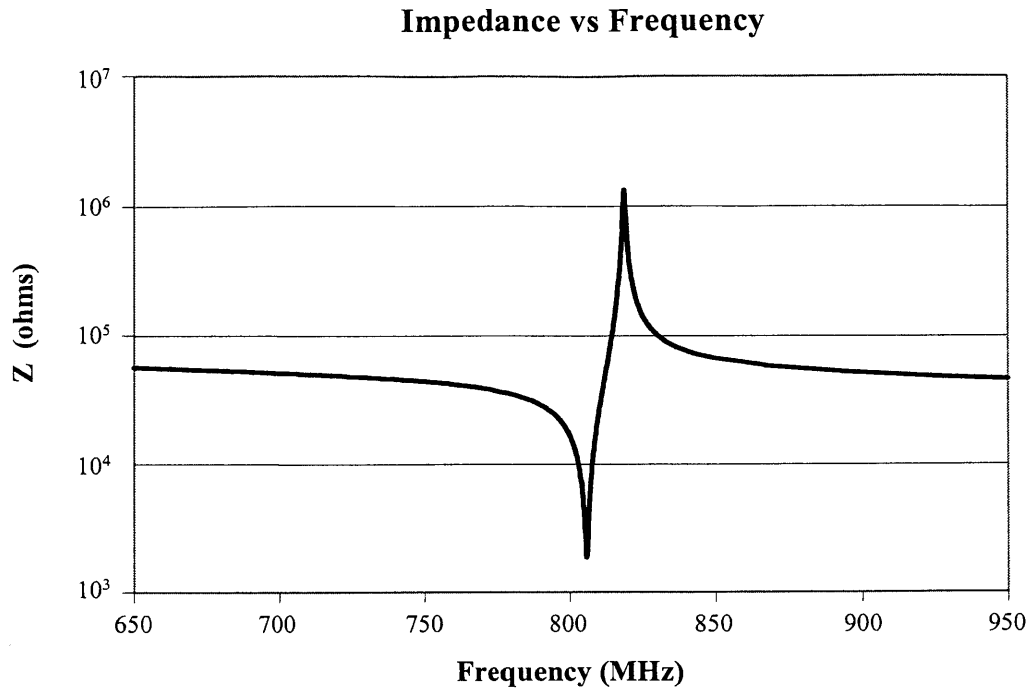
Figure 2.5: Graph of the resonator bar's impedance versus frequency

[THIS PAGE INTENTIONALLY LEFT BLANK]

Chapter 3

Comparison of Simulation and Analytical Results

3.1 Electromechanical FEA Model (No Tethers)

With an analytical derivation and equivalent circuit model established for the piezoelectric L-Bar resonator, electromechanical simulations are utilized to validate the results of Ch.2. In this chapter, the simulated FEA model has the same geometry and boundary conditions as the analytical model. Because it is necessary to limit the analytical analysis to relatively simple geometries, the corresponding FEA model is comprised of the resonator bar without support tethers. Figure 3.1 shows the FEA geometry of the analytical bar with its corresponding electrical and spatial boundary conditions.
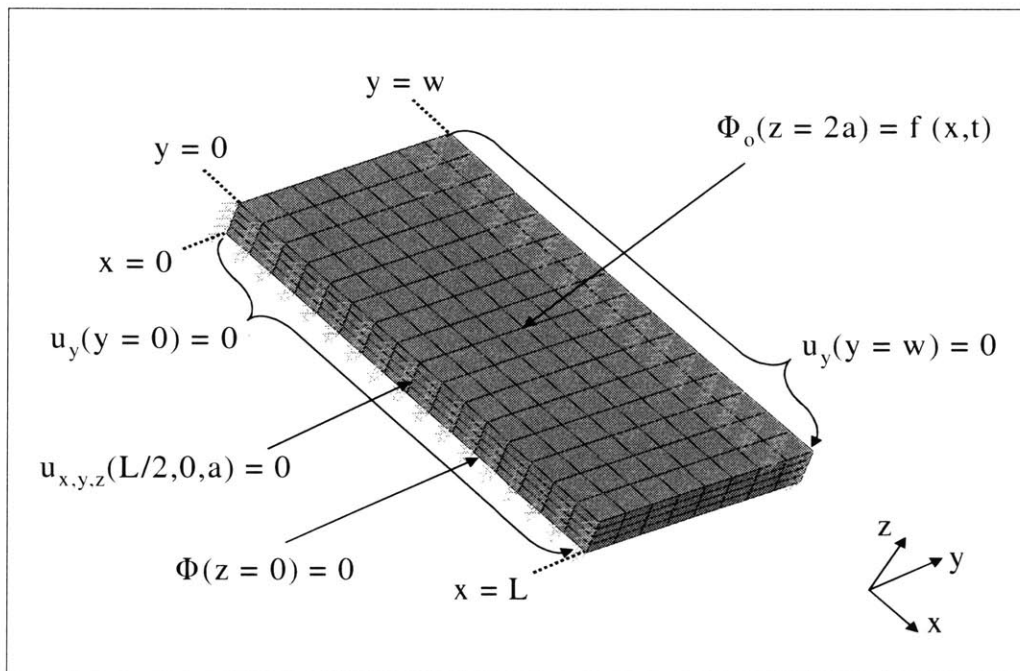
Figure 3.1: FEA model of bar without support tethers. In the model presented, L = 6 μm, w = 3 μm, and 2a = 0.5 μm.

The purpose of the model in Fig. 3.1 is to serve as an FEA equivalent to the analytical model. All dimensions, boundary conditions and other material parameters are made to match, as closely as possible, those used to derive the *RLC* circuit model. The bar's dimensions are maintained at: L = 6 μm, w = 3 μm, and t = 0.5 μm. To mimic an infinite boundary condition through the width of the resonator, all the nodes at y = 0 and y = w are fixed in the y-direction. Furthermore, to fully constrain the model, a cantilever condition is placed on the node at the center of the left edge (i.e. point → (L/2, 0, a)). For the electrical boundary conditions, electrodes are modeled by coupling the nodes along the top and bottom surfaces of the bar and prescribing a potential value on the master node of each set. The equi-potential condition on the electrodes is applied in this manner because, for simplicity, neither the mass nor the stiffness of the metal layers is modeled in the geometry. Finally, a mechanical Quality factor (Q) of 1000 is prescribed for the structure. The goal for the actual resonator design is a Q of 10^4. However, for Q = 10^4, the bandwidth of the model's response at resonance is extremely small and thus, difficult for the FEA program to capture accurately. Therefore, a value of 1000 is set for simulations in order to facilitate adequate resolution of the resonant response. The Quality factor is input into the FEA parameters as a damping ratio relating to the resonator Q by the following equation.

$$Q = \frac{1}{2\xi} \qquad (3.1)$$

where ξ is a constant damping ratio across the frequency range of the harmonic analysis. Thus, to assign a Q of 1000, the user inputs a value of .0005 for the damping ratio.

The table below shows the material properties used for the FEA model.

Material Parameter	Symbol (Units)	Value
Density	ρ (kg/m^3)	3300
Stiffness Constants	c_{11}, c_{22} (N/m^2)	3.45e11
	c_{33}	3.95e11
	c_{12}	1.25e11
	c_{13}, c_{23}	1.20e11
Dielectric Constants	ε_{11}, ε_{22}, ε_{33} (F/m)	8.41e-11
Piezoelectric Constants	e_{33} (C/m^2)	1.55
	e_{13}, e_{23}	-0.58

Table 3.1: Material properties for FEA model

For the analytical model, the problem solving process is made more convenient if a compact set (i.e. c_o, e_o, ε_z) of the material property coefficients is defined. However, because the FEA model is not being solved analytically, the actual orthotropic material property values of AlN are used. With an FEA model having virtually the same characteristics as its analytical counterpart, the output of the electromechanical FEA simulation is compared to the result obtained from the mathematical calculation.

3.2 Impedance Transfer Functions

The test procedure for finding the impedance transfer function of the bar is comprised of two main steps. First, a modal analysis is performed and the frequencies from the modal output are read into an array. The second step is to perform a harmonic sweep about each of the modal frequencies from the array. This procedure is applied to the model shown in Fig. 3.1, and a transfer function is obtained. Table 3.2 compares the key results between the two models, such as impedance and center frequency of the bar at the longitudinal resonance. Furthermore, Fig. 3.2 is the graph of the FEA result overlaid on the analytical curve. The sweep range is approximately 300 MHz from 650 to 950 MHz.

Model Type	Z (ohms)	ω_c (MHz)
FEA	1873.1	807
Analytical	1888.2	807.5
% Error	**0.800**	**0.062**

Table 3.2: Results for comparison of FEA and analytical models; Q = 1000

Impedance vs Frequency
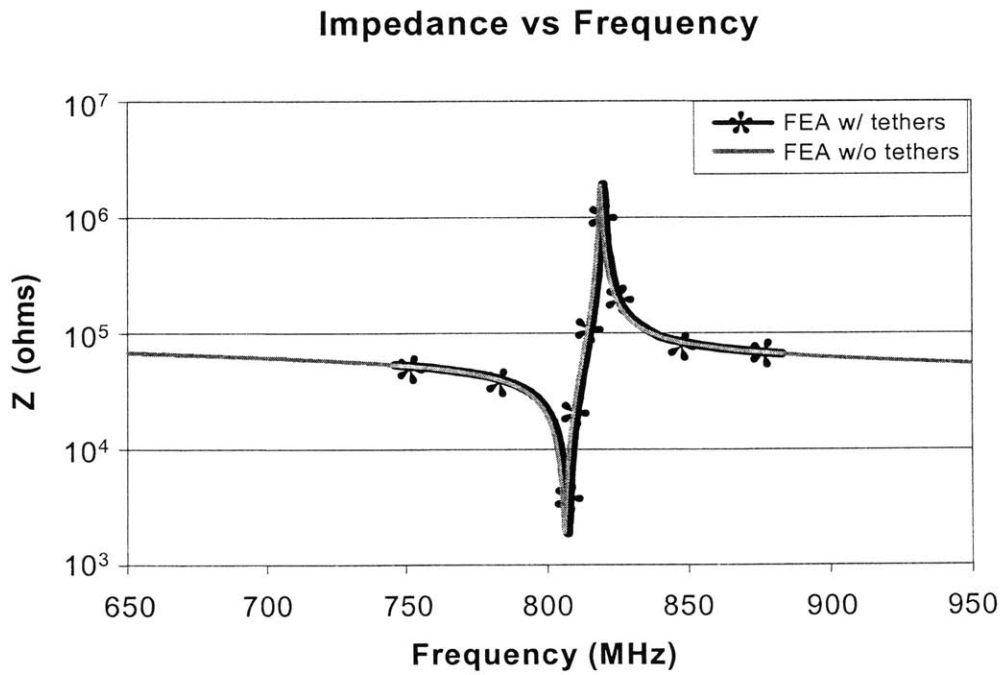
Figure 3.2: Plot of FEA/analytical impedance results

Both the table and graph above demonstrate that the FEA results match those predicted by theory. The two models' impedances and center frequency values at the longitudinal resonance coincide to within a percent difference of each other. This result illustrates that, with the correct boundary conditions and material parameters applied, the FEA model and the analytical calculation validate each other.

Chapter 4

Boundary Condition Study: Single Bar

4.1 Exploring Models of Greater Complexity

With the analytical results validated by simulation data, the simple FEA model introduced in Ch. 1 is now qualified in relation to more complex geometries. The purpose of this case study is to determine the error associated with the results of the simpler model. In other words, we now attempt to find out if the simple model yields an acceptable tradeoff between modeling sophistication and simulation efficiency. The former provides increased accuracy and a more realistic model, while the latter facilitates the attainment of usable results. It is important to achieve a balance between these two aspects of modeling.

One of the resonator's primary roles is to interface with integrated circuit (IC) technology as a frequency filter component, driven and sensed in the electrical domain [5]. Voltage inputs are used to actuate the resonator while output potentials are employed to measure its response. The bond pads, used for electrically driving and sensing the resonator, are orders of magnitude larger than the dimensions of the bar. Consequently, a series of intermediate geometries are fabricated to link the resonator to the external environment – specifically, the bond pads and the packaging of the IC chip. The interactions between these intermediate geometries, the resonator, and the IC chip establish the actual boundary conditions of the device, which, in turn, determine how the resonator will behave in the electrical and mechanical domains. Ideally, the geometry and boundary conditions of the FEA model would correspond identically to those of the real device. However, because of the size discrepancy between the resonator and its external environment, the full set of boundary conditions and geometric components characterizing the electromechanical behavior of the MEMS filter cannot feasibly be modeled. The size and mesh characteristics (i.e. number of elements and nodes) of a model determine how feasibly it can be built and simulated. As the mesh density is refined, the simulation results, theoretically, become

more reliable. However, the computation time and memory requirements increase drastically. The simple geometry, including only the resonator and its support tethers, is thought to satisfy the balance needed between model size, mesh density, and computation time. However, to be certain, we compare its electromechanical output with the transfer functions of more complex geometries to determine the error between the results.

4.2 Determining Appropriate Tether Length for Study

In general, the purpose of the support tethers is to provide the resonator bar with partial acoustic isolation from the substrate. This isolation can never be perfect, however, because the tethers will always dissipate some portion of the resonator's energy to the environment. Therefore, to minimize this energy loss, an attempt to optimize the length of the tether supports is undertaken. Optimization of the tether length could potentially isolate a longitudinal wave traveling through the structure, thus trapping the energy of that wave and minimizing the amount of dissipation. Theoretically, a standing longitudinal wave could be established in the device if the tether ends coincided with a displacement node of that wave. If this were accomplished, the end of the tether would have zero displacement and the longitudinal wave traveling through the tether would be reflected perfectly, resulting in no transmission of the wave to the substrate. In reality, it is virtually impossible to determine the exact location of the wave node. However, a good approximation of that location would serve as a suitable starting point for choosing the appropriate tether length for the boundary condition study.

In order to determine the locations of the longitudinal wave nodes occurring along the tethers, a free-free boundary condition is applied to the resonator model geometry with extra long tethers. For the model shown in Figure 4.1, the primary nodes of the longitudinal wave in the tethers occur at approximately 6 μm and 12 μm from the edge of the resonator. Because the wavelength corresponding to the longitudinal natural frequency of the bar is 12 μm, this finding seems to be consistent with what would be expected in theory.
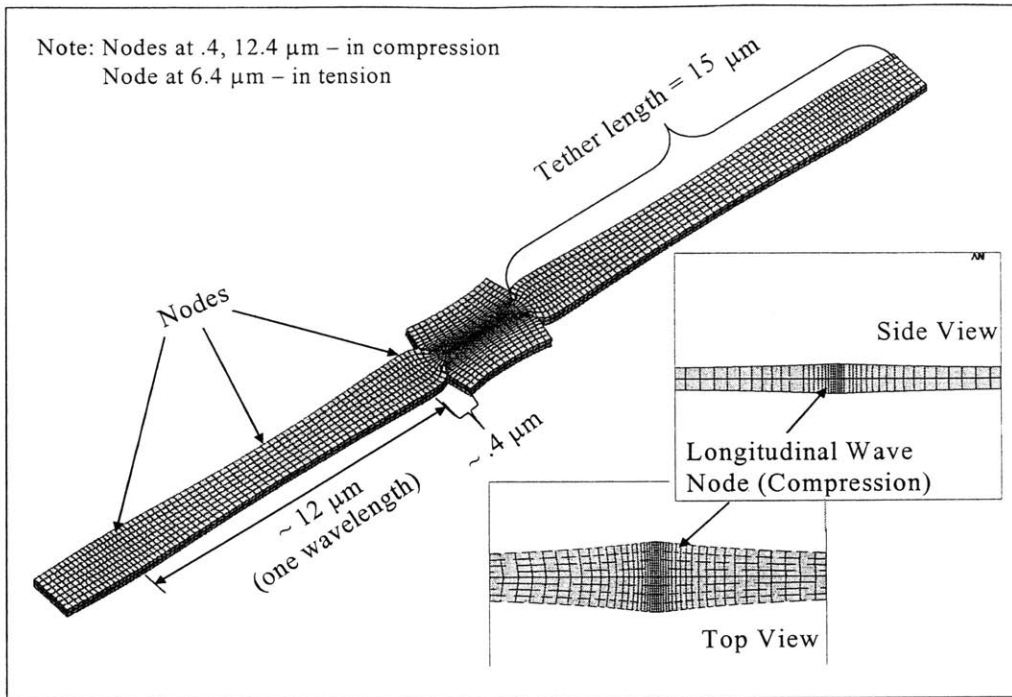
Figure 4.1: Resonator with extra long tether supports. Free-free boundary conditions imposed upon the tether ends; tether length = 15 μm.

Using the free-free case as a reference, the tether length is increased from a quarter to a half wavelength in order to better match the tether ends with a wave node. Based on the modal animation of the simple free-free case, we observe that the first node in the tether does not coincide exactly with the edge of the resonator. As a result, subsequent nodes do not lie precisely at their theoretical values (i.e. 6 μm, 12 μm, 18 μm, etc). Therefore, an estimate of 6.4 μm is chosen as an appropriate tether length for the remainder of the boundary condition study.

4.3 Simple Model: Resonator Bar with Tethers

With an appropriate tether length established, the boundary condition study begins with a look at the geometry and transfer function of the resonator bar with tethers. While this simple geometry does not include much of the filter substrate or packaging, it still provides useful information and insight into the electromechanical behavior of a real device. The simple model is shown in Figure 4.2.
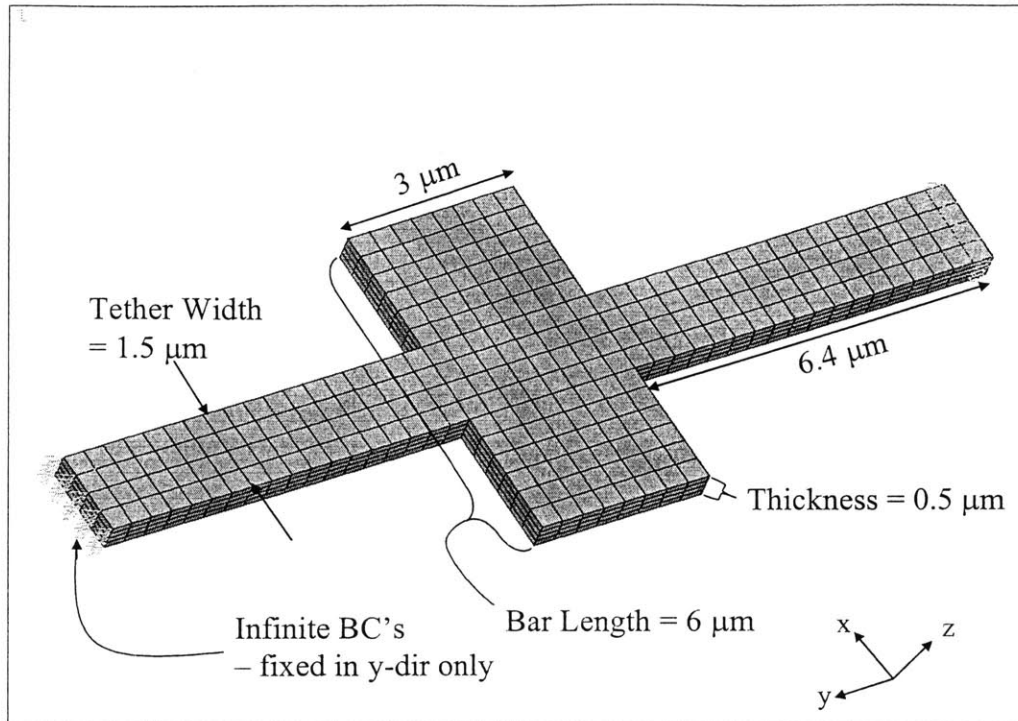
Figure 4.2: Simple model geometry.

In order to analytically solve for the electrical transfer function of the bar, many assumptions and simplifications are necessary to idealize the model. The addition of tethers represents a significant non-ideality characterizing the simple model. The effect of such a non-ideality is demonstrated through a comparison of the models' electrical transfer functions. Specifically, it is significant to observe the way and the degree to which the transfer function parameters such as resonant impedance and longitudinal center frequency vary between the models. Figure 4.3 shows the transfer function for the model in Fig. 4.2 overlaid on the electrical response of the geometry with no tethers.

Impedance vs Frequency
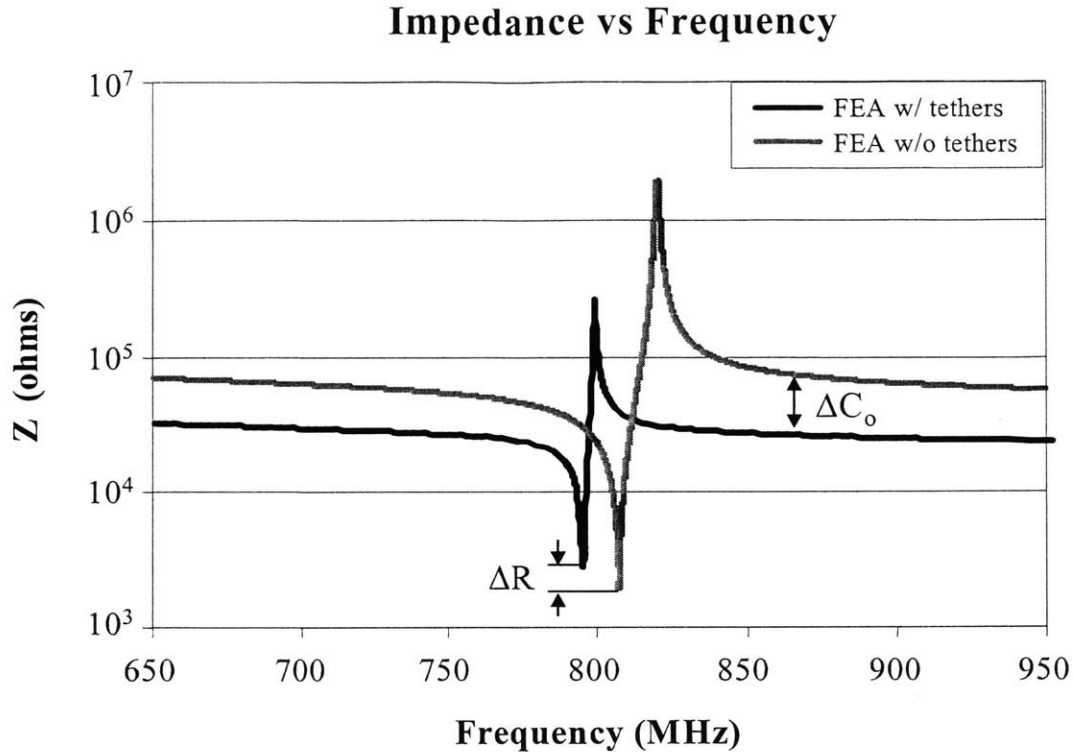
Figure 4.3: Electrical transfer function comparison. Simple geometry impedance overlaid on analytical response curve.

Comparing the transfer functions in Fig. 4.3, we observe that the addition of tethers has a significant effect on the absolute impedance value at resonance. Each curve exhibits an isolated longitudinal response having both a resonance and anti-resonance. With respect to circuit parameters, the main discrepancies between the transfer functions lie in their R and C_o values.

In the equivalent circuit model of Fig. 2.4, the R value represents the approximate impedance of the device at resonance. Comparing the two resonant impedances, we observe that the addition of tethers causes a 30% increase in the R value. This discrepancy can most likely be attributed to the difference in boundary conditions between the models. For the resonator geometry with no tethers, the sides of the bar are given an infinite boundary condition which restricts displacement in the x_2 (i.e. y) direction. This displacement restriction negates any Poisson effect in the x_2 direction as the bar displaces longitudinally. If a Poisson effect was present, a portion of the charge on the electrodes would be cancelled due to changes in the bar's width. For example, as the resonator extends there would normally be an associated Poisson compression through the width, canceling some of the total charge accumulated on the bar. Because this effect is not

present in the x_2 direction of the analytical model, the electromechanical coupling in the bar is more efficient, producing a lower resonant impedance.

Another difference between the transfer functions is their off-resonance impedance characteristics. With the addition of tethers to the resonator bar, the baseline impedance of the model drops significantly, thus accounting for the offset between the transfer functions. The presence of tethers causes the effective capacitive area of the device to increase, thus, decreasing the model's impedance over a wideband frequency range.

4.4 Initial Complex Model: 45 Degree Departure

4.4.1 Features and Boundary Conditions

The first complex model is designed and fashioned after the actual topology of Draper's current L-Bar resonators. This geometry, like its simple counterpart, has tethers which serve to acoustically isolate the resonator from the substrate. The tethers suspend the bar over an air gap created by a chemical etch of the silicon substrate. Figure 4.4 shows this model and an image of an actual L-Bar resonator as viewed through a scanning electron microscope (SEM).
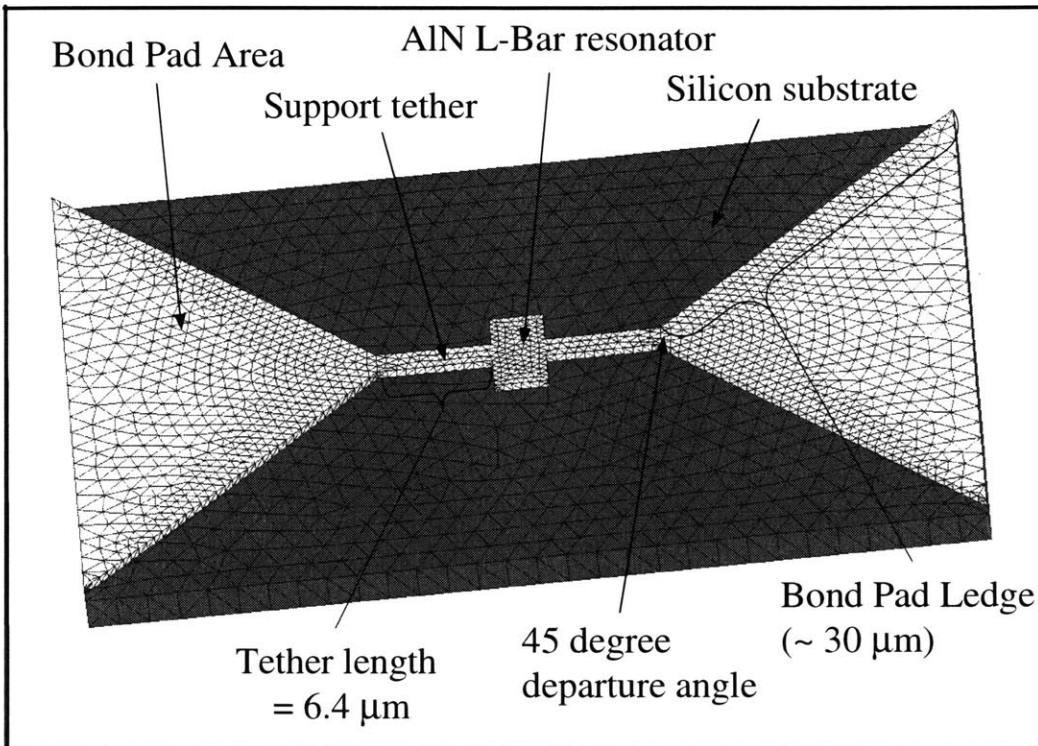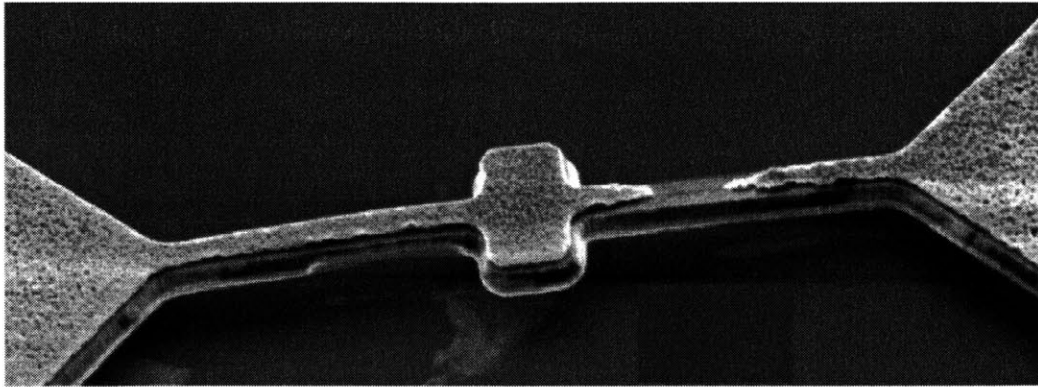
Figure 4.4: Top – SEM image of Draper's L-Bar resonator; Bottom - Initial electromechanical model for boundary condition study. Model includes a portion of the bond pads and Si/SiO$_2$ substrate.

The important features of this initial model are the substrate and the bond pad areas. The bond pads depart at a 45 degree angle from the support tethers. In the initial device design, this departure angle is chosen in order to produce a smooth transition between the filter components. The bond pad material sits on a thin film of silicon dioxide (SiO$_2$), approximately .5 μm thick. The SiO$_2$ serves as the sacrificial layer in the fabrication process. A chemical etch is used to release the resonator from the substrate, providing acoustic isolation for the bar. Because of the isotropic characteristics of the echant, however, the bond pad is undercut by the etching process.

This undercut is significant enough to create a ledge of bond pad material extending out over the Si layer below. The ledge is virtually free in space and as a result, facilitates the propagation of energy away from the system. For this reason, the presence of the ledge can be expected to influence the overall output of the device. Figure 4.5 provides a profile view of the model with the individual layers of the geometry labeled. The figure illustrates how the bond pad ledge is unconstrained over the majority of its surface area
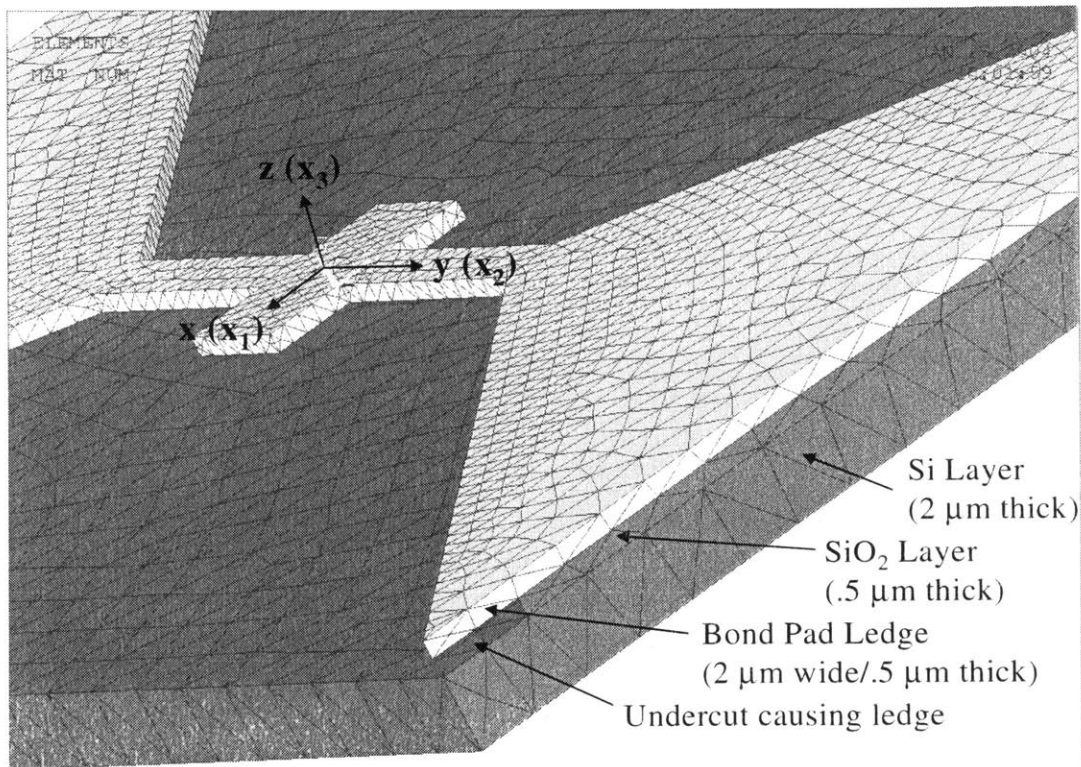
Figure 4.5: Model profile with material types and dimensions labeled

4.4.2 Modeling Theory

Because of the size discrepancy between the resonator and the substrate, an "infinite" boundary condition is utilized to constrain the periphery of the model. "Infinite" refers specifically to the assumption that, relative to the size of the resonator, the silicon substrate is modeled as dimensionally infinite in all directions. The infinite boundary conditions apply to those surfaces beyond which material would extend in the actual device. For any such surface, the infinite condition is applied by fixing the normal displacement degree of freedom (DOF) corresponding

to that surface. For example, in order to apply the infinite constraint to the base nodes of the silicon substrate in Fig. 4.5, the x_3 DOF are fixed, because the z-direction is the normal unit vector to that surface.

The ledge width is dictated by the characteristics of the current fabrication process. When the release etch is performed on the sacrificial layer below the resonator, the echant attacks the SiO_2 in an isotropic manner. Thus, the SiO_2 is etched laterally as well as through the thickness. The echant works downward until it reaches the silicon substrate which serves as an etch stop for the process. Once the echant hits the Si layer, its downward progress ceases, but SiO_2 etching continues laterally. The limiting parameter on this lateral etch is the width of the resonator, because the echant is applied until the resonator has been completely released from the substrate. As the echant works laterally through the SiO_2 to release the resonator, it also works underneath the bond pads creating a ledge around the periphery of the material, as shown in Figure 4.5. Because resonators are fabricated in batches, the width of the ledge is determined by the width of the largest resonator in the array being etched. Assuming the bar shown in Figure 4.4 is the largest of its array, the echant would work laterally from the edges of the bar, eventually converging at the middle. Therefore, the resonator is fully released after etching a distance equal to half the bar width. Thus, for the 3 μm wide bar, the width of the corresponding ledge would be approximately 1.5 μm. As noted in Figure 4.5, the ledge is assigned a value of 2 μm in order to simulate a worst case scenario.

4.4.3 Longitudinal Mode Shape

Studying the longitudinal mode shape of the structure indicates that the influence of the ledge motion is significant as predicted earlier. Below is a graphic illustrating how the displacement of the ledge compares to that of the resonator bar.
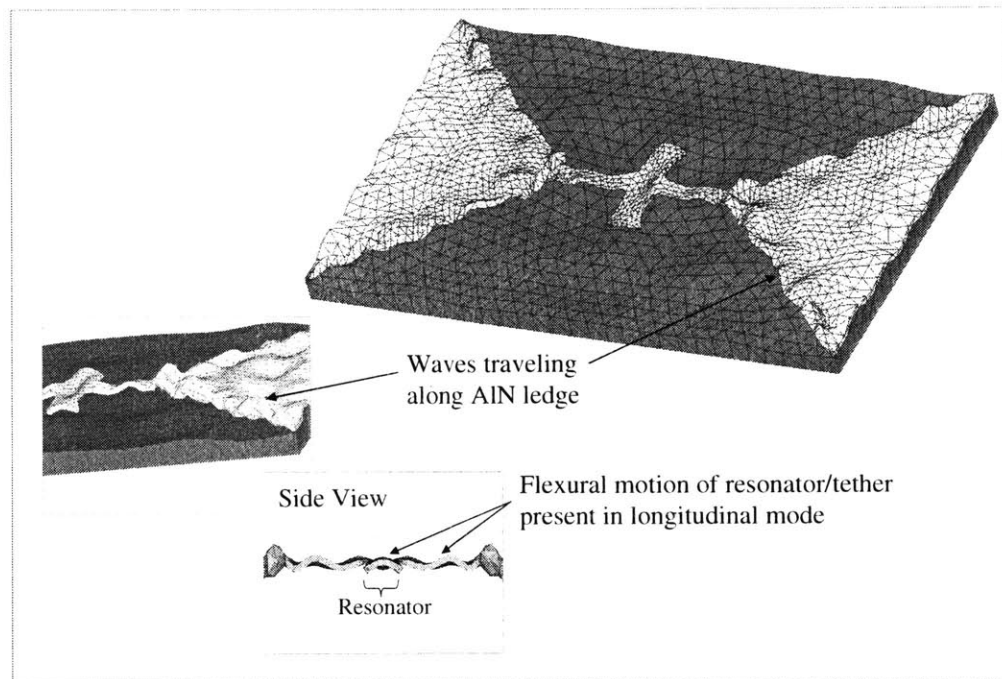
Figure 4.6: Longitudinal mode shape of initial FEA model. Modal animation shows significance of ledge motion relative to the resonator's displacement.

It is important to remember that the displacement of the mode shape is purposely exaggerated by the FEA software during animation in order to emphasize the motion. In reality, the absolute displacements of the bar, the tether, and the AlN ledge are on the order of nanometers. Relatively, however, the animation indicates that the ledge motion is comparable to that of the resonator, and, as a result, degrades the transfer function of the filter. In other words, the large amount of additional flexural motion present through the geometry pollutes the longitudinal mode shape, resulting in an increase in impedance at resonance and thus a decrease in filter performance.

70

4.4.4 Electrical Transfer Function

Besides the primary resonant frequency, several additional modes appear to have longitudinal motion. Because of the complexity of the model, irregular motion present in the bulk material has the capability to produce longitudinal displacement in the resonator at several different frequencies. In order to investigate the effect of this irregular motion in the electrical domain, a harmonic analysis is performed and the corresponding impedance transfer function for the model is obtained. Figure 4.7 shows this transfer function and illustrates how it is degraded relative to the impedance characteristic of the simple model. Once again, a mechanical Q of 1000 is prescribed for the simulations.

Impedance vs Frequency
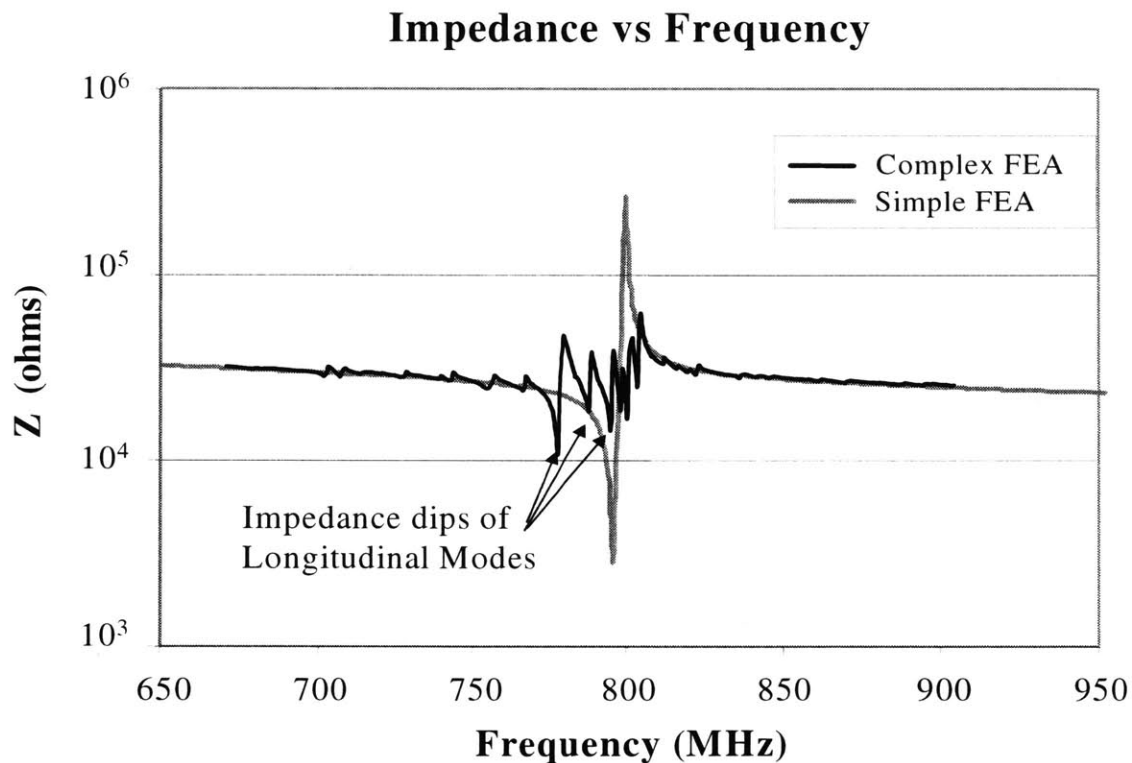
Figure 4.7: Plot of simulated impedance characteristics: simple and complex FEA models

Relative to the transfer function of the simple model, the impedance characteristic for the complex model is degraded dramatically. As the graph indicates, the complex model does not produce a dominant, well isolated longitudinal mode. The primary impedance dip, occurring at approximately 778 MHz, is not significantly lower than spurious modes adjacent to it in the

graph. Each of the five dips in the transfer function represents the characteristic impedance of a distinct longitudinal mode shape of the structure.

4.5 New Complex Model: 90 Degree Departure

For a sweep range of approximately 230 MHz, the initial complex model, shown in Fig. 4.4, produces over 260 distinct mode shapes. Furthermore, as evidenced by the FEA data series in Fig. 4.7, several modes are characterized by electromechanical coupling that is strong enough to significantly lower the impedance of the bar. As a result, a primary goal for future filter topologies is to reduce the effect of these spurious modes and isolate the filter's passband about one distinct longitudinal frequency. With this goal in mind, a new geometric configuration is introduced which potentially provide better acoustic isolation and a reduction in the significance of spurious modes, thus producing a cleaner electrical transfer function. The new configuration is simply a modified form of the initial geometry. The modification centers on the departure angle of the bond pads from the tether supports. Rather than having the bond pad area lithographically cut to depart at a 45 degree angle from the x-axis, in the new topology, this material extends away from the tether supports parallel to the x-axis (i.e. 90 degree angle) as depicted in Figure 4.8.
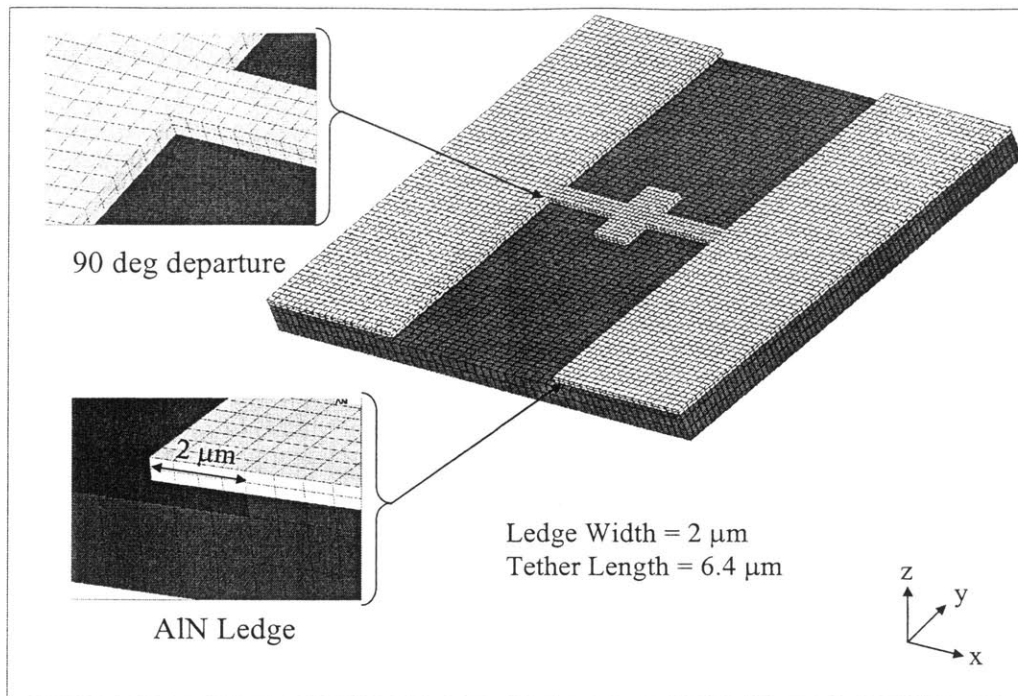
Figure 4.8: New complex configuration with 90 degree departure of bond pads.

Other than the difference in departure angle of the bond pads, the boundary conditions and dimensional parameters are consistent between the two configurations. As described in the previous section, displacement constraints are applied to the outer surfaces of the 90 degree model to mimic an infinite substrate. Both the tether length and the ledge width are maintained at their original values of 6.4 μm and 2 μm, respectively. These model characteristics are kept constant in order to facilitate a legitimate comparison between the transfer functions of the differing configurations. In Figure 4.9, the impedance characteristics of both the new and old topologies are shown.

Impedance vs Frequency
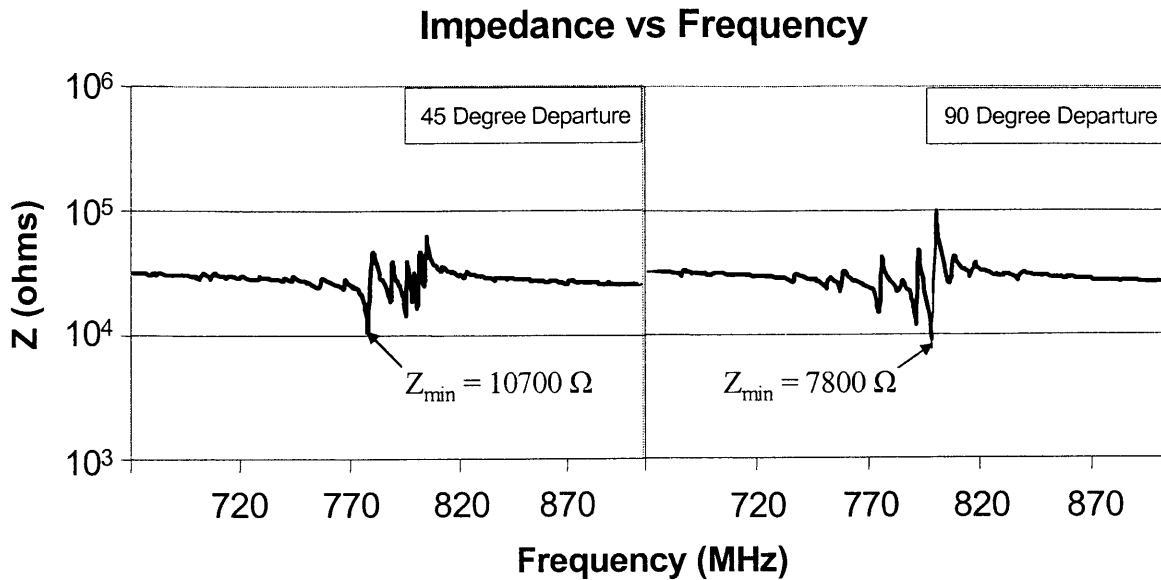
Figure 4.9: Plots of transfer functions for 45 and 90 degree configurations

The transfer function for the new configuration, shown on the right of the figure, indicates that the modification of the departure angle improves the electrical output of the bar. The longitudinal mode having a center frequency of approximately 799 MHz couples the electrodes better than the other modes around it. Furthermore, of the spurious modes producing a significant response at their resonance, only two seem to have impedances comparable to that of the predominant mode. This contrasts with the output of the 45 degree geometry whose transfer function is characterized by four significant spurious modes. For the 90 degree configuration, the magnitude of the impedance at the primary longitudinal mode is approximately 7800 Ω. This value represents about a 30 % decrease in device impedance as compared to the output of the initial configuration. As before, the modal animation can be used to illustrate these results. Fig. 4.10 shows the primary longitudinal mode shape of the 90 degree configuration.
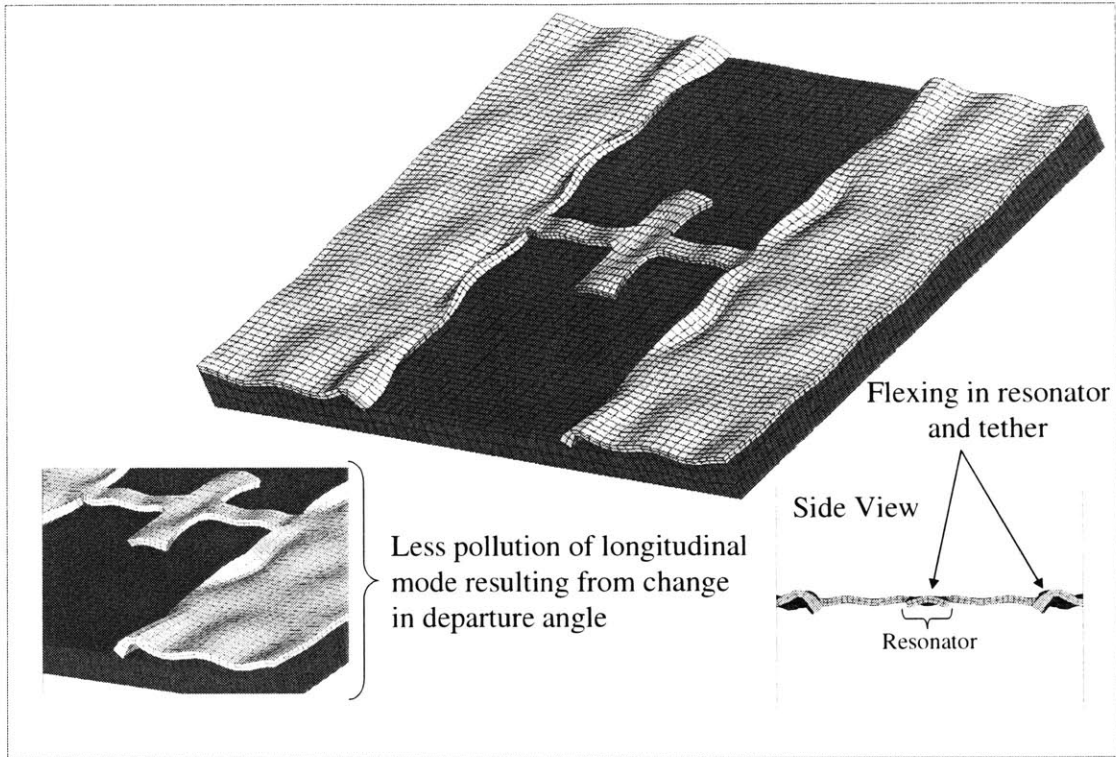
Figure 4.10: Longitudinal mode shape of 90 degree geometry. The image shows the bar in tension.

Although the motion of the resonator does not yet correspond to the ideal longitudinal mode shape, it is significantly improved relative to the displacement of the original configuration as depicted in Fig. 4.6. Flexural waves are present in both the tethers and the ledge of the model shown above, but as the side view indicates, this motion does not have as great an effect on the resonator's displacement. As a result, because of this "cleaner" longitudinal mode shape, the resonator passes more current at its operational frequency. In addition, this topology suppresses the output of the spurious modes more effectively and thus, reduces their impact on the overall transfer function. For this reason, the new configuration represents a viable alternative to the 45 degree geometry and therefore, could prove valuable in future filter design.

75

4.6 Comparison of Model Parameters

As the previous sections demonstrate, with respect to the longitudinal mode, the simple model produces a transfer function comparable to that of both the idealized and more complex geometries. Table 4.1 gives a break-down of the key features of each model's transfer function.

Illustration/Description of BC's	Impedance (Z, ohms) Q = 1000	Center Frequency, Spurious Modes (MHz)	Notes
Analytical Bar	1874	ω_C : 807 Spurious modes: None	• Sweep Range: 600-1000 MHz • No tethers • Infinite BC's along right and left sides
Fixed-Fixed (x direction)	2715	ω_C : 805 Spurious modes: None	• Sweep range: 600-1000 MHz • Tether length: 6.4 μm • Infinite BC's at tether ends
45 Degree Departure	10685	ω_C : 778 4 spurious modes: 788, 795, 798, 800	• Sweep range: 670-905 MHz • Ledge not shown • Bond pad area not drawn to scale • Tether length: 6.4 μm
90 Degree Departure	7804	ω_C : 799 2 spurious modes: 775, 792	• Sweep range: 670-905 MHz • Ledge not shown • Bond pad area not drawn to scale • Tether length: 6.4 μm
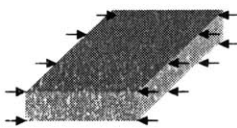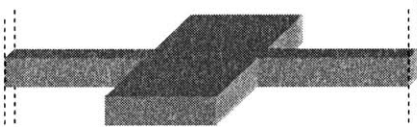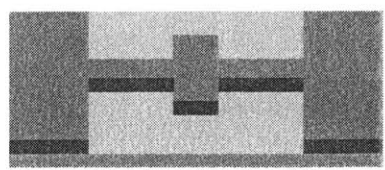
Table 4.1: Comparison of key electrical transfer function parameters.

The first column of data gives the value of the impedance at resonance for each model assuming a mechanical Q of 1000. As previously discussed, there is approximately a 30% increase in impedance due to the addition of tethers to the analytical model geometry. This percentage corresponds closely to the Poisson's ratio for AlN, indicating that the difference in boundary conditions explains the increase. Comparing the simple model to the more complex geometries, we observe another jump in the impedance due to the presence of additional non-idealities such as the bond pads and substrate.

The second column notes the center frequencies of the primary longitudinal modes as well as the frequencies of significant spurious responses. Regardless of the topology, the longitudinal center frequency falls consistently into a narrow range of values. With the exception of the 45 degree configuration, the geometries produce center frequencies within a percent difference of each other. The 45 degree geometry yields a primary longitudinal mode whose frequency value is approximately 3% different from the other configurations. This invariance of the resonant frequency indicates its robustness to changes in the model geometry. In contrast, the appearance of spurious modes is highly dependent on the complexity of the model. For both the analytical and simple models, no spurious modes exist and, consequently, the longitudinal mode shape is well isolated. In the complex geometries, however, substrate motion produces transfer functions with significant spurious responses.

4.7 Transfer Function Data: Simulated vs. Actual Results

The table in Section 4.6 provides a range of error for the simple model relative to other FEA geometries. In order to fully qualify the simple model, we now compare its electrical transfer function to actual resonator data. A few modifications are made to the geometry of the simple model in order to match it to the actual resonator. Due to the limitations associated with the experimental testing of Draper's resonators, only a few geometries produce data which facilitates further analysis. From the first batch of resonators tested, the 10x5x0.5 μm geometry yields the most useful transfer functions. Therefore, the FEA bar is changed to match these dimensions. Also, the tether length and width are modified to 6 μm and 1 μm, respectively. Furthermore, in

order to better match the operational frequency of the actual resonator, the metal electrode geometry, including the density and stiffness, is modeled in addition to the AlN. The profile view of the model in Fig. 4.11 shows the metal-piezoelectric-metal configuration characteristic of an actual L-Bar resonator [5].

Side View

Ni - .24 μm thick

AlN - .5 μm thick

Mo - .15 μm thick

Resonator/Tether Dimensions:
L_{res} = 10 μm
W_{res} = 5 μm
L_{tether} = 6 μm
W_{tether} = 1 μm
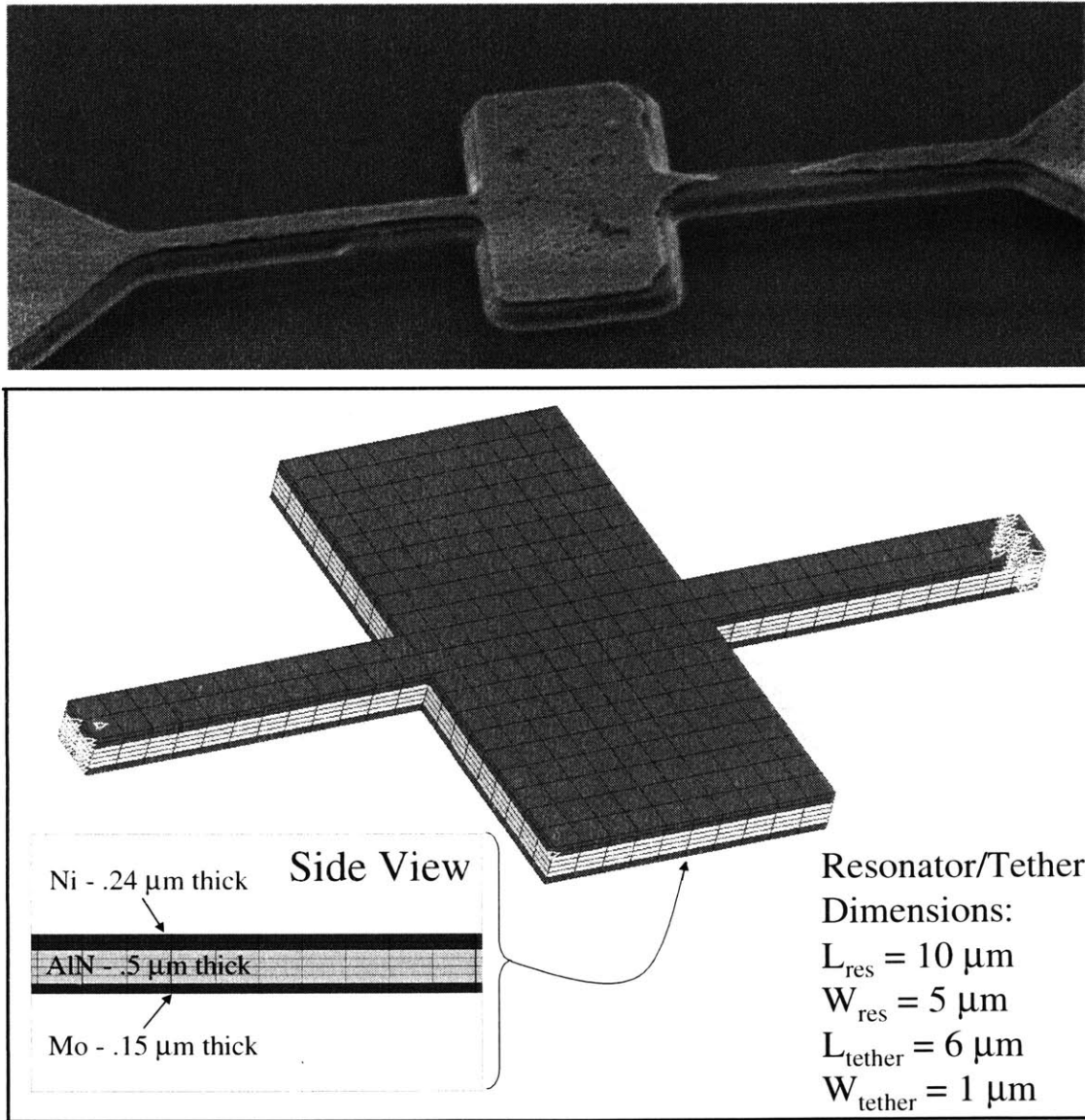
Figure 4.11: SEM image and FEA model geometry of 10 μm bar with metal electrodes. Tether dimensions and Q (i.e. 125) modified to match real structure

Because direct impedance measurements cannot be obtained in experimental tests, the response of the filter is measured in terms of scattering parameters (S-parameters). S-parameters are reflection and transmission coefficients which measure the performance of an electrical device

operating under linear conditions in the MHz frequency range. For this study, the S_{21} transmission coefficient is used to determine the electrical response of Draper's L-Bar resonators. The S_{21} parameter, characterized by a magnitude and phase, is calculated from the resonator bar's output voltage ratio (i.e. V_{out}/V_{in}). The equation for the magnitude of S_{21} is written as

$$|S_{21}| = 20 \cdot \left[\log_{10}\left(\frac{V_{out}}{V_{in}} \right) - \log_{10}\left(\frac{V_{out.sc}}{V_{in}} \right) \right] = 20 \log\left(\frac{2 \cdot V_{out}}{V_{in}} \right) \qquad (4.1)$$

where $V_{out.sc}$ is the voltage out in the short circuit case - $V_{out.sc} = V_{in}/2$. In order to obtain the voltage ratio, the resonator is placed electrically in series with a source and load resistance. The modified filter topology and its corresponding equivalent circuit are shown in Fig. 4.12.
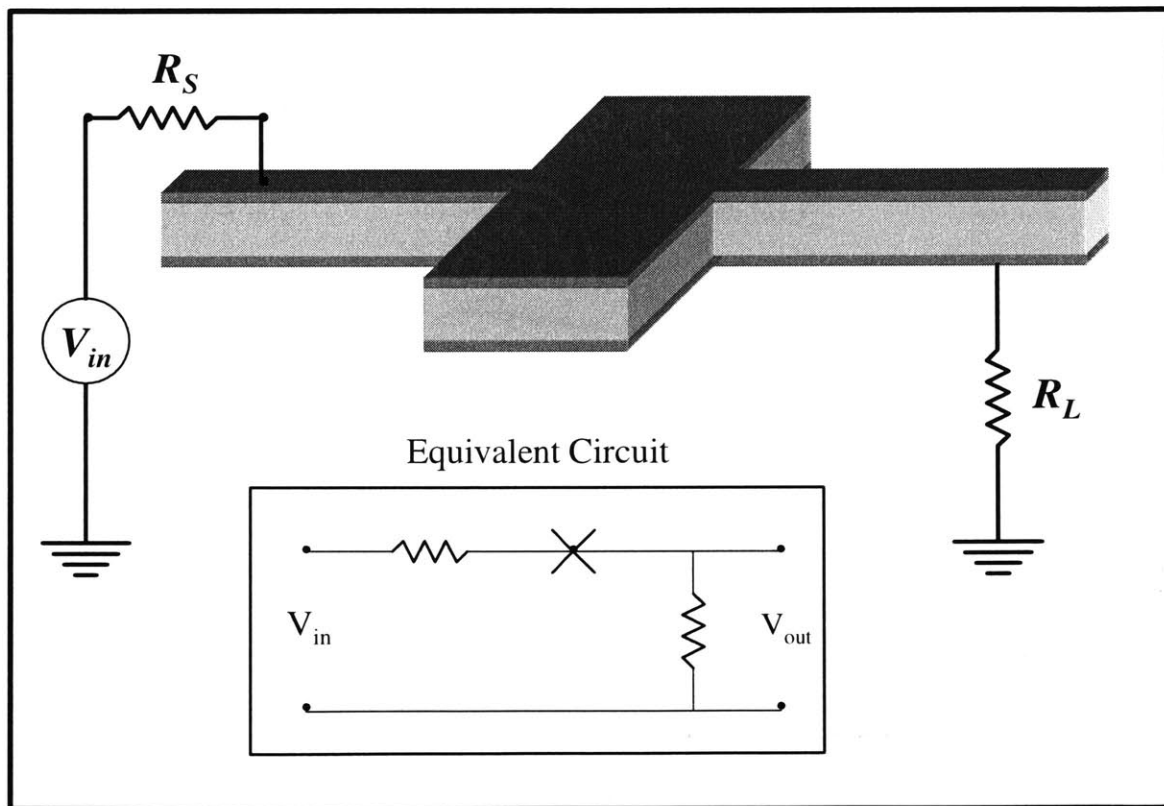
Figure 4.12: FEA model with passive resistor elements and equivalent circuit. For initial designs, R_S and R_L are 50 Ω.

For simplicity, a sinusoidal input voltage of 1 V is used for the simulations. The output voltage is measured across the load resistor and used to calculate the S_{21} parameter. Experimental S_{21}

data measured from the actual device gives resonator Q of approximately 125. As a result, the mechanical Q for the FEA model is set to this new value. With these adjustments made to the 10x5 μm resonator model, the simulated electrical transfer function is generated and found to correspond closely to the actual results data. Fig. 4.13 shows the simulated transfer function overlaid on the actual data [9].

S₂₁ vs Frequency
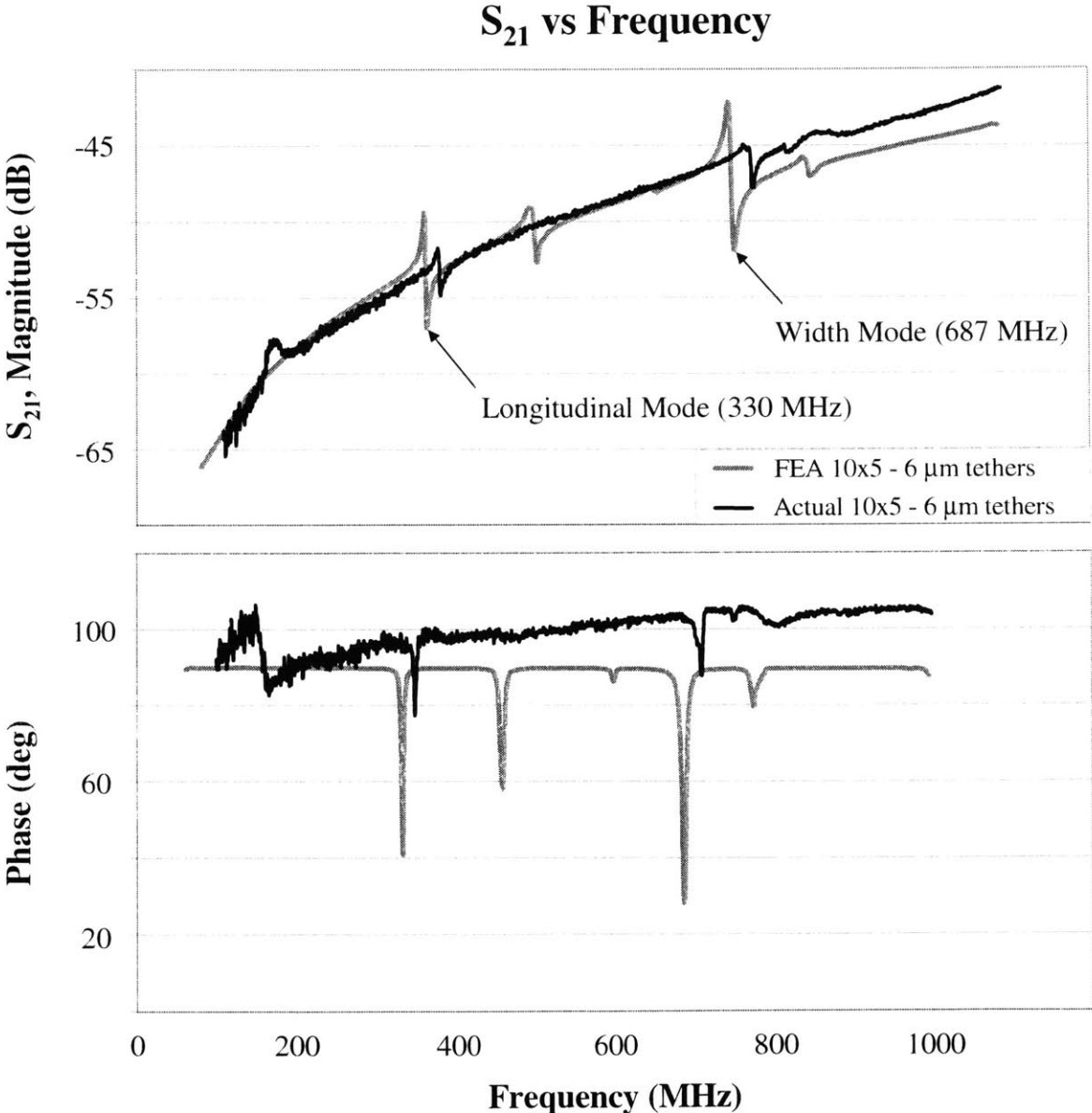
Figure 4.13: S_{21} plot of simulated and actual data. Longitudinal and width modes labeled for simulated curve

4.8 Variation of Tether Length: Impedance Analysis

At the beginning of the boundary condition study, an appropriate tether length was established based upon the approximate location of longitudinal wave nodes along the tether. With the quantitative FEA approach now firmly established, we attempt to verify the initial choice of 6.4 μm for the tether length of the simple L-Bar resonator. This final task of the boundary condition study is accomplished by varying the tether length in half micron increments and obtaining the simulated resonant impedance of each geometry.

Impedance vs. Tether length
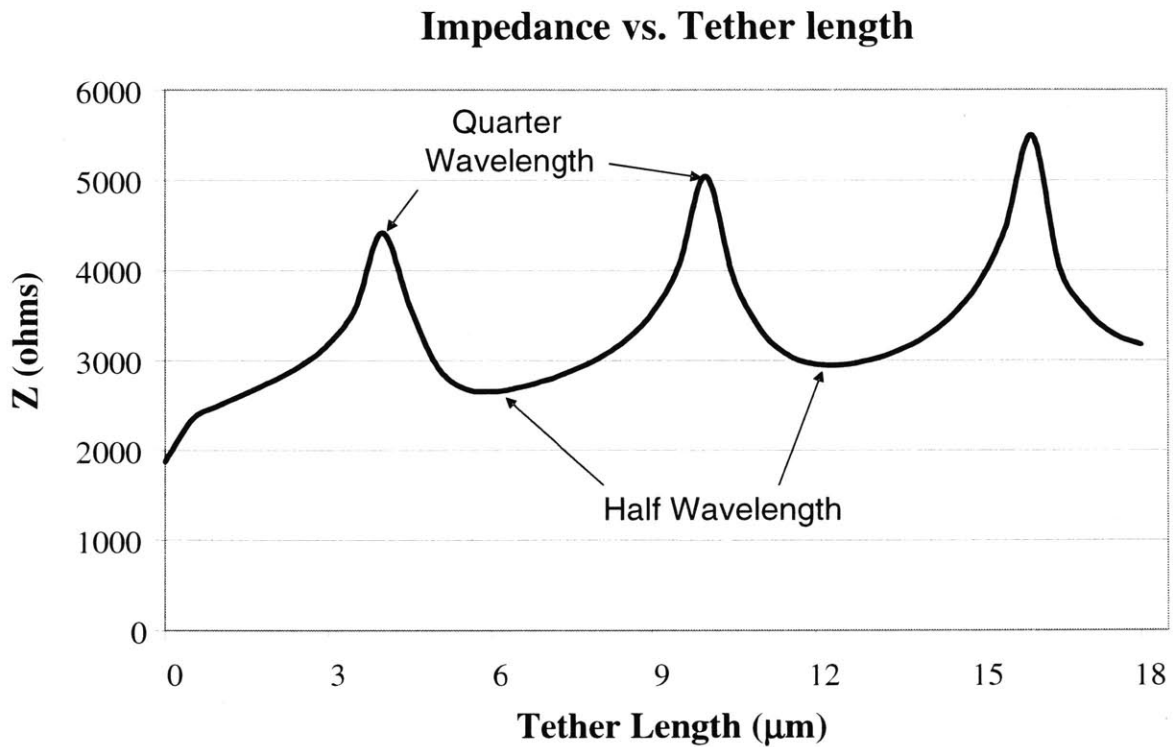
Figure 4.14: Plot of impedance versus tether length for simple model. 6x3 μm resonator geometry and 1.5 μm wide tether used for simulations; Q = 1000.

The graph illustrates that the impedance of the resonator is significantly dependent upon the length of its supporting tethers. For example, an increase in impedance occurs when the tether length corresponds approximately to a quarter wavelength increment. At tether lengths of 4 and 10 μm, the impedance reaches a peak value and drops off quickly at lengths above and below these values. This trend is most likely caused by poor coupling between the resonator and

support tethers. At these lengths (i.e. 1/4λ, 3/4λ, 5/4 λ, etc), the vibration of the resonator is out-of-phase with the wave traveling through the tether, causing destructive interference and a subsequent canceling of charge on the electrode. This cancellation of charge causes a corresponding impedance rise at the quarter wavelength increments.

A trend is also observed for geometries with half wavelength tethers. The response at these tether lengths correspond to minimum impedance values on the plot. For half wavelength increments (1/2λ, λ, 3/2λ, etc), the waves in the tether resonate in-phase with the sinusoidal motion of the bar. The acoustic waves traveling in the resonator and the tethers combine constructively, thus maximizing their electromechanical coupling and reducing the impedance of the device.

As illustrated by Fig. 4.14, for each successive half wavelength increment, the associated impedance "trough" rises slightly, indicating the smaller tether values produce better a better response at resonance. Furthermore, the graph verifies the results of Ch. 3, which demonstrated that the resonator geometry with no tethers represents the ideal boundary conditions. However, this is not a realistic model for actual L-Bar resonators. The next minimum impedance value along the curve corresponds to a tether length of approximately $\frac{1}{2}\lambda_{res}$. For the 6 μm resonator bar, based on the quarter wavelength increments of 4 μm and 10 μm, a new half wavelength estimate of 7 μm will be used in future models.

Chapter 5

Extracting Equivalent Circuit Model Parameters

5.1 Equivalent Circuit Model Theory

In general, an equivalent circuit model is useful because it allows an electromechanical device to be incorporated into a purely electrical system. In Ch. 2, an equivalent circuit for the resonator geometry is derived analytically. This equivalent circuit, known as the Butterworth van Dyke (BVD) model, is commonly used by filter designers to represent the electrical transfer function of filter elements (i.e. resonators) over a wide band of frequencies [10]. As the analytical derivation demonstrates, the BVD model accurately describes the electromechanical behavior of the resonator bar without tethers. However, an actual L-Bar resonator has support tethers connecting it to the substrate and therefore, yields a different set of circuit parameters. As noted in the boundary condition study, both the impedance at resonance (R) and the through capacitance (C_o) increase with the addition of tethers. The L and C values of the equivalent circuit also change because the extra mass of tethers causes a shift in resonant frequency. The BVD model is shown again below with its element parameters labeled.
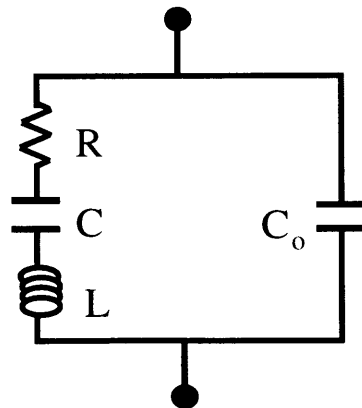
Figure 5.1: Butterworth van Dyke equivalent circuit model

Draper's resonators are designed to be integrated into larger electrical circuits such as frequency filters and oscillators. Consequently, there is a need to determine the new BVD element parameters corresponding to the resonator geometry with tethers. In this chapter, we introduce a method for extracting the BVD element values from measured data parameters. Using a simulated transfer function, specific values from the data curve are used to determine the new R, L, C and C_0. Also, in order to verify the extraction method, the mechanical Q prescribed in the FEA model is compared to the circuit Q calculated from the new BVD parameters.

5.2 BVD Parameter Extraction: Impedance Transfer Function

To maintain continuity with previous impedance data, the method for BVD parameter extraction is applied first to a simulated transfer function for a resonator without passive elements. The first step in the process is to define the complex impedance function characterizing the BVD model. The impedance function of the equivalent circuit in Fig. 5.1 is expressed as

$$Z_{BVD} = \frac{1}{sC_o} \frac{s^2 LC + sRC + 1}{s^2 LC + sRC + 1 + C/C_o} \tag{5.1}$$

C_o represents the resonator's through capacitance, which dominates the off-resonance impedance characteristic of the model. The R, L, and C parameters capture the mechanical resonance and piezoelectric behavior of the bar at the longitudinal mode. The longitudinal frequencies corresponding to the resonance and anti-resonance of the BVD model are found by solving for the zeros and poles of (5.1). For a typical resonator, the loss is small and thus, for convenience, we initially assume a lossless system (i.e. R $\approx$ 0). Employing this assumption, the two equations needed to solve for the zeros and poles are

$$s^2 + \frac{1}{LC} = 0 \tag{5.2}$$

$$s^2 + \frac{1}{L}\left(\frac{1}{C} + \frac{1}{C_o}\right) = 0 \tag{5.3}$$

where s is the frequency domain parameter equivalent to the complex expression jω. Solving these equations, we find that the solution yields a complex conjugate zero pair followed closely by complex poles. Only one peak occurs for each pair because the complex conjugates have the same magnitude. The frequencies corresponding to the minimum and maximum impedance of the longitudinal mode are calculated according to

$$\omega_S = \frac{1}{\sqrt{LC}} \tag{5.4}$$

$$\omega_P = \omega_S \sqrt{1 + \frac{C}{C_o}} \tag{5.5}$$

These values are referred to as the series and parallel resonant frequencies. These values are significant, because they can be read directly from a plot of measured data. As such, the unknown L and C parameters are defined in terms of ω_s and ω_p. Taking the difference between (5.4) and (5.5), dividing the result by the series resonant frequency and rearranging terms, we arrive at the following equations for the unknown parameters.

$$C = C_o \cdot \left(\left(1 + \frac{\omega_P - \omega_S}{\omega_S}\right)^2 - 1\right) \tag{5.6}$$

$$L = \frac{1}{\omega_S^2 C} \tag{5.7}$$

C_o is found by fitting the off-resonance impedance characteristic of the data to the function $1/\omega C_o$ and then verifying this extracted value by comparing it to an analytical calculation based on the capacitor area. With these parameters defined, we recall that our device is not actually lossless and therefore, has some non-zero impedance at the series resonance. To determine this value, consider the fact that, at ω_s, the *RLC* branch dominates the impedance transfer function of

the BVD model. As a result, at frequencies near resonance, Z(ω) for the model can be effectively reduced to that of a series *RLC* circuit.

$$Z_{RLC} = R + j\left(\omega L - \frac{1}{\omega C}\right)$$ (5.8)

From (5.8), we can solve for the impedance at ω_s directly. Substituting (5.4) for ω in the equation above, the imaginary term drops out, and we find that the impedance at the series resonance is equal to R of the BVD model. In reality, $Z(\omega_s)$ is equal to the sum of R and the through impedance calculated from the resonator's C_0 value (i.e. $Z_{cap} = 1/\omega C_0$). For an L-Bar resonator 6 μm in length, the series resonant frequency is approximately 800 MHz with a Co on the order of 10^{-15} F. Based on these values, a reasonable estimate for Z_{cap} is approximately 20 kΩ. This impedance value is about an order of magnitude larger than the typical R of a high Q resonator. Therefore, the assumption that $Z_{BVD}(\omega_s) = Z_{RLC}(\omega_s) = R$ is feasible. As a result, the value of R can be read directly from a plot of measured data as the impedance value at ω_s.

With all the BVD element values expressed in terms of measured parameters, we now solve for the Quality factor of the resonator to check the effectiveness of the extraction method. Nilsson [4] notes that, by definition, Q is the ratio of the resonant frequency to the filter bandwidth. This bandwidth is calculated by taking the difference of the half-power frequencies. These frequencies are defined as those at which the magnitude of the impedance is equal to $\sqrt{2}\,R$. Taking the magnitude of (5.8) and setting it equal to $\sqrt{2}\,R$, we arrive at the following quadratic equation.

$$\left(\omega L - \frac{1}{\omega C}\right)^2 - R^2 = 0$$ (5.9)

The roots of this difference of squares are the half-power frequencies. Solving (5.9) yields

$$\omega_{1,2} = \sqrt{\left(\frac{R}{2L}\right)^2 + \frac{1}{LC}} \pm \frac{R}{2L} \tag{5.10}$$

As stated above, the half-power frequencies define the bandwidth of the filter response and therefore, the quality factor. Taking the difference between ω_1 and ω_2, we find that the bandwidth can be expressed as

$$\beta = \omega_1 - \omega_2 = \frac{R}{L} \tag{5.11}$$

With the bandwidth defined in this manner, the resonator Q becomes

$$Q = \frac{\omega_S}{\beta} = \frac{\omega_S L}{R} \tag{5.12}$$

In terms of the measured parameters, the equation for the Quality factor takes the form

$$Q = \left[\omega_S R C_o \cdot \left(\left(1 + \frac{\omega_P - \omega_S}{\omega_S} \right)^2 - 1 \right) \right]^{-1} \tag{5.13}$$

Figure 5.2 is a simulated transfer function showing where the important measured parameters are found on a data plot.

Impedance vs Frequency
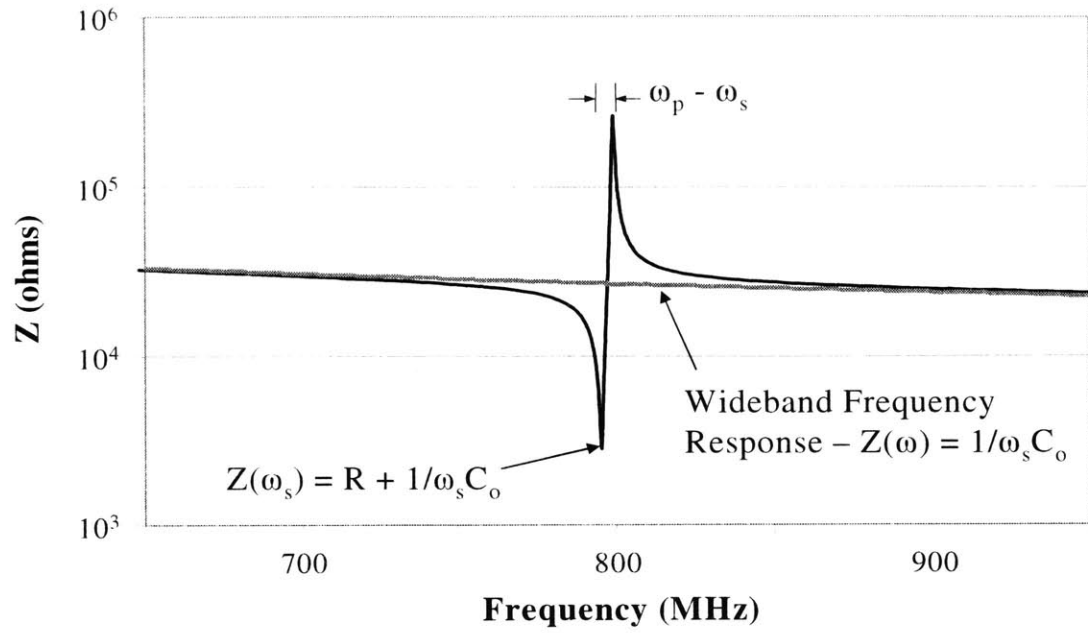
Figure 5.2: Plot of resonator impedance versus frequency. Key measured values used for circuit parameter extraction include ω_s, ω_p, C_o, and R.

5.3 BVD Parameter Extraction: S_{21} Transfer Function

As previously mentioned, a filter designer is not able to experimentally determine the transfer function of an actual device in terms of impedance. As a result, the procedure for the parameter extraction is now applied to the S_{21} transfer function of a filter topology similar to that introduced in Section 4.7. Fig. 5.3 shows the equivalent circuit of the geometry in Fig. 4.12.
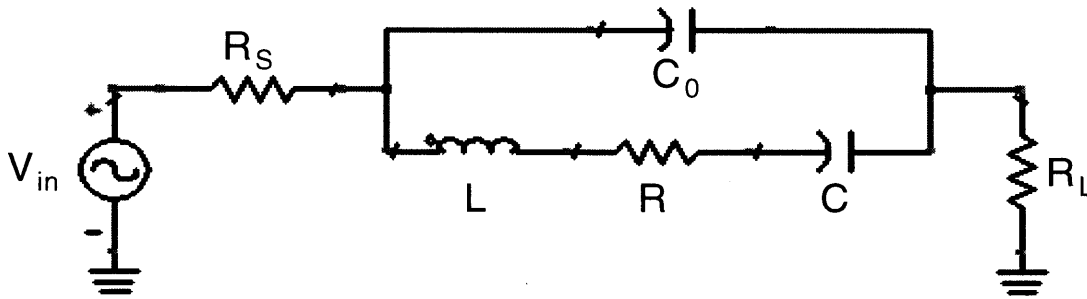
Figure 5.3: BVD model in series with source and load resistors. This configuration is needed to measure an output voltage (i.e. $V(R_L)$) and obtain an S_{21} transfer function

Extracting the BVD parameters from a plot of measured S_{21} data is analogous to the process described in the previous section. First, to find R, the S_{21} value is measured at ω_s. At or near the series resonant frequency, the equivalent circuit of Fig. 5.3 can be simplified to the following.
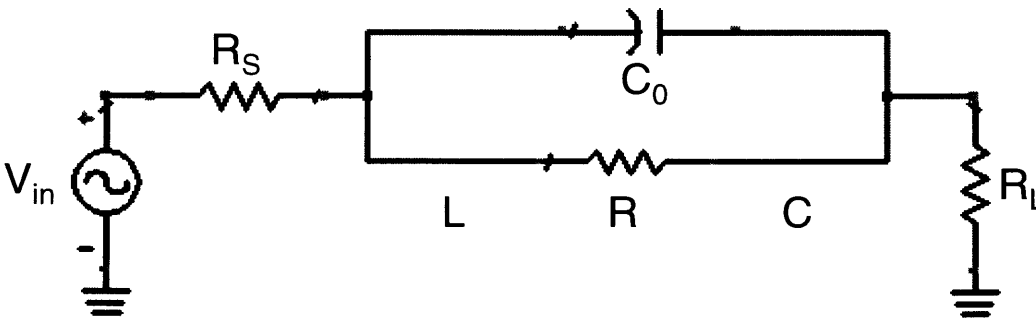
Figure 5.4: Simplified circuit model used to fit the impedance (i.e. R) *at resonance*.

At resonance, the impedances of the L and C components of the BVD model cancel, leaving only the R in parallel with the through capacitance, C_o. For a high Q filter, we can assume that $R \ll 1/\omega_s C_o$ at ω_s and consequently, R can be determined by a simple voltage divider calculation. The equation for R is then

$$R = 50 \left(\left| \frac{V_{in}}{V_{out}} \right|_{res} - 2 \right) \tag{5.14}$$

Recalling the definition for the magnitude of S_{21} in Ch. 4, we manipulate the form of (4.1) and calculate $\left| \frac{V_{in}}{V_{out}} \right|_{res}$ according to the following

$$\left| \frac{V_{in}}{V_{out}} \right|_{res} = \frac{2}{10^{S21/20}} \tag{5.15}$$

With the voltage ratio known at resonance, (5.14) becomes

$$R = 50 \cdot 2 \left(\frac{1}{10^{|S21|/20}} - 1 \right) \tag{5.16}$$

For a non-idealized geometry including electrical parasitics, the parallel capacitance, C_o, may become significant in relation to R, making it necessary to account for its effect. In this case, (5.14) would be modified to

$$\left| R \parallel \frac{1}{j\omega_s C_o} \right| = 50 \left(\left| \frac{V_{in}}{V_{out}} \right|_{res} - 2 \right) \tag{5.17}$$

It is important to note that (5.17) fits R based only on the magnitude of the simulated data. For actual S_{21} measurements, a complex fit of the data is the most appropriate. This is accomplished by fitting the real and imaginary parts simultaneously to a constant magnitude and zero phase impedance.

No calculation is necessary to determine ω_s and ω_p, as these values can be measured directly. However, the wideband frequency response of the resonator must be fit in order to find the off-resonance capacitance, C_o. The equation necessary to fit the S_{21} data and calculate the through capacitance is

$$C_o = \frac{1}{j\omega x} \qquad \text{where } x = 100\left(\frac{1}{10^{S21/20}} - 1\right) \qquad (5.18)$$

Once all the required measured parameters are determined, as before, in order to complete the parameter extraction, the remaining BVD element values are calculated according to Eqs (5.6), (5.7), and (5.12). The simulated electrical response of the circuit configuration in Fig. 5.3, is recorded in dB, and graphed versus frequency, producing the following S_{21} plot.

S_{21} vs Frequency
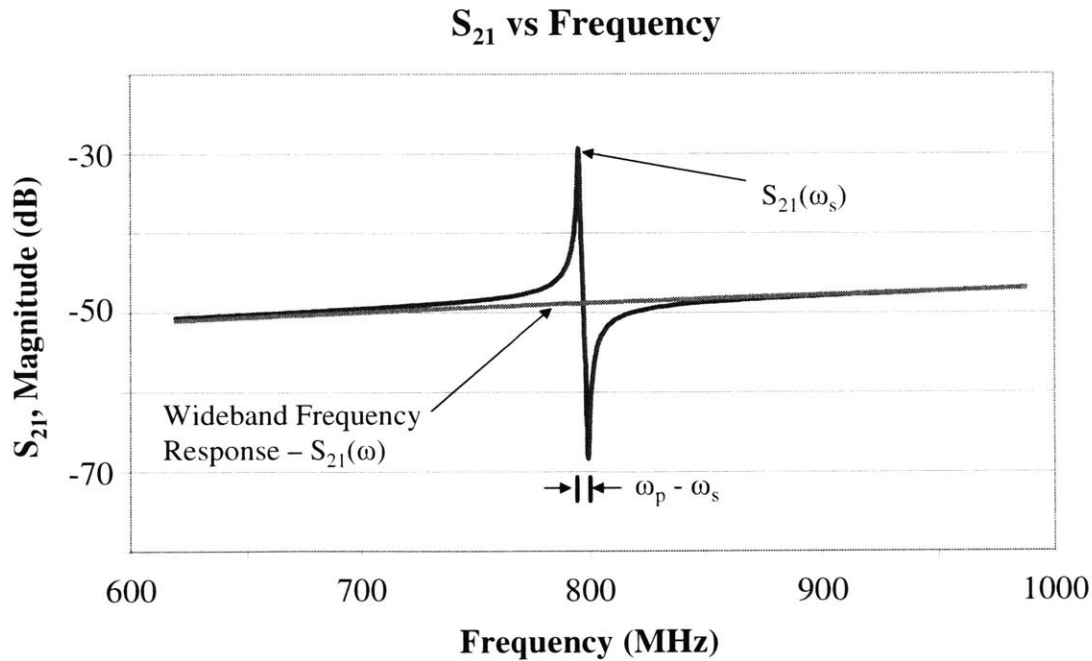
Figure 5.5: Simulated S_{21} plot with important measured parameters labeled.

By virtue of the S_{21} calculation, the resonant impedance drop occurring at the longitudinal natural frequency now corresponds to a resonant peak on the response plot. Likewise, the anti-resonance peak of the Z(f) plot is analogous to the minimum value of the S_{21} curve.

5.4 Parameter Extraction Example

In the following example, the circuit element values for the longitudinal and width modes of a 10 μm bar are calculated from a simulated S_{21} transfer function. Shown below is the simulated S_{21} plot for the 10x5 μm geometry with an input mechanical Q of 1000. Overlaid on the S_{21} curve is the through capacitance fit of the wideband frequency response.

Simulated S_{21} of Draper Resonator
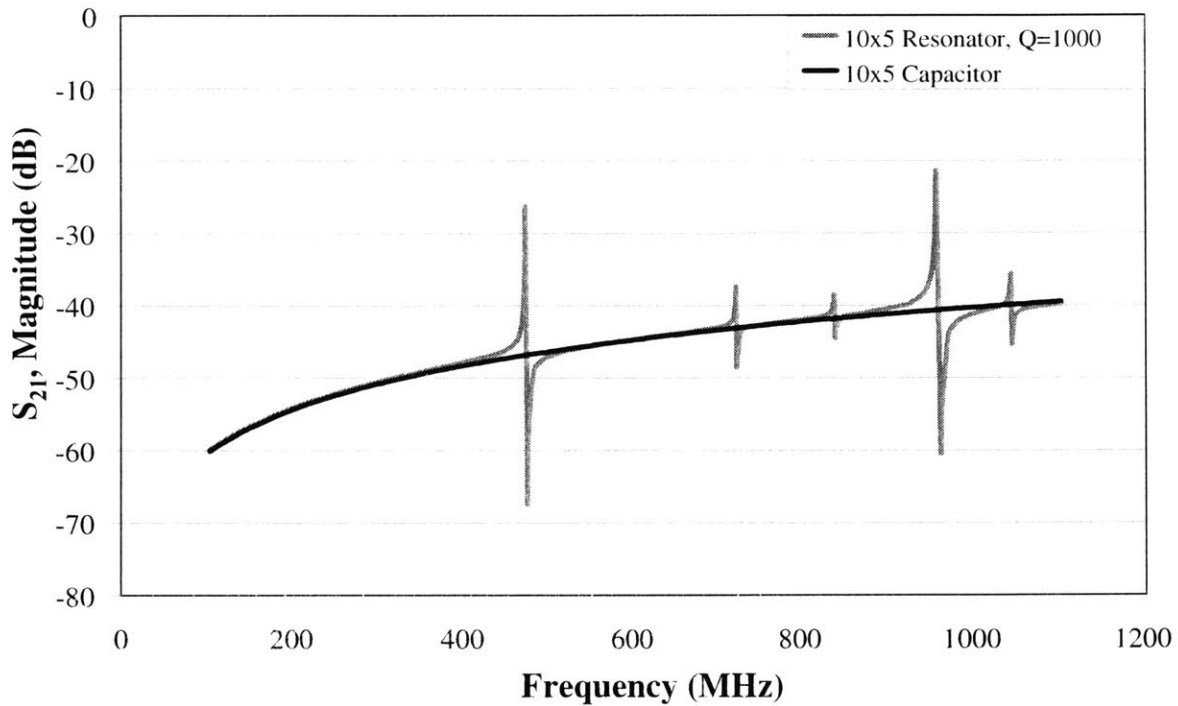
Figure 5.6: Simulated S_{21} for FEA mechanical resonator loaded in the series configuration of Fig. 4.12. The resonator bar is 10x5x0.5 μm, with tethers that are 1.5 μm wide and 11 μm long. AlN material parameters are used, and metal electrodes are not modeled for this simulation.

Following the procedure from the previous section, we first calculate the R value of the BVD circuit characterizing the longitudinal mode. Using Eq. (5.16), for $S_{21}(\omega_s)$ equal to -26.29 dB, R is calculated to be

$$R = 50 \cdot 2\left(\frac{1}{10^{-26.29/20}} - 1\right) = 1963 \ \Omega$$

Next, the series and resonant frequencies of the longitudinal response are read directly from the simulated data. These values are

$$\omega_S = 470.49 \ MHz$$
$$\omega_P = 473.08 \ MHz$$

Finally, Co is calculated from a complex fit of the wideband frequency response. This C_o value applies for both the longitudinal and width modes. Using Eq. (5.18), we find that the through capacitance is

$$C_o = \frac{1}{j\omega x} = 15.46 \ fF \quad where \ x = 100\left(\frac{1}{10^{S21/20}} - 1\right)$$

Employing these measured parameters, the remaining BVD element values are

$$C = C_o \cdot \left(\left(1 + \frac{\omega_P - \omega_S}{\omega_S}\right)^2 - 1\right) = .1707 \ fF$$

$$L = \frac{1}{\omega_S^2 C} = .6703 \ mH$$

The BVD model parameters are determined in the same way for the width mode of the bar. Table 5.1 gives a summary of the measured and calculated parameters used in the extraction method.

Circuit Parameter	Longitudinal Mode	Width Mode
R (Ω)	1963	1092
ω_s (MHz)	470.49	955.56
ω_p (MHz)	473.08	960.30
C_0 (fF)	15.46	15.46
C (fF)	.1707	.1538
L (mH)	.6703	.1804

Table 5.1: Circuit parameters and measured values from the transfer function of a 10 µm bar.

5.5 Quality Factor Comparison: Mechanical Q vs. Circuit Q

In order to verify the results of the parameter extraction method, a Quality factor comparison is conducted. Several different mechanical Q values are input for the 10x5 µm FEA model, and a simulated S_{21} plot is obtained for each case. Using this S_{21} data, the BVD model parameters for both the longitudinal and width modes are extracted, and the associated circuit Q is calculated according to the procedure described in the Section 5.2. The frequency sweep of the harmonic analysis spans a range of 100 MHz – 1 GHz. The following table summarizes the comparison between the input mechanical Q of the FEA model and the circuit Q extracted from the simulated S_{21} curves.

Q, mechanical	Mode	Q, extracted	% error
500	Length	497.40	0.520
500	Width	496.37	0.726
1000	Length	1009.91	0.991
1000	Width	991.47	0.853
10000	Length	9931.94	0.681
10000	Width	9946.87	0.531

Table 5.2: Comparison of input mechanical Q and extracted circuit Q for a simulated 10x5x0.5 µm piezoelectric resonator - includes percent error calculations.

Based on the information in the table, the extracted Q values match the mechanical Q values to within a percent difference. For the case where Q = 1000, the BVD element parameters are analyzed in a circuit simulator. Fig. 5.7 shows the circuit transfer function overlaid on the simulated S_{21} curve from Fig. 5.6.

S_{21} vs Frequency
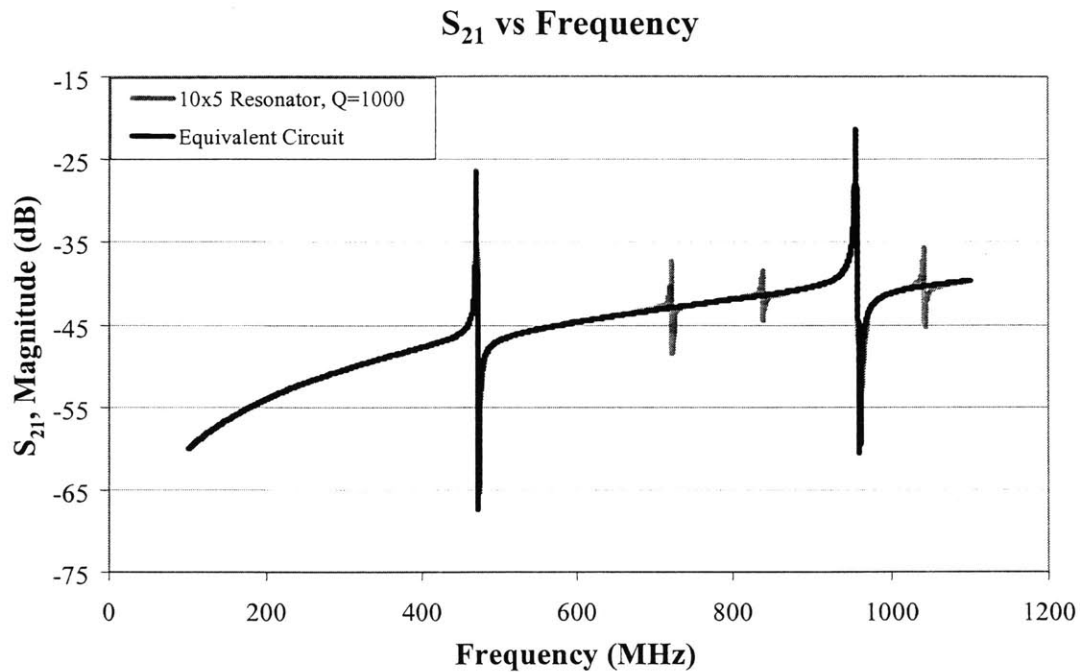
Figure 5.7: Circuit transfer function generated using extracted BVD parameters overlaid on simulated S_{21}. Simulated curve (gray) can only be distinguished from the circuit transfer function (black) by spurious responses of the FEA model.

5.6 Conclusions for Parameter Extraction Method

In the preceding sections, BVD element parameters are extracted from simulated data, which is obtained from a model geometry including no electrical parasitics. When parasitics are significant, as in an actual Draper resonator, the method for determining circuit parameters does not hold well. As a result, a more comprehensive circuit model including parasitics is being developed with the expectation that the latter will be more applicable to geometries of varying sizes and complexities.

Despite the current method's limitations, it still provides significant insight into how the circuit parameters are related to each other when the BVD model applies. For a real device, the relationship between C and C_o is dependent on material properties alone and therefore sets performance limits for the resonator. For longitudinal modes, the maximum value for the ratio of C/C_o is given by

$$\frac{C}{C_o} = \frac{8e_{31}^2}{E\pi^2\varepsilon} = 3.22\% \text{ for AlN} \tag{5.19}$$

Since this ratio has a theoretical limit based on the material properties of AlN, a corresponding restriction is placed upon the impedance and peak separation of the electrical transfer function. Applying (5.19) to (5.13) and rearranging terms to isolate R, we find that for a given resonant frequency and Quality factor, the minimum impedance at ω_s is determined by

$$R_{min} = \frac{1}{\omega_s Q} \frac{1}{C_o(0.0322)} \tag{5.20}$$

Furthermore, the maximum peak separation is calculated according to

$$\sqrt{\frac{C}{C_o} + 1} - 1 = \frac{\omega_p - \omega_s}{\omega_s} = 1.6\% \tag{5.21}$$

These limits can be verified by calculating the R value and peak separation of the analytical transfer function of Ch.2. Substituting the applicable simulation parameters into (5.20) and (5.21), we find that

$$\left.\begin{array}{l} R_{min} = 1840 \ \Omega \\ \\ \dfrac{\omega_p - \omega_s}{\omega_s} = 1.6\% \end{array}\right\} \quad \text{Limits calculated from simulation data}$$

While the peak separation matches the material property based maximum exactly, the minimum R is slightly lower (~ 2%) than the value produced by the FEA simulation. This discrepancy indicates that even the "ideal" geometry contains some loss which prevents it from producing the maximum response at resonance. The C_o used for these calculations is determined analytically from the resonator geometry and scaled by a factor of 1.1 to account for the effect of fringing fields. Furthermore, from (5.20), we observe that the through capacitance and the resonant frequency are the only real control variables for R. The two values are inversely proportional – as resonator size increases, C_o increases, while ω_s decreases. The increase in C_o occurs more rapidly than the corresponding decrease in resonant frequency, and as a result, in the current design, larger devices will be able to achieve lower impedances at resonance.

[THIS PAGE INTENTIONALLY LEFT BLANK]

Chapter 6

Coupled Resonator Geometry: Single and Multi-Port Configurations

6.1 Introduction

Thus far, it has been demonstrated that the current design for Draper's L-Bar resonator, while not completely optimized, is applicable in the MEMS community and specifically, in the area of wireless communications. However, initial studies of the resonators indicate that a considerable amount of improvement is still needed in the overall design. As a result, a new topology, initially presented in the qualitative analysis, will not only improve upon the performance characteristics of the current device but also create new opportunities in filter design at Draper. The new geometry couples two longitudinal bars through a common tether to create a new device. Although the electromechanical behavior of the coupled bar is similar to that of a single bar, the new device possesses unique characteristics that make it a more advantageous design. This coupled configuration has the capability to serve a variety of functions depending upon the electrical boundary conditions that are imposed upon it. Because the L-Bar resonator is an electrical device represented as a combination of passive elements (i.e. BVD equivalent circuit model), individual resonator bars can be coupled in various single and multi-port configurations. Figure 6.1 shows the new coupled design, with its key features highlighted.

Resonator Dimensions:
L = 6 μm
w = 3 μm
t = 0.5 μm

Tether Lengths:
Outside = 7 μm
Inside = 14 μm

Coupling ("Inside") Tether

Boundary Conditions:
y-DOF constrained at tether ends
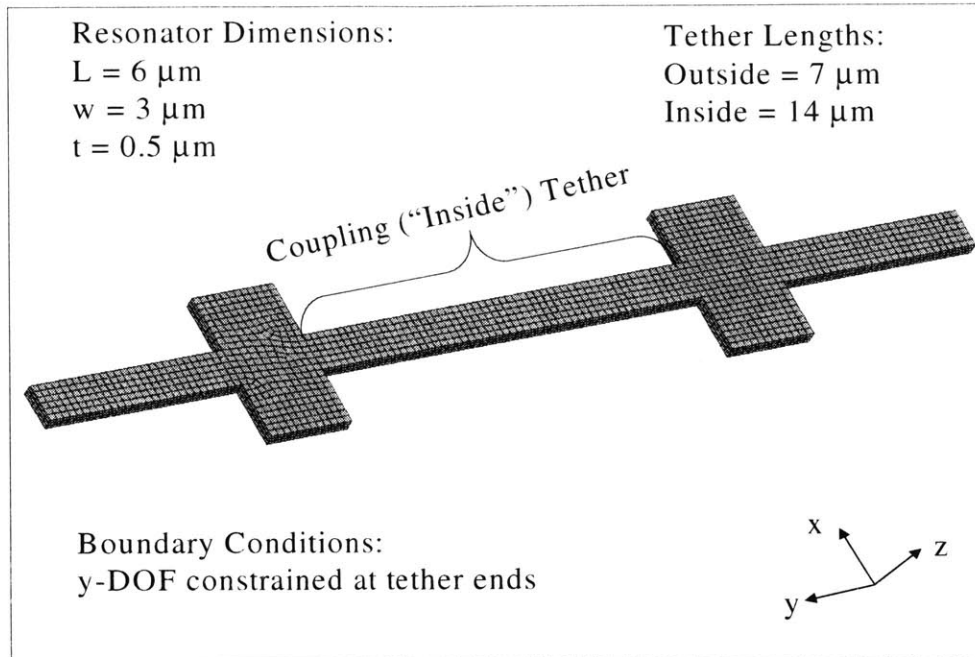
Figure 6.1: Coupled resonator geometry. "Infinite" displacement boundary conditions imposed upon tether ends. Electrical boundary conditions are determined by filter configuration.

The model in Fig. 6.1 represents a "symmetric" coupled geometry, where the inside tether length is twice the outside. The qualitative analysis demonstrated that this configuration would produce the cleanest in-phase mode and therefore, in theory, the most desirable electrical transfer function. Theoretical knowledge of modal analyses suggests that the resonant frequencies associated with the in-phase and out-of-phase modes will fall symmetrically about the longitudinal center frequency of a single bar. However, FEA simulations of the coupled bar show that the in-phase modal frequency coincides closely with the single bar's natural frequency, and the out-of-phase mode falls either above or below this value.

6.2 Comparison of Single Port Configurations

Two straightforward single port topologies are the parallel and series configurations. Normally, in relation to filter technology, the goal is to design a device whose impedance is as low as possible at the operational resonant frequency. Consequently, boundary conditions which prescribe a parallel electrical configuration are most useful in frequency filter design. Regardless

of applicability, however, investigating the responses of parallel and series coupled configurations as they compare to that of a single bar, provides insight into how the coupled piezoelectric resonator behaves as an electrical device. Figures 6.2(a) and (b) illustrate how the electrical boundary conditions of the model are applied in defining the two single port configurations.
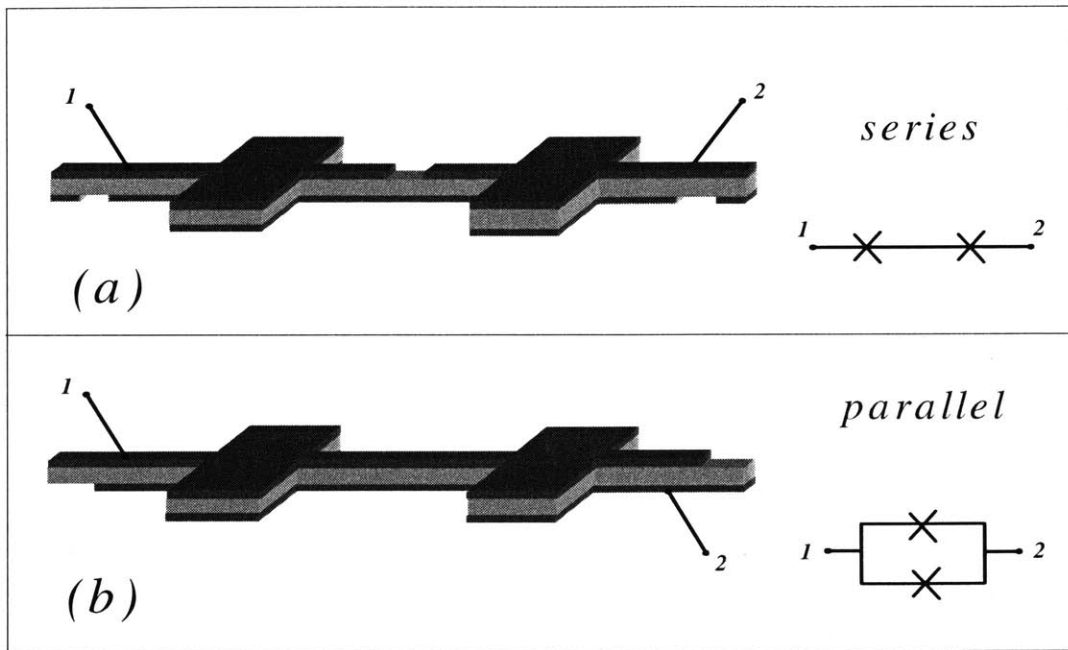
Figure 6.2(a) and (b): Single port electrical configurations of coupled resonator design. Gaps in electrode represent cuts made in the metal to create the boundary conditions.

As indicated by the figure above, the electrical configuration is determined by the placement of the electrodes on the top and bottom surfaces of the resonator. The equivalent circuits to the right of each geometry show the path current is allowed to travel from the input at terminal 1 to the output at 2. From knowledge of basic circuits, the parallel configuration is expected to yield a transfer function two times lower in magnitude than that obtained from a single bar, assuming the coupled bars have the same impedance characteristics. Conversely, the series topology should produce an impedance whose magnitude is double that of a single model. The following is a set of plots comparing the output of the parallel and series configurations. The impedance characteristic of each topology is overlaid on the electrical transfer function of a single bar to demonstrate their significance.

Impedance vs. Frequency
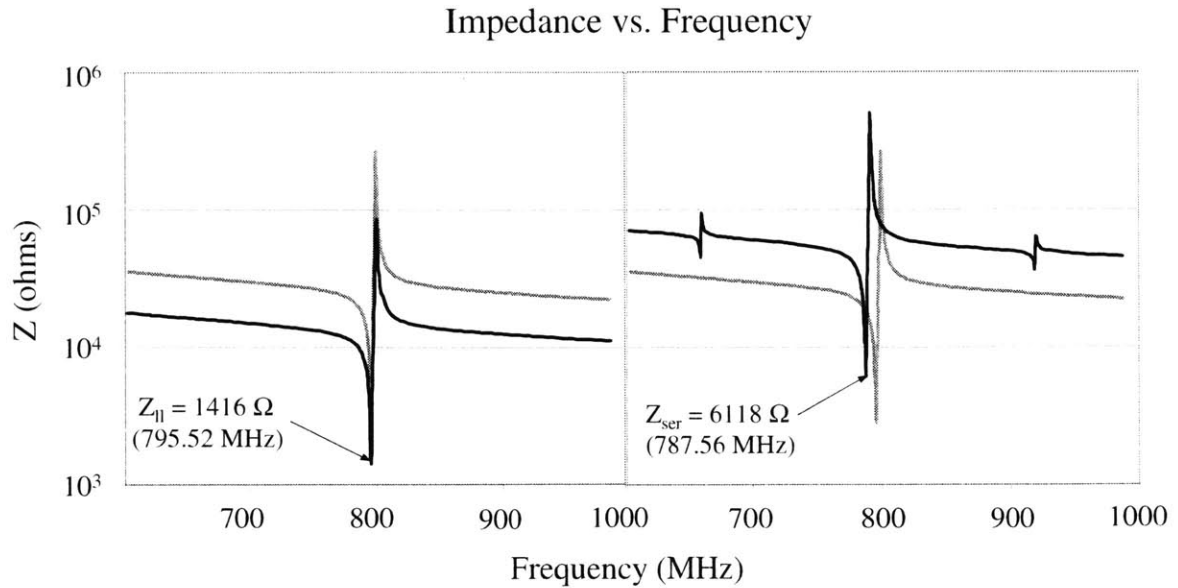
Figure 6.3: Electrical transfer functions for the coupled parallel and series configurations. Plot on the left shows parallel response while the graph on the right illustrates series curve.

For a coupled resonator design, there are two primary longitudinal modes – in-phase and out-of-phase. By virtue of the electrode configurations used to create a parallel or series resonator circuit, only one of the two longitudinal modes will produce a net electrical output for a given configuration. For the parallel design, the operational frequency corresponds to that of the in-phase mode, whereas, the series configuration produces an amplified response when the displacement of the bars is out of phase. This knowledge helps explain the frequency shift of the resonant response for the series transfer function shown in the plot on the right of the figure. The center frequency of the in-phase mode coincides almost exactly with ω_s of the single bar, while the out of phase modal frequency is slightly lower than the latter. Furthermore, in contrast to theory, the Z_{min} value for the series design is more than twice the single bar output. This result occurs because the out-of-phase mode shape is characterized by a "polluted" longitudinal motion relative to the "clean" mode shape of a single bar (i.e. qualitative analysis – Fig. 1.5). Therefore, the electrodes are not coupled perfectly by the out-of-phase mode, and the impedance of the device increases slightly above the theoretical value of $2 \cdot Z(\omega_s)_{single}$. On the other hand, because the resonance of the parallel configuration occurs at the in-phase mode, the symmetry of the latter produces a much cleaner longitudinal mode shape. This clean longitudinal motion, in turn, produces a resonant impedance value that matches the theoretical standard of $\frac{1}{2} \cdot Z(\omega_s)_{single}$.

6.3 Parallel Configuration

As discussed earlier, the series configuration applied to a coupled resonator has little applicability in regards to frequency filter design. Consequently, with respect to single port coupled topologies, we restrict our focus to the modeling of the parallel configuration. As evidenced by Fig. 6.3 and test results from [6], the impedance transfer function of the coupled parallel configuration corresponds closely to that of its single counterpart. Although the parallel resonator circuit possesses an additional longitudinal mode shape (i.e. out-of-phase), its impedance characteristic is virtually identical to that of a single bar, excluding a factor of two between their magnitudes. Therefore, the parallel topology represents a way to achieve the wideband frequency response of a single bar with a reduction in impedance at resonance. This improvement upon the performance of the single bar is highly advantageous and makes the parallel coupled configuration a viable option for future resonator design.

6.3.1 Effect of Coupled Tether Length Variations on Impedance

The geometry shown in Fig. 6.1 is chosen based on a symmetry condition. In other words, the initial topology for the coupled resonator is analogous to placing two single resonators side by side. To create the coupled design, the "inside" tethers are joined to each other. The length of this common tether affects the amount of coupling between the resonator bars. As Fig. 6.3 indicates, when the coupled configuration is symmetric (i.e. inside tether length is twice outside lengths), the characteristics of its transfer function, such as bandwidth and center frequency, match those of a single bar. However, if the length of the coupling tether is modified, the impedance characteristics of the model change as well. As a result, a study of the influence of inside tether length on the device impedance is undertaken. If modifications yield appreciable changes in the transfer functions, the coupling tether length can then be utilized as an additional tunable parameter in the filter design process. The lengths of the coupling tether used in the case study are chosen so as to coincide with multiples of 7 μm, the outside tether length. The values chosen were 3.5, 7, 14 and 21 μm, which correspond approximately to increments of the longitudinal wavelength of the 6 μm bar (i.e. 3.5 μm ~ ¼λ, 7 μm ~ ½λ, etc). Figure 6.4 shows the simulated transfer functions corresponding to the various geometric topologies.
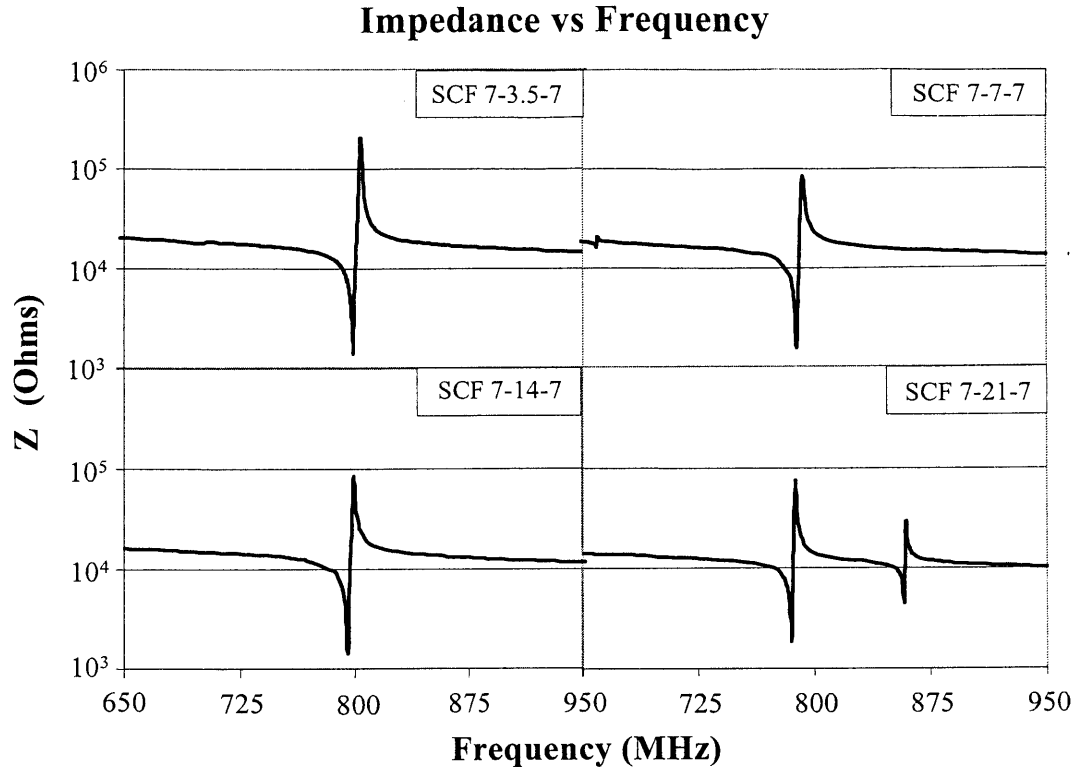
Figure 6.4: Parallel impedance characteristics for different coupling tether lengths. Legend notation (i.e. 7-4-7) indicates lengths of the inside and outside tethers according to the form outside-inside-outside (values in μm)

The different geometries produce comparable resonant impedances and center frequencies at their primary longitudinal modes. The center frequencies are, for the most part, within a percent difference of each other. The largest discrepancy between the resonant impedances is only about 500 Ω, a relatively small difference considering average off-resonance impedances of 10 kΩ or greater. Therefore, based on the simulation results, the primary longitudinal response of the parallel coupled resonator seems to be relatively insensitive to changes in coupling tether length. However, spurious responses, which result from longitudinal modes dominated by tether motion, do appear to be highly dependent upon the amount of mechanical coupling that exists between the resonators. All the geometries, with the exception of the symmetric case, possess at least one spurious mode. The magnitude of the spurious mode's electrical response and its center frequency vary significantly as inside tether length changes. Only coupling tether lengths corresponding to a half wavelength or less produce negligible spurious modes, with relatively small magnitudes and locations far from the center frequency of the primary longitudinal mode.

As the inside tether length increases above 7 μm, longitudinal waves traveling through the tether produce significant motion in the resonator, resulting in an electrical response at a frequency other than the primary resonant mode. Table 6.1 illustrates this phenomenon by comparing the frequency and impedance values of the different geometries.

Illustration and BCs (Parallel Configuration)	Coupling Tether Length, μm ($L_{outside} = 7μm$)	Longitudinal Mode, Ohms - (ω_s, MHz)	Spurious Mode, Ohms - (ω_s, MHz)
	3.5	1391.1 (797.7)	N/A (520.4)
	5	1456.7 (795.7)	17877 (682.9)
	7	1581.4 (789.0)	16426 (659.1)
	11	3059.4 (777.2)	2368.5 (830.2)
	14	1416.2 (795.2)	N/A
	17	1517.7 (790.9)	6144.0 (997.2)
	21	1878.9 (785.5)	4440.2 (857.9)
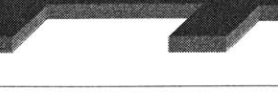
Table 6.1: Magnitude and frequency values for various coupling tether lengths. Mechanical Q of 1000 input for simulations of parallel configurations. "N/A" indicates a negligible value.

For the three coupling tether lengths of 7 μm or less, the impedance value of the spurious mode is over an order of magnitude larger than that of the corresponding longitudinal mode. Furthermore, the spurious frequency is shifted more than 100 MHz from the longitudinal center

frequency. Neglecting the symmetric geometry, models with coupling tether lengths greater than a half wavelength possess significant spurious contributions. In fact, for a tether length of 11 μm, the spurious impedance is about 20% lower than the primary response. In general, for longer inside tether lengths, spurious modes resulting from large vibrations in the tether cause electrical responses comparable in magnitude and frequency to the primary longitudinal mode of the device.

6.3.2 Effects of Tolerance Error: Mechanically Coupled vs. Uncoupled

To this point, we have assumed the lengths of the coupled resonators to be equal. This assumption requires their longitudinal resonant frequencies to be equal as well. However, as discussed briefly in the qualitative section, with respect to current fabrication techniques, making two identically dimensioned resonators is virtually impossible. Therefore, it is important to investigate how tolerance errors affect the electrical response of the parallel configuration for both a coupled and uncoupled bar. During fabrication, photolithography is used to define the resonator geometry. A chemical etch is then employed to release the resonator from the substrate. Finally, detailed modifications of the geometry can be made by means of laser trimming. While this fabrication process is considerably accurate, the tolerance of the existing process is only accurate to about a tenth of a micron. In an absolute sense, this tolerance value is adequate, but, as demonstrated in the qualitative analysis, even a resonator length discrepancy as small as .1 μm shifts the center frequency of the device by more than a percent. In relation to high Q resonators which are mechanically uncoupled, a percent difference between the resonant frequencies of the two bars creates two distinct response peaks and negates the benefit of using the parallel configuration. As shown in [6], a coupled resonator bar forces the bars' resonant frequencies to match and thus, offers a more robust design. Figures 6.5(a) and (b) show the electromechanical topologies of a coupled and uncoupled parallel resonator.
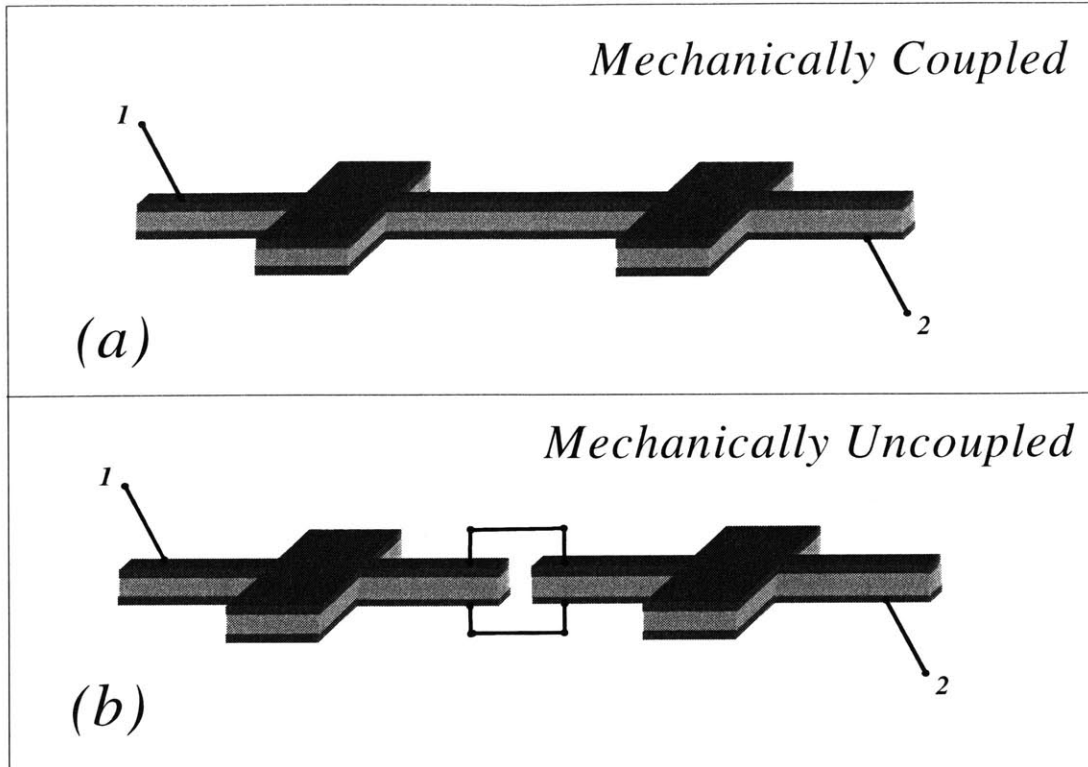
Figure 6.5: (a) Coupled parallel configuration (b) Uncoupled parallel configuration

As the figure above shows, the resonators are coupled electrically in both configurations. The distinction between coupling occurs in the mechanical domain depending on whether the inside tethers are physically joined. If the resonators are identical in size, both configurations produce the same transfer function when driven at the longitudinal resonant frequency. However, if fabrication errors result in a small discrepancy between the lengths of the bars, the impedance characteristics associated with the two configurations will no longer match. For the coupled geometry, a small difference between the bar lengths causes the in-phase and out-of-phase mode shapes to degrade slightly, affecting their electrical outputs. In the ideal case, with no discrepancy in length, the in-phase mode couples the electrodes perfectly, and the out-of-phase response is completely cancelled. However, with a discrepancy in lengths, the response of the in-phase mode decreases, while incomplete cancellation of the out-of-phase mode causes a small impedance drop. On the other hand, having neither an in-phase or out-of- phase mode, the resonators of the uncoupled case behave like two separate bars, with two distinct resonant frequencies. Consequently, fabrication error causes the uncoupled transfer function to break down, and the amplified responses the two bars no longer combine at a single frequency. Figure

6.6 compares the changes in electrical transfer function due to tolerance errors for a mechanically coupled and uncoupled parallel resonator configuration.

Impedance vs Frequency
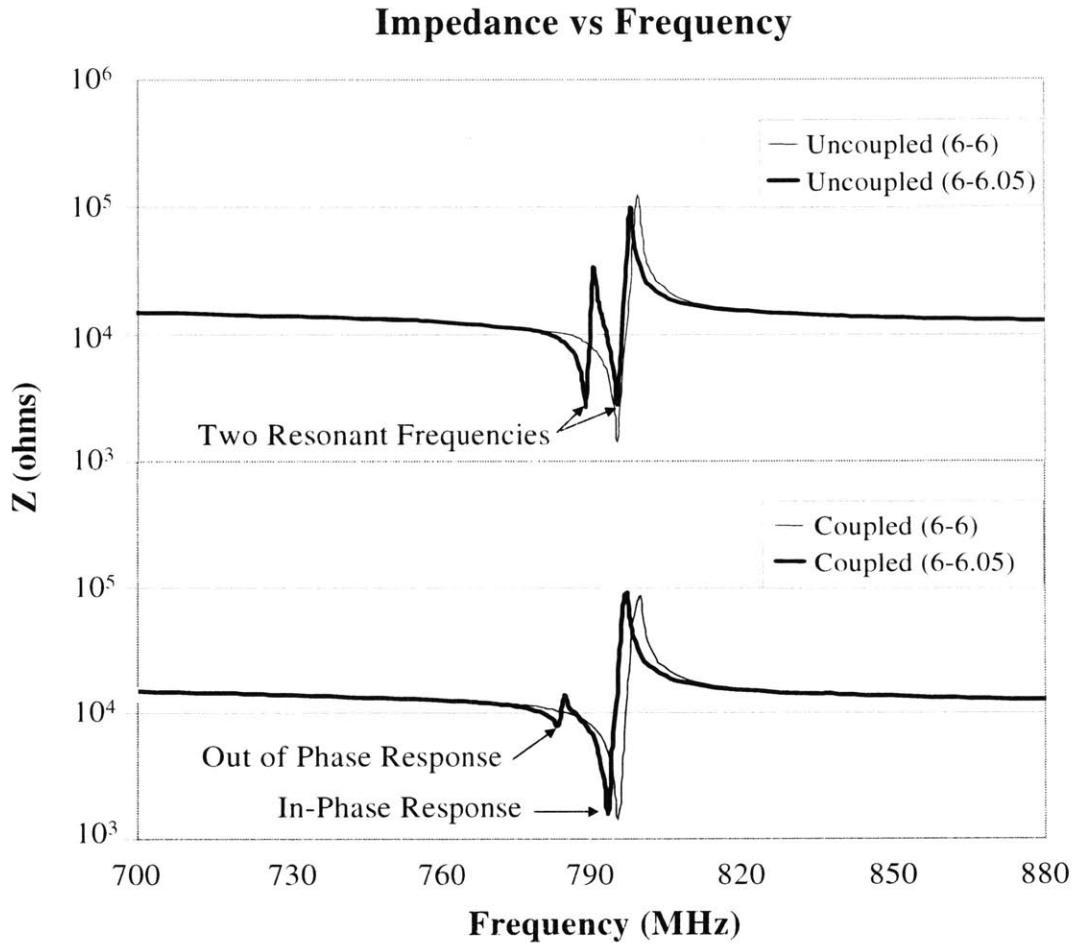
Figure 6.6: Coupled and uncoupled transfer functions showing effect of fabrication errors.

The two distinct impedance dips of the uncoupled geometry are shown in the first graph, while the in-phase and out-of-phase responses of the coupled design are marked on the lower graph. For the coupled bar, slight pollution of the in-phase mode shape causes a small increase in impedance as compared to the ideal geometry. Likewise, a break down in the out of phase mode shape corresponds to an imperfect cancellation of charge and a spurious electrical response. When analyzing the plots above, it is important to note that these transfer functions are produced by a dimensional mismatch that is half (i.e. 50 nm) the quoted tolerance value of .1 μm. Therefore, a more realistic error value would cause even greater degradation of the impedance characteristics. Specifically, in relation to the uncoupled case, a larger fabrication error would

produce an even greater frequency gap between the two longitudinal responses. Their magnitudes would not suffer significantly however, because, despite the discrepancy in lengths, the longitudinal mode shape of each resonator would still be clean. On the other hand, in the coupled design, as the difference between resonator lengths becomes more severe, the two primary longitudinal mode shapes will continue to degrade, resulting in a further break down of the transfer function. This break down is illustrated in the figure below.

Impedance vs Frequency
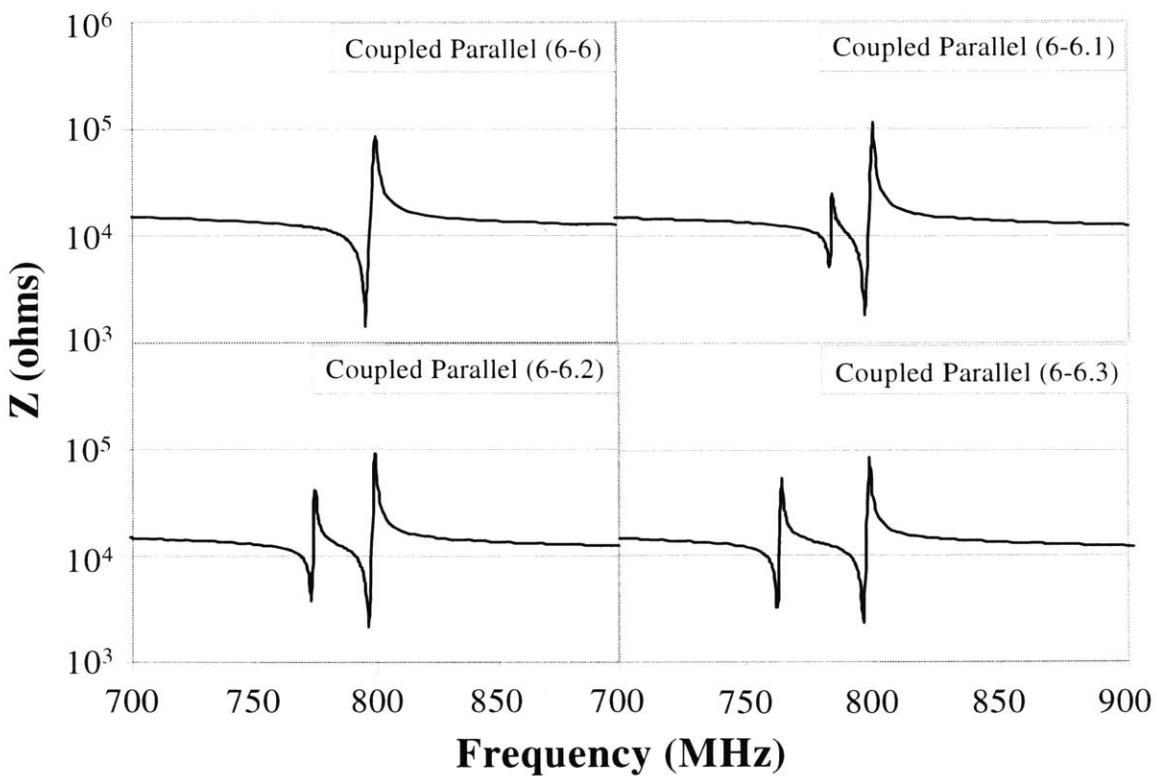
Figure 6.7: Deterioration of coupled transfer function as fabrication error increases (i.e. discrepancy between resonator lengths increases). The first value in the parentheses refers to the unmodified bar, 6 µm in length. The second indicates the amount of mismatch between the bars.

When the fabrication mismatch reaches .2-.3 µm, the transfer function of the coupled geometry resembles that of the uncoupled case, where the in-phase and out-of-phase modes represent two distinct resonant frequencies with comparable responses. A similar result was found for the effect of resonant frequency mismatch on the corner-coupled resonators of [6]. However, in the

latter, the combined electrical output of the flexural-mode microresonators was dramatically compromised with a much smaller mismatch than the values shown in Fig. 6.7.

Current fabrication techniques employed at Draper consistently produce dimensional tolerances of .1 μm or less. Therefore, assuming errors will not exceed this standard, the coupled parallel resonator represents a much more robust design than its uncoupled counterpart, whose transfer function is degraded severely with even the smallest of dimensional discrepancies.

6.4 Multi-Port Configuration: Ladder Filter

Because the parallel coupled resonator is a one-port electrical device, it can function only as filter component. However, by changing the electrical boundary conditions imposed upon the coupled geometry, the latter can be transformed into a multi-port device, allowing it to operate as a filter independent of additional passive elements. Because the electrical boundary conditions depend only on the positions of the electrodes, the geometries of the single and multi-port configurations are the same. The difference between the two configurations lies in the method used to actuate and sense the behavior of the resonator bars. In the parallel configuration, both the bars in the coupled set are driven simultaneously and their output represents a combination of their responses. In contrast, for a multi-port configuration, only one resonator is driven by a sinusoidal potential input. Because the resonator has piezoelectric properties, this voltage input produces a sinusoidal displacement in the driven resonator. Mechanical coupling between the bars, in turn, causes a corresponding vibration in the unforced resonator. The vibration of the latter induces an output voltage which determines the filter response.

The ladder filter is a common multi-port topology, with well established applications in the area of wireless communications [12]. A normal ladder filter design includes two resonators whose electrical responses are linked by a passive capacitor element. This capacitive element provides electrical coupling between the resonators and creates a filter which can operate with or without a mechanical connection. In fact, most current ladder filter designs are fabricated such that the resonators are not physically joined. However, as with the parallel configuration, mechanical

coupling yields a ladder filter design that is more robust to tolerance errors. Figure 6.8 shows both the coupled and uncoupled ladder filter geometries as well as the corresponding equivalent circuit. Source and load resistances are added to the geometries shown in Figures 6.5(a) and (b) in order to model the presence of the electrical probes used to actuate and sense the filter's response. The output voltage is determined by finding the potential drop across the load resistor. The electrical reflection coefficient, S_{21}, is calculated from this value and utilized to generate the transfer function of the filter.
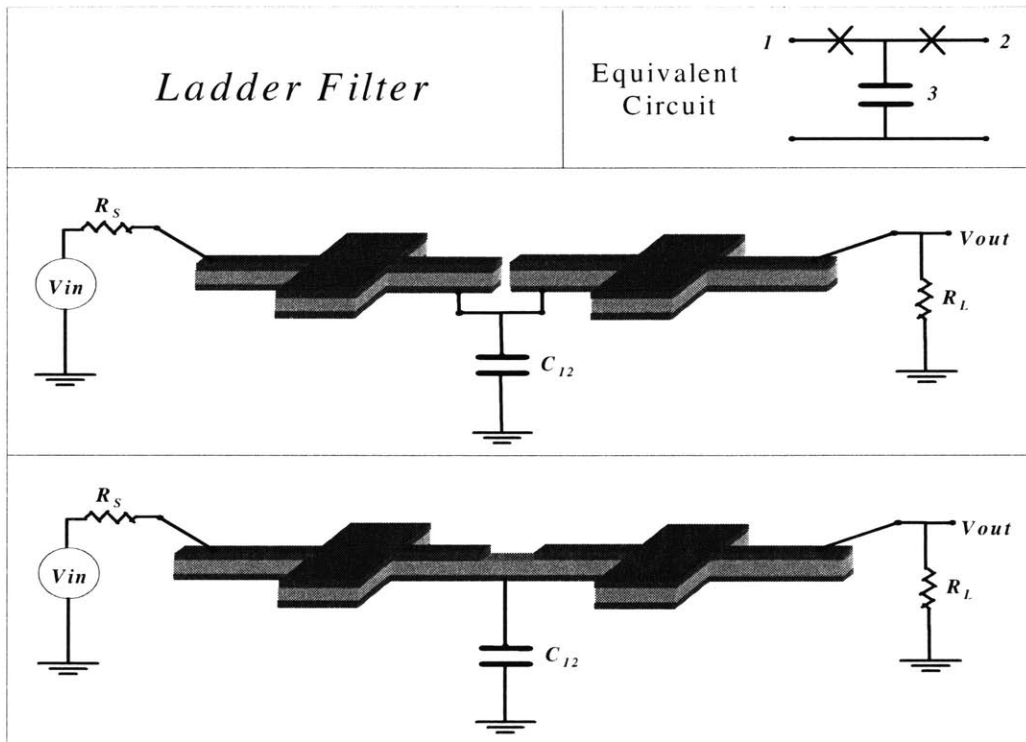
Figure 6.8: Coupled and uncoupled ladder filter topologies including equivalent circuit model. Passive elements include coupling capacitor, C_{12}, as well as source and load resistances (i.e. R_S and R_L). Filter output is read across R_L.

The passive coupling capacitor is connected to the bottom electrodes of both resonator pairs. As the equivalent circuit indicates, the resonators share a common node in the electrical domain. In the coupled geometry, this common node is created by both the mechanical connection between the inside tethers and the presence of C_{12}. For the uncoupled configuration, the coupling capacitor alone is responsible for linking the electrical responses of the resonator pair. For the uncoupled topology, the C_{12} element provides filter designers with a tunable parameter that can

control the filter response in the passband [2]. At or near the operational resonant frequency of a high Q filter, the impedance characteristic of the coupling capacitor dominates the electrical transfer function of the uncoupled filter. For typical MEMS filters, the bandwidth is relatively small compared to the center frequency. As a result, the coupling capacitor impedance is virtually constant over the operational frequency range, providing a relatively flat passband response. As will be demonstrated later, the passband response for a coupled filter is dominated by the mechanical connection between its tethers rather than the value of C_{12}.

Similar to the response of the parallel configuration, the filter output of the uncoupled ladder topology will break-down if the resonator sizes do not match exactly. Once again, however, if the resonators are coupled mechanically, the transfer function of the filter is significantly more robust to dimensional errors. To demonstrate this phenomenon, a case study is performed utilizing the guidelines provided by an optimized ladder filter design, the details of which are included in the thesis of J. Kang [2]. While the design in [2] was fully defined for only one specific resonator ($L = 6.04$ μm, $w = 3.22$ μm, $Q = 10^4$), the general optimization approach suggests that filter parameters based on a generic resonator bar should have the following relationships:

$$\left. \begin{array}{l} R_S = R_L = 2R \\ C_{12} = 500C \end{array} \right\} \textit{ Uncoupled Ladder Filter Design}$$

where R is the resistance and C is the motional capacitance of the BVD model. When the mechanical coupling is included, an optimal transfer function is achieved with a different set of filter parameters:

$$\left. \begin{array}{l} R_S = R_L = 10R \\ C_{12} = 1000C \end{array} \right\} \textit{ Coupled Ladder Filter Design}$$

With both the coupled and uncoupled configurations close to their optimum designs, Figure 6.9 compares their electrical responses.

S$_{21}$ vs Frequency
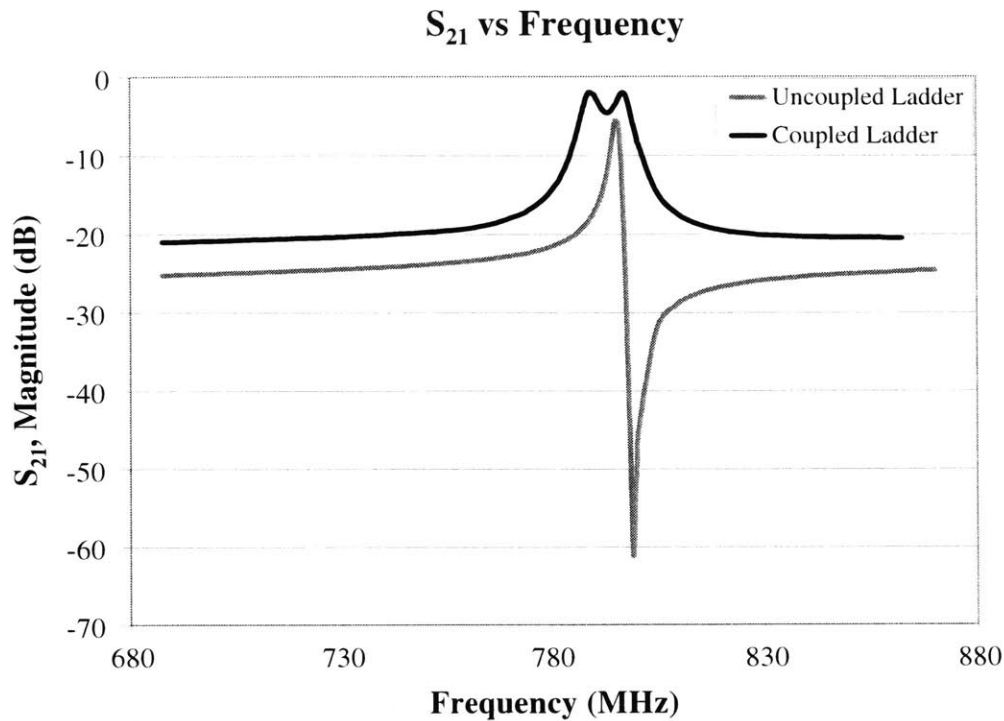
Figure 6.9: Electrical transfer functions for coupled and uncoupled configurations using circuit parameter guidelines from an optimized design.

The effect of mechanical coupling on the transfer function of the ladder filter is evident from the S$_{21}$ plot above. The two peaks of the coupled response correspond to the in-phase and out-of-phase modes of the device. While the values of the passive electrical elements are refined to achieve minimal insertion loss, the passband "ripple" between the peaks indicates that further mechanical optimization is needed to flatten the response over this frequency range.

Assuming that this ripple can be attenuated, the coupled filter offers the potential for a much larger response bandwidth than the value that is achievable using the uncoupled configuration. The uncoupled bandwidth, like that of a single bar, depends primarily on the Q of the device. In contrast, the bandwidth of the coupled filter is determined mechanically by the modal output of the structure [13].

113

Despite the advantages discussed thus far, the importance of coupling becomes most apparent when the effects of fabrication errors are investigated. When tolerance errors are incorporated into the geometry of a ladder filter model, the effects of such non-idealities are similar to those associated with the parallel configuration. For example, in the uncoupled case, the single resonance occurring at the resonators' common longitudinal frequency begins to break-down into two distinct, smaller electrical responses. On the other hand, the transfer function of the coupled geometry is only slightly degraded. Figure 6.10 illustrates this difference in robustness.

S$_{21}$ vs Frequency
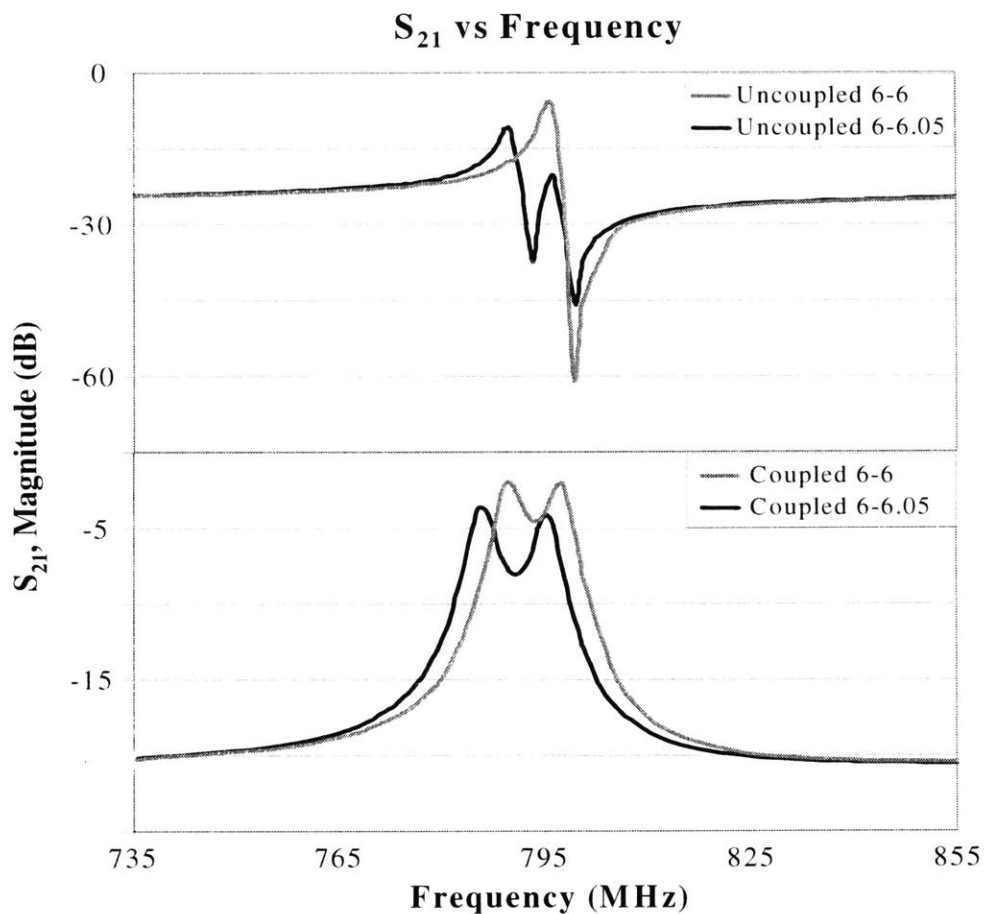
Figure 6.10: The effect of fabrication errors on the transfer functions of coupled and uncoupled ladder filters. The legend notation, "6-6.05", refers to the different resonator lengths (μm).

For a relatively small discrepancy in resonator length, the uncoupled ladder geometry produces a significantly deteriorated transfer function. Because the fabrication error of .05 μm is still rather small compared to the resonator lengths, the difference between the center frequencies is also small. For this reason, the unforced bar has an electrical response at both resonant frequencies.

As the difference in resonator length increases, the individual responses in the transfer function would be expected to drift farther apart and decrease further in magnitude. In contrast, the lower plot illustrates the robustness of the coupled design. For the same fabrication error as in the uncoupled case, the response at resonance drops slightly and the passband ripples increases. However, the transfer function, in general, does not break down significantly.

While the presence of the coupling capacitor is necessary in the uncoupled design, the effect of C_{12} is still not clearly established for the coupled geometry. Since the advantages of the latter are now firmly established, there is interest in investigating the role of the coupling capacitor in the mechanically coupled ladder filter design. For this case study, we return to the more realistic circuit parameters of Ch. 5, where R_S and R_L equal 50 Ω. Assuming identical bar dimensions, the coupling capacitor value is varied to match multiples of a single bar's through capacitance, C_o. Figure 6.11 shows how the S_{21} transfer function of the coupled ladder filter is affected by changes in the value of C_{12}.
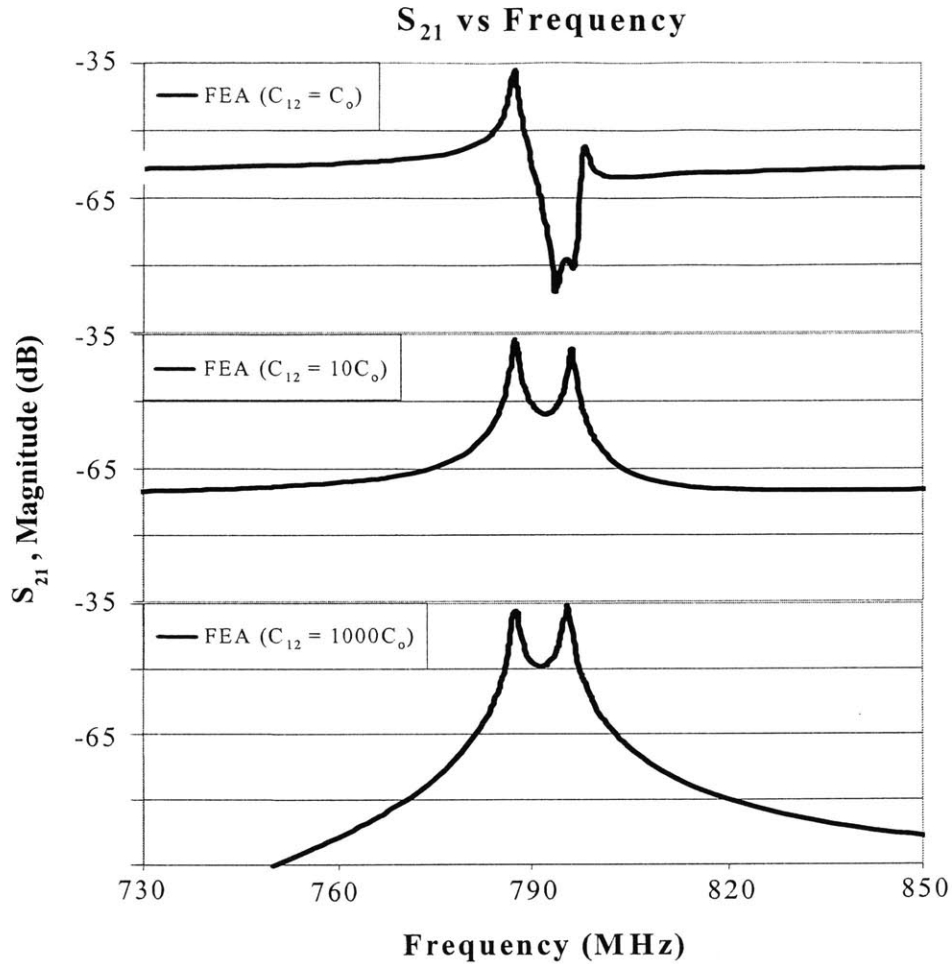
Figure 6.11: Changes in transfer function of coupled ladder filter with variation in C_{12}. "FEA Ladder" response curves generated from simulation data of coupled topology shown in Fig. 6.8. "Circuit Ladder" represents response of circuit model in which BVD parameters have been replaced by a passive capacitor having a value of C_o.

The figure above indicates that the coupling capacitor value in the mechanically coupled ladder design has a significant effect on the transfer function of the latter. However, the general trend is that the filter response becomes increasingly better as the value of C_{12} is made larger. This trend indicates that the coupled ladder design performs best when the mechanical coupling through the support tethers dominates the impedance characteristic. Therefore, whereas C_{12} is necessary for operation of the uncoupled ladder filter, its presence in the coupled design is not only unnecessary, but degrades the transfer function significantly when the C_{12} value is within an order of magnitude of C_o.

6.5 Multi-Port Configuration: Stacked Crystal Filter

The general conclusion from the ladder filter case study is that large coupling capacitor values produce the best transfer function characteristics. In the electrical domain, large capacitors have low impedances. When C_{12} is equal to $1000C_o$, the impedance of the coupling capacitor ($Z \propto 1/C_o$) is relatively small and, therefore, has little effect on the transfer function of the model. As a result, for large coupling capacitor values, the effect of C_{12} in the circuit model can be neglected. If the impedance of the coupling capacitor is assumed to be negligible, the equivalent circuit for the ladder filter matches that of another multi-port topology - namely, the stacked crystal filter (SCF). Originally, SCF designs were characterized by vertically stacked layers of piezoelectric material and focused on isolating the primary thickness modes of the structure [11]. In a SCF design, the top layer is driven at the resonant frequency and because the two layers are joined mechanically, the bottom layer resonates as well. In between the layers, the common electrode is grounded, thus completely decoupling the layers in the electrical domain. Because the layers are not coupled electrically, the output voltage is attributed solely to the mechanical resonance of the bottom layer. Like the original SCF, the electrodes of Draper's coupled resonator design are lithographically cut such that the two bars are driven and sensed independently, while, at the same time, sharing a common ground electrode. Figure 6.12 shows the two geometric configurations characterizing the SCF topology.
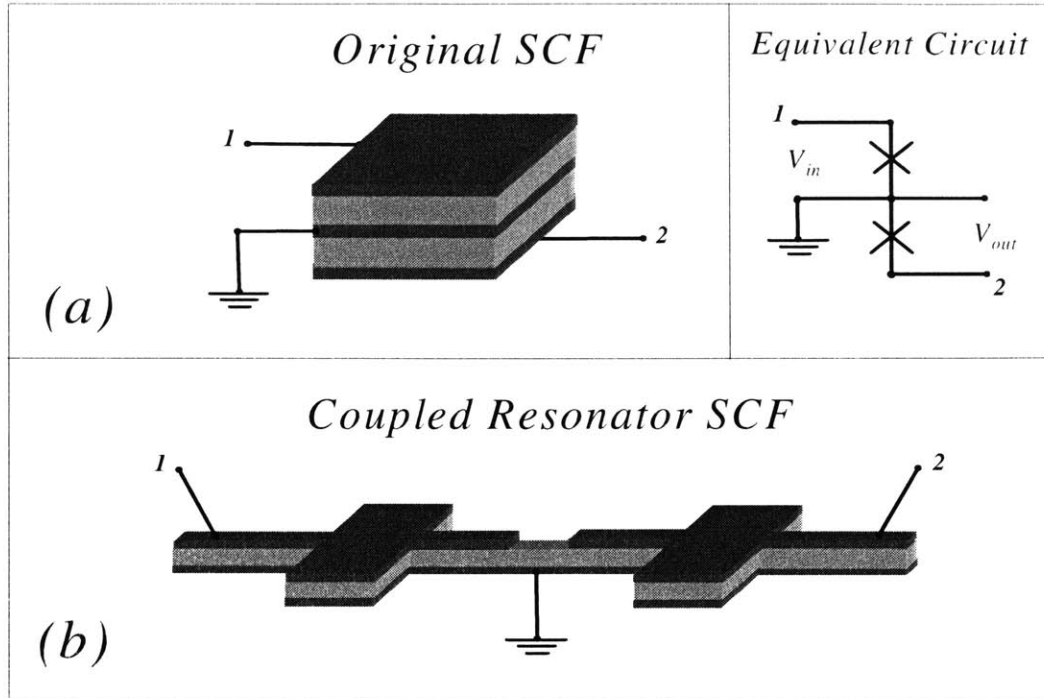
Figure 6.12(a) and (b): Geometric configurations for original and coupled bar stacked crystal filter. The equivalent circuit for the SCF topology is also shown.

The equivalent circuit indicates that the bars will not interact with each other electrically without mechanical coupling. As in a ladder configuration, both the longitudinal modes of the SCF geometry produce a voltage response at their resonant frequencies. For a typical SCF geometry, the in-phase and out-of-phase responses overlap in the transfer function creating a new larger passband. The frequency separation between the in-phase and out-of-phase modes depends upon the modal output of the structure and, as a result, varies with modifications to the geometry. Consequently, as with the parallel configuration, there is interest in observing how varying the inside tether length (i.e. affecting the coupling between the resonators) changes the filter characteristics of the coupled SCF geometry.

6.5.1 Effect of Coupled Tether Length Variations on S_{21}

An ideal filter has a large bandwidth (i.e. 3-5% of center frequency), flat passband, and sharp roll off characteristics. A set of relatively optimized circuit parameter values was introduced in the ladder filter case study. However, the optimized source and load resistances are currently not realizable values. Therefore, R_S and R_L are maintained at 50 Ω and simulations are performed to

determine how modifications to the coupling tether length can be utilized to tune filter parameters. The simulated FEA model employed to generate the transfer functions of the various coupled configurations is shown in Figure 6.13.
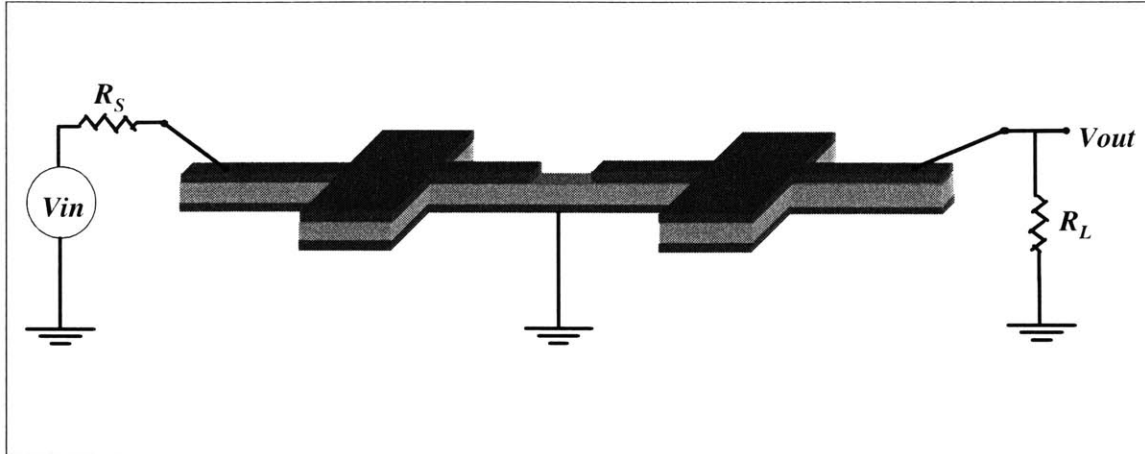
Figure 6.13: FEA model of coupled SCF configuration including source and load resistances. Output voltage is read across R_L.

As in the previous tether length study, the outside tether length of 7 μm is held constant, and the coupling tether length is varied to match multiples of the outside value (i.e. 3.5, 7, 14 μm, etc). Because the multiples approximately coincide with fractions of the bar's longitudinal wavelength, the different configurations produce relatively similar transfer function parameters. Figure 6.14 illustrates the similarities between the various response curves.

S_{21} vs Frequency
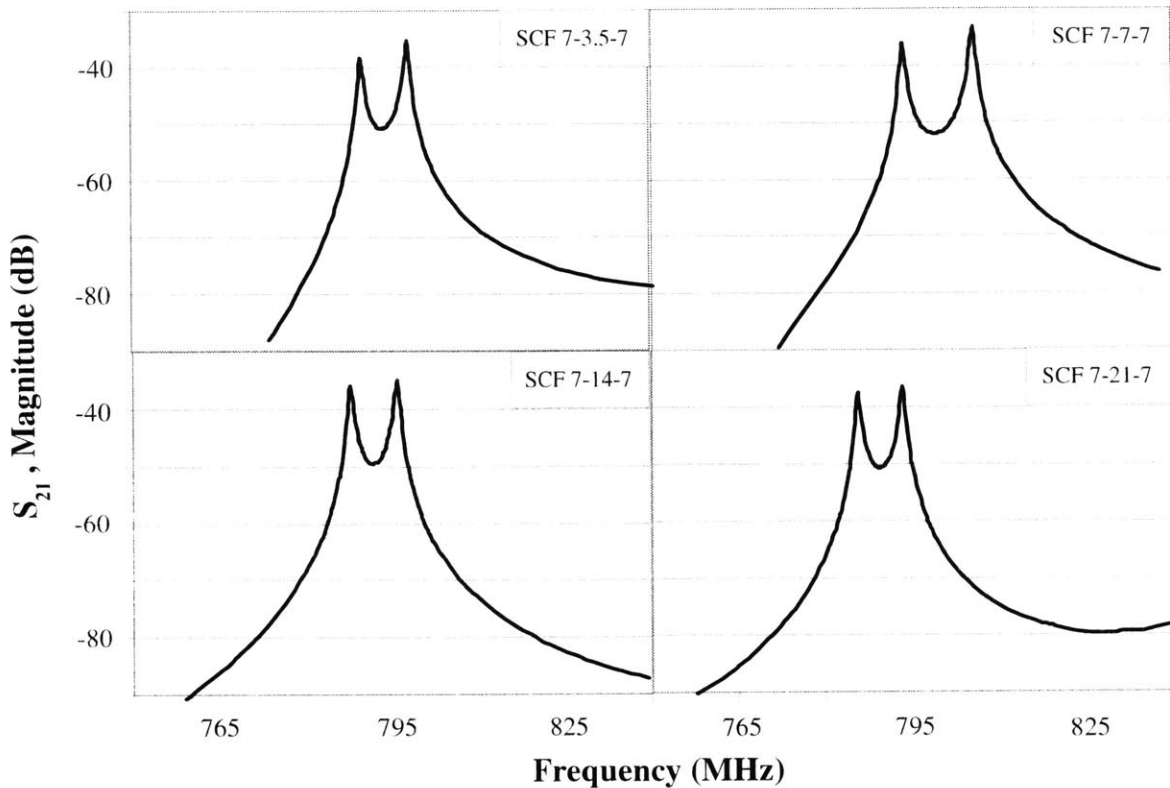
Figure 6.14: SCF transfer functions for various coupling tether lengths. The legend notation is the same as that used for Fig. 6.4.

For all the configurations, the out-of-phase response peak (between -33 and -35 dB) is slightly higher than the in-phase value. The peak to peak difference for the symmetric geometry is the smallest (< 1 dB) of the group. However, none of the other configurations produce a peak discrepancy larger than 3 dB. Since the models are not optimized, their passbands response is significantly distorted. For all the geometries, the "ripple" through the passband is in the range of 12-16 dB. Finally, the roll off for each curve is consistent with that of a typical filter. On average, the passband rejection is approximately 40 dB. Table 6.2 summarizes the comparison of the transfer function parameters.

Coupling Tether Length (μm)	Bandwidth (MHz)	Passband Ripple (dB)
3.5	8.00	11.89
7.0	12.14	15.85
14.0	7.98	13.25
21.0	7.63	12.98

Table 6.2: Transfer function parameters for SCF geometries with modified inside tether lengths.

For coupling tether lengths which do not coincide with multiples of the outside length, the transfer function parameters vary significantly from the values shown above. Especially in the cases of smaller inside tether lengths, the transfer function parameters are sensitive to changes in the geometry. With a change as little as a micron in the coupling tether length, the passband ripple and peak to peak bandwidth vary considerably. Furthermore, the location and significance of spurious modes is also affected. Fig. 6.15 shows the effect of a transition in coupling tether length from 7 to 6 μm.
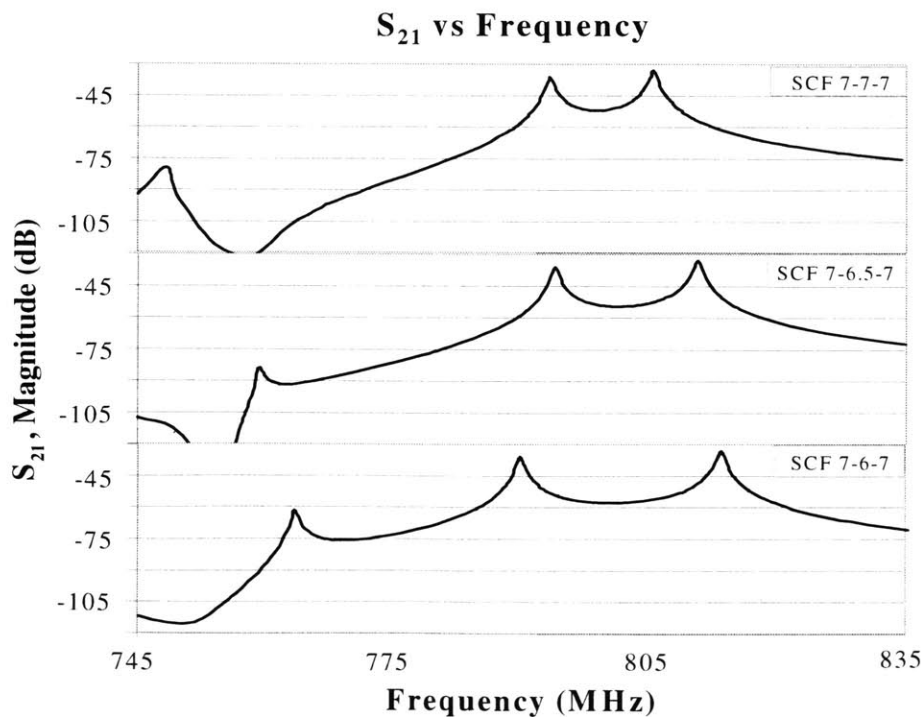

Figure 6.15: Transfer function progression with small changes to coupling tether length.

As the length changes from 7 μm to 6 μm, the peaks corresponding to the in-phase and out-of-phase modes drift apart. In one sense, this movement is beneficial because it produces a larger filter bandwidth. However, because the passband ripple also increases, the peaks begin to appear more like two distinct electrical responses, reducing the effectiveness of the filter. The three plots in Fig. 6.15 track the frequency shift and response increase of a lower spurious mode relative to the filter passband. For the inside tether length of 7 μm, the passband is relatively well isolated, having a response about 40 dB larger and 50 MHz higher than the corresponding spurious mode. For the 7-6-7 geometry, that same spurious mode is shifted 20 MHz closer to the filter passband and approximately 20 dB higher in magnitude. These results demonstrate that the inside tether length represents an important geometric parameter that can be manipulated to tune the filter's performance.

6.4.2 Comparison of Simulated SCF and Equivalent Circuit Model

Comparing the FEA model to its corresponding equivalent circuit provides information about how the mechanical effects of coupling can be represented in the electrical domain. As discussed earlier, the transfer function produced by the resonator bar can be reproduced by the BVD model, comprised of a series RLC combination in parallel with a through capacitance. Using a separate BVD circuit to represent each bar in the coupled configuration, the equivalent circuit model looks like Figure 6.16.

Circuit Parameters:
$V_{in} = 1$ V
$R_S = R_L = 50$ Ω
$C_0 = 7.075$ fF

$R = 2830.38$ Ω
$L_m = .5662$ mH
$C_m = .0707$ fF
$C_{coup} = .01 C_m$
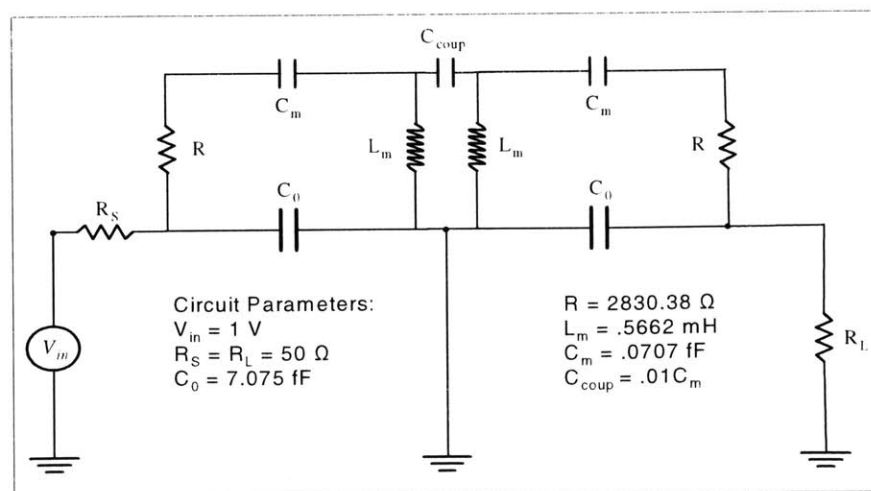
Figure 6.16: Equivalent circuit for coupled SCF configuration; coupling tether represented by coupling capacitor (C_{coup}).

In order to account for the effect of mechanical coupling in the device, the model of Fig. 6.12 is amended to include a passive capacitor element between the BVD circuits. The BVD element parameters are calculated by applying the technique of Ch. 5 to simulation data. The individual parameter values correspond to those for a 6 μm single bar. In the electrical domain, without the coupling capacitor (C_{coup}) present, the driven bar could not communicate with its counterpart. Therefore, C_{coup} serves as the electrical representation of the coupling between the bars through their common tether. Its value is found by fitting the simulation data generated from the SCF topology shown in Fig. 6.13. As the figure above indicates, in order to match the transfer function of the symmetric case, the value for C_{coup} should be approximately a hundred times smaller than the motional capacitance for a single bar. Figure 6.17 illustrates the effectiveness of the equivalent circuit to accurately reproduce the transfer function of the symmetric coupled geometry.
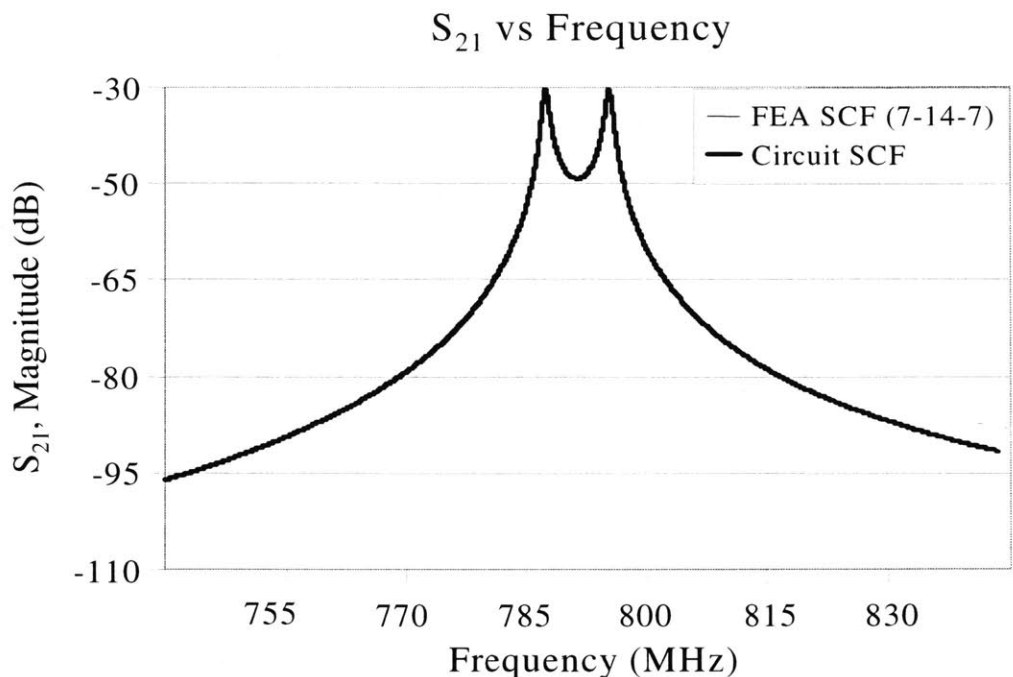
Figure 6.17: Comparison of transfer functions for SCF: Equivalent circuit vs. FEA.

In the equivalent circuit, C_{coup} is the only parameter available to change the coupling between the resonators. Changing the value of C_{coup} modifies the response bandwidth, and the latter can be tuned to fit any peak separation. In the structural FEA model, the coupling mechanism is much more complex, and, consequently, variations in the coupling tether length cause, not only

bandwidth changes, but also passband frequency shifts. Modifying the value of C_{coup} in the circuit model cannot account for frequency shifts such as these. In the BVD model, the resonant frequency of the circuit is proportional to the product of L and C. To accurately account for the frequency shift, the higher of the two longitudinal frequencies in the modal response is utilized to recalculate the BVD element parameters. With the appropriate value of L, C and C_{coup}, the circuit model of Fig 6.16 can be utilized to fit the simulation data of models with varied inside tether lengths.

For example, with respect to a SCF coupled geometry having inside and outside tether lengths of 7 μm, C_{coup} is increased to account for the change in bandwidth and the BVD parameters are recalculated to match the new frequency range of the passband. Relative to the symmetric geometry (7-14-7), the bandwidth of the 7-7-7 configuration increases about 4 MHz and the passband shifts approximately 10 MHz higher. The circuit model captures the increased bandwidth with a corresponding increase in the value of C_{coup}. In fact, the appropriate ratio of C_{coup} to C for a given geometry coincides closely with the ratio between the bandwidth and the resonant frequency of the filter. This trend is analogous to the relationship found by Clark [1] in the study of a three resonator micromechanical filter coupled with soft flexural-mode springs. This study demonstrated that the percent bandwidth (BW/ω_s) of the filter is proportional to the stiffness ratio between the resonators and the coupling springs. Table 6.3 shows this relationship for the circuit model of Draper's coupled resonator bar.

Coupling Tether Length (μm)	Ratio: Bandwidth To Resonant Frequency (%)	Ratio: C_{coup} To Motional Capacitance (%)
3.5	1.01	1.02
7.0	1.53	1.54
10.0	1.16	1.17
14.0	1.01	1.02
18.0	1.94	1.96
21.0	.97	.98

Table 6.3: Ratio of transfer function parameters (BW/ω_s) compared to ratio of circuit element parameters (C_{coup}/C). The ratio of capacitances in the circuit model is analogous to the stiffness ratio in [1].

The table shows that, relative to the symmetric case, the ratio of C_{coup} to C is increased to 1.5% to account for the larger bandwidth. This passband spans the frequency range from approximately 793.5 to 805.6 MHz. To account for this frequency shift, the motional inductance and capacitance of the BVD model are recalculated using the higher of the two frequencies. The transfer function of the modified circuit model is overlaid on the response of the corresponding FEA simulation in Figure 6.18.

S21 vs Frequency
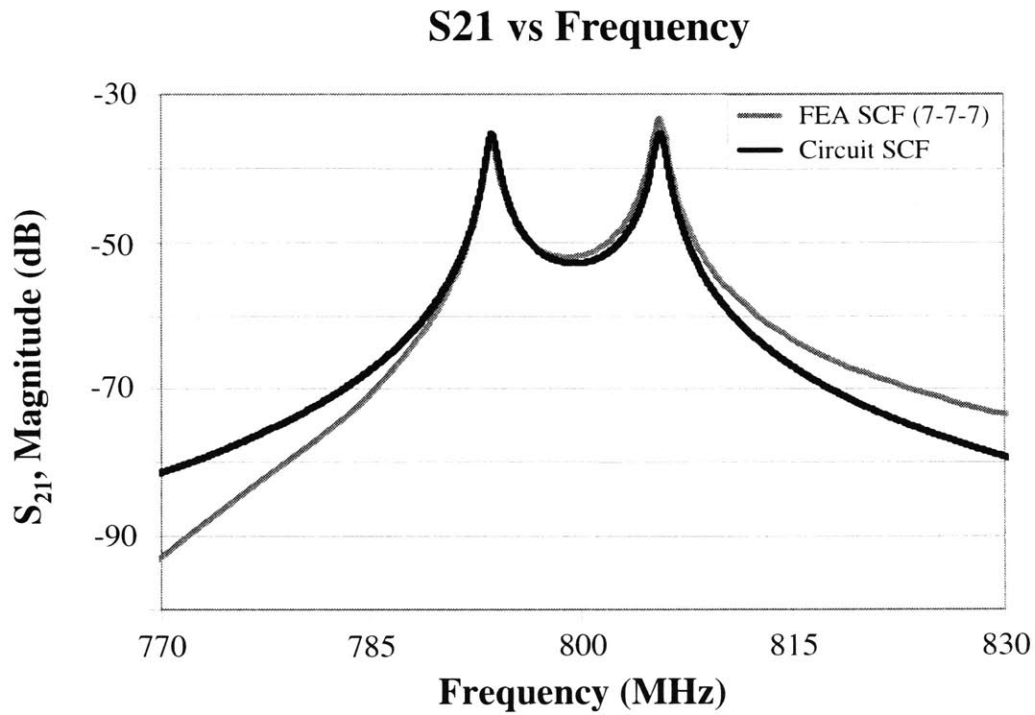
Figure 6.18: Circuit and FEA model transfer functions for a coupled SCF geometry with a modified coupling tether length (i.e. 7 μm).

[THIS PAGE INTENTIONALLY LEFT BLANK]

Chapter 7

Future Work and Conclusions

7.1 Optimization of Coupled L-Bar Stacked Crystal Filter

In Ch. 6, an equivalent circuit model was introduced and validated as a useful means of representing the electrical behavior of a coupled SCF. Using this equivalent circuit, the coupled design is now optimized, noting the modifications made to achieve the improved transfer function. The suggested source and load resistance values from [2] are used to obtain the optimum filter response. Furthermore, the passband ripple characterizing the unoptimized SCF configuration is eliminated by lowering the value of the coupling capacitor in the circuit model. Finally, because initial testing established the 10 μm bar as the most advantageous resonator geometry, the BVD model parameters introduced in Section 5.4 are used for the optimized SCF design. Applying these modifications to the SCF equivalent circuit of Fig. 6.16, the following model is obtained.


Circuit Parameters:
V_{in} = 1 V
R_S = R_L = 10R
C_0 = 15.35 fF

R = 1962.14 Ω
L_m = .6751 mH
C_m = .1695 fF
C_{coup} = .007C_m
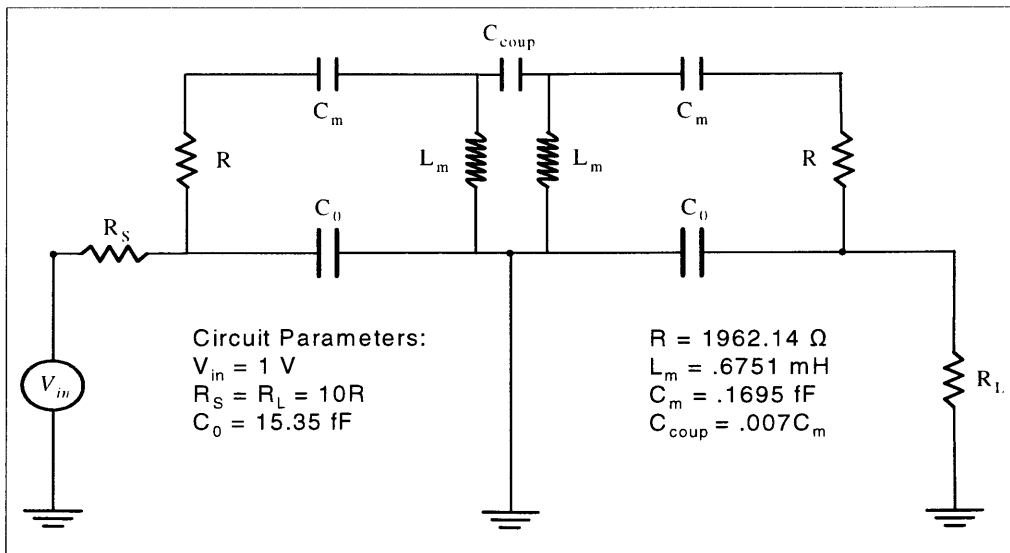
Figure 7.1: Optimized SCF equivalent circuit model with corresponding element values.

The modified equivalent circuit produces an optimized filter transfer function characterized by a flat passband response and an insertion loss of approximately 1.4 dB. Also, the percent bandwidth of the filter is 1% with a passband rejection of about 40 dB. The impedance at resonance is around 2 kΩ for an input mechanical Q of 1000. As a result, the source and load resistances, equal to 10 R, are not realizable values in an actual filter design. However, assuming the desired Q range (i.e. 10^4) for the resonator can be obtained, impedance matching with front end electronics will become more feasible. Figure 7.2 shows the response magnitude and phase angle of the optimized transfer function plotted versus frequency.
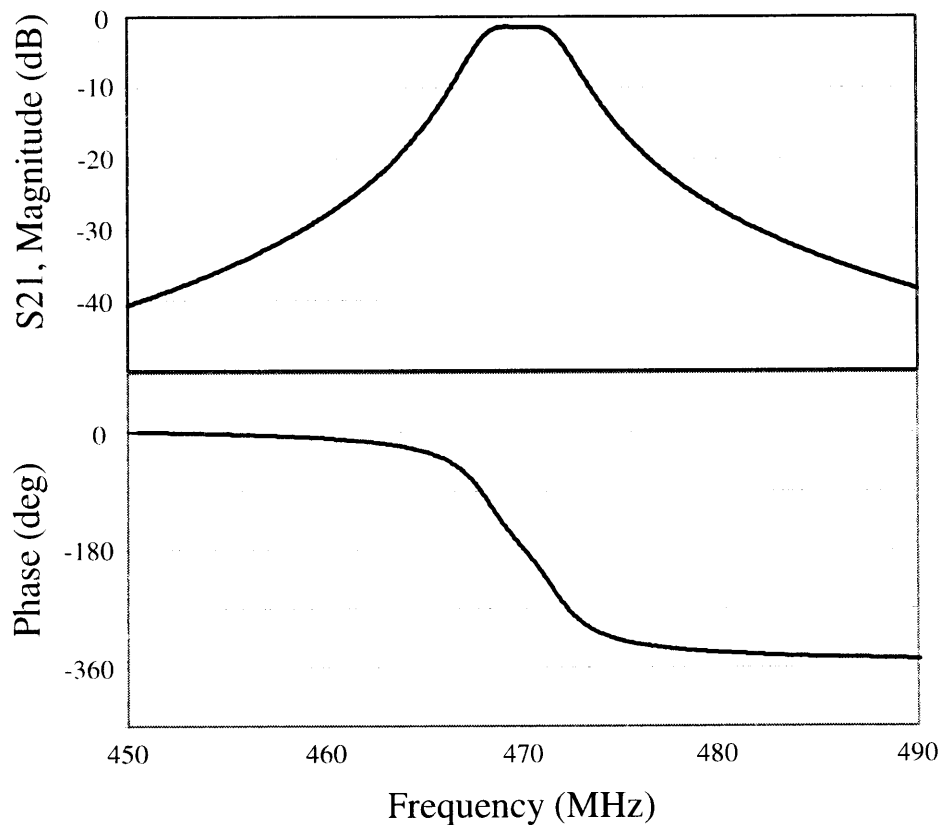
**Figure 7.2**: Circuit transfer function for optimized stacked crystal filter configuration. Circuit data obtained using BVD model parameters for 10x5 μm geometry.

In order to achieve the passband characteristic shown above, the value of C_{coup} is reduced by 30%. This decrease in the coupling between the individual BVD circuit components causes the peaks to shift closer together, and the passband flattens as a result.

Figure 7.3 illustrates this phenomenon by comparing the transfer functions of the standard symmetric geometry and the SCF model with reduced coupling.

S_{21} vs Frequency
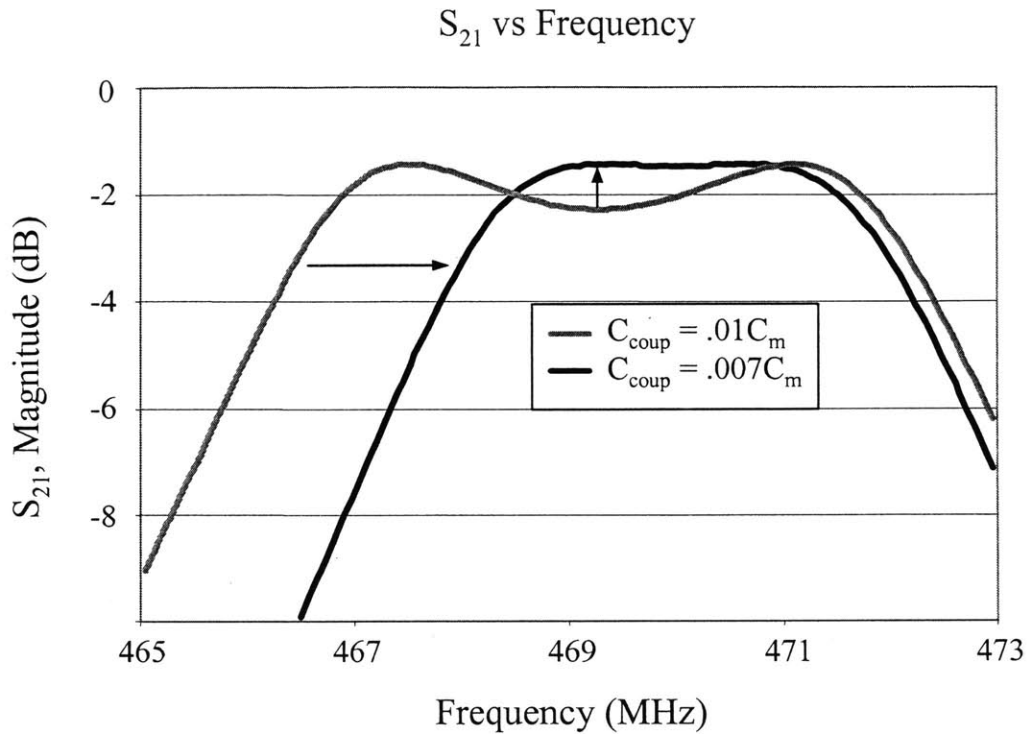
Figure 7.3: Zoomed view of original transfer function overlaid on the optimized passband response

Although reduced, the passband of the modified SCF design is more useful for filter applications because of its flattened response. Reducing C_{coup} in the electrical domain is analogous to decreasing the amount of mechanical coupling between the resonators. Therefore, in order to achieve smaller mechanical coupling in future coupled filter designs, physical modifications must be made to the inside tether connecting the resonators. The amount of mechanical coupling present in a design depends upon the ease with which longitudinal waves can travel through the common support tether. As a result, modifications to the filter geometry which discourage the formation of these waves could potentially reduce the coupling between the resonator bars. For example, a stress relief structure could be incorporated into the model to dissipate some of the energy transmitted by the tether waves. A structure such as this could be created by fabricating bends in the coupling tether. Other options include reducing the width of the coupling tether or fabricating a rigid structure to connect a portion of the tether to the substrate. Figure 7.4 gives

examples (top view) illustrating what each of the suggested geometries would look like after etching.
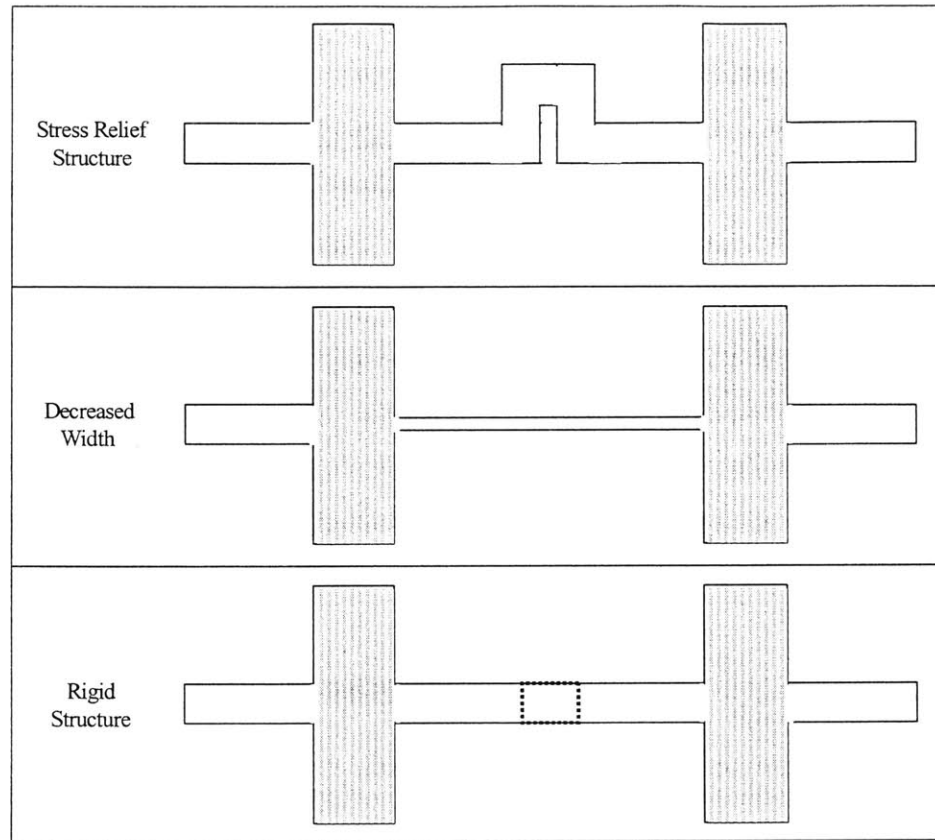
Figure 7.4: Examples of modified coupling tether geometries. Goal of modification is to reduce the mechanical coupling between the resonator bars.

7.2 Proposed SCF Geometry and Fabrication

Presently, Draper's fabrication and testing of the L-Bar resonator have been restricted to a single bar geometry. However, it is anticipated that future batches of the devices will include coupled designs, which may serve as both filters and filter components. Depending on their compatibility with current fabrication techniques, the suggested coupling tether modifications introduced in the preceding section can be implemented as necessary. The following is a proposed SCF topology

that can serve as a guideline for future coupled devices. Figure 7.5 illustrates the steps of the fabrication process.
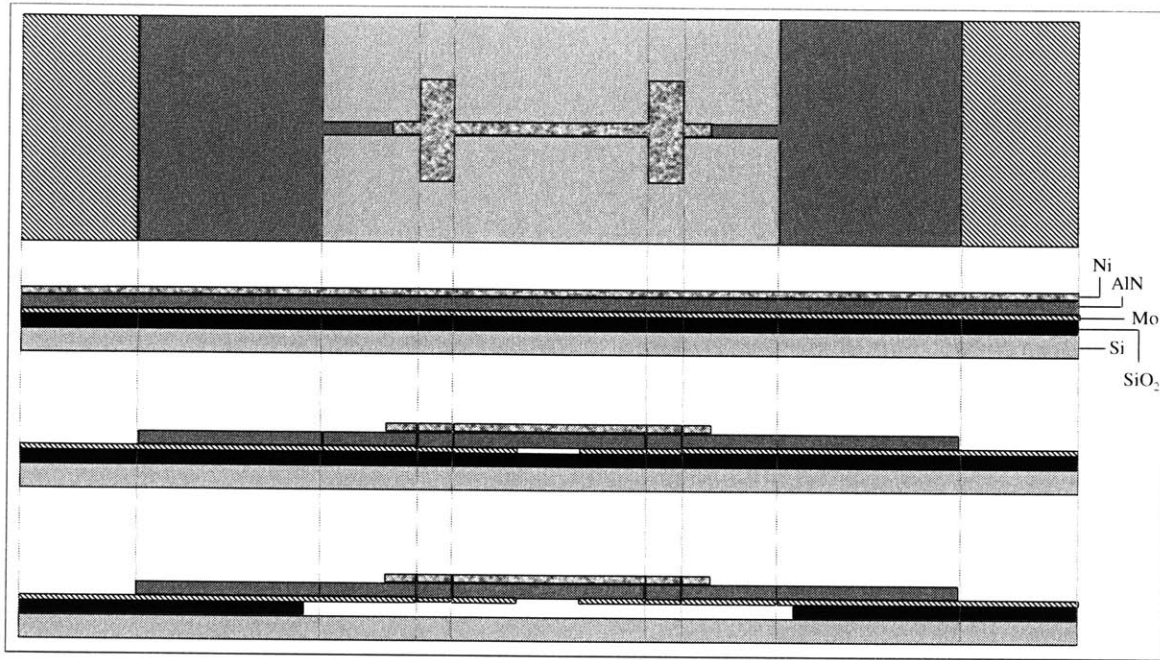
Figure 7.5: Steps for fabrication of coupled SCF topology. Top view is shown for reference. Side views show the progression of fabrication process.

The geometry shown in Fig. 7.5 combines the coupled bar design with the new 90 degree departure of the bond pads from the support tethers. The first profile view shows that the process begins with a multi-layered film. A metal-AlN-metal combination sits upon two layers of substrate. The silicon comprises the wafer base, while the silicon dioxide serves as the sacrificial layer eventually removed in order to release the device. The second profile view illustrates how the electrical circuit is patterned. Both the top metal (Ni) and AlN are removed at both ends of the structure to expose the bottom metal (Mo). Exposing the bottom metal on both sides facilitates the actuation and sensing of the device. A cut is made in the bottom metal between the resonators to electrically decouple them. Then, to complete the patterning of the electrical boundary conditions, a lead is used to connect the top metal to ground. These boundary conditions are slightly different from those applied to the FEA models of Ch. 6. For the simulated SCF geometries, a cut is made in the top surface and the entire bottom surface is grounded. For an actual device, inverting this set up reduces the probability of parasitic capacitances developing across the bond pads. The last step, as shown in the final profile view,

is to release the resonator bar and tether supports from the substrate. This is accomplished by etching away the sacrificial SiO_2 layer from beneath the device.

7.3 Conclusions

The purpose of this study was to show how mechanical coupling between MEMS L-Bar resonators could be utilized to achieve improved impedance characteristics for a range of UHF filter applications. FEA simulations were used to investigate this mechanical coupling. First, an analytical model and equivalent circuit were derived. The analytical derivation was then validated with an FEA model having the same material properties and boundary conditions. The center frequency and resonant impedance produced by the FEA model was within 1% of the analytical values. For further investigations, the FEA model was modified to include both the resonator bar and its tether supports.

Compared to an actual device, this geometry including tethers is relatively simple, not accounting for any of the filter's substrate or packaging. As a result, a boundary condition study was undertaken to determine the sensitivity of the L-Bar model to changes in the peripheral geometry and displacement constraints. This case study provided information about the range of error associated with the simple resonator-tether model. A table was generated comparing the transfer function parameters of resonator geometries with various boundary conditions. The longitudinal center frequencies of the different models fell in a narrow range, and the resonant impedance of the simple model was within a factor of four or less of the other values. Therefore, the comparison of FEA results demonstrated that the simple model yielded impedance and center frequency values comparable to those of more complex geometries. Despite these similarities, the more complex models did produce a greater number of spurious modes than the simple geometry. However, due to an inability to reproduce the exact boundary conditions of the real device, it was decided that the presence and significance of spurious modes would ultimately have to be determined by experimental means. Taking this into consideration, initial experimental results from an actual resonator were compared to the transfer function of a simple 10x5 μm model including metal electrodes. With respect to resonant frequency, impedance, and

the nature of spurious modes, the simulated electrical output corresponded well to the actual transfer function.

With the simple model qualified as a suitable FEA geometry, a technique was introduced that outlined a method for calculating the parameters of the Butterworth van Dyke (BVD) circuit model from simulated (or measured) transfer function data. This technique was tested on simulation data for which a mechanical Q had been designated. As a consistency check, the input mechanical Q was compared to the extracted Q for a range of values. The percent error between the two Q values was found to be minimal for all cases. Consequently, it was demonstrated that an effective circuit model could be developed from transfer function data. Further testing of the method on actual S_{21} data was hindered by the presence of electrical parasitics, which contribute significantly to the transfer function of a real device. However, this parameter extraction technique can serve as a foundation for future efforts to develop a more comprehensive circuit model.

In the final chapter, a new resonator topology was presented. This topology employs mechanical coupling between L-Bar resonators to improve upon the output of a single bar, and offer alternative configurations for filter design at Draper. The new coupled geometry can be configured as either a single-port resonator or a multi-port filter. If used as a resonator, the single-port mechanically coupled configuration with parallel electrical boundary conditions provides virtually the same transfer function as a single bar, with half the impedance at resonance. If the coupled bar is designed to operate as a filter, it provides a geometry that is more robust and offers a wider bandwidth than uncoupled topologies. In the discussion of future work, optimized filter parameters were presented, and suggestions were provided for achieving these values. Furthermore, the process for fabricating a stacked crystal filter geometry was outlined, thus establishing a guideline that will facilitate efforts to improve upon current UHF filter designs at Draper.

[THIS PAGE INTENTIONALLY LEFT BLANK]

Appendix

Finite Element Analysis in ANSYS

This section provides a general overview of the finite element modeling process using ANSYS. The steps for modeling a piezoelectric resonator bar with tether supports are outlined. The descriptions given below provide insight into the procedure for finite elements based analysis and demonstrate the comprehensive nature of electromechanical modeling in ANSYS. The general modeling process is divided into three main parts: preprocessing, solution, and post-processing.

Preprocessing

- Define model geometry including dimensions and coordinate system. For consistency with the analytical model, resonator length is aligned with x_1 and tether length with x_2. Also, Boolean operations (i.e. adding/gluing volumes, areas, etc) are performed to combine resonator and tethers into a single geometry.

- Choose element types. A piezoelectric block element is chosen along with the circuit elements (i.e. source/load resistors, coupling capacitor, etc.) used in the harmonic analysis.

- Define material properties – density, orthotropic stiffness and piezoelectric constants, and isotropic dielectric value.

- Define real constants – values for passive circuit elements. Only necessary in harmonic analysis because circuit elements are not compatible with modal solver.
    - For a MEMS component, both material property values and real constants should be scaled to account for the micrometer dimensions of the geometry.

- Mesh model geometry. Area and line element divisions are designated to define the mesh density. Because linear block elements are used, the mesh through the model thickness should be comprised of at least three element layers and the element aspect ratio (i.e. length/thickness) should not exceed five.

- Apply boundary conditions – mechanical and electrical
    - Mechanical – finite element displacement constraints are imposed on the tether ends. Nodes on the cross-section of the tethers are fixed in the y-direction. A stress free boundary condition exists on all other surfaces.
    - Electrical – nodes along the top and bottom surfaces of the geometry are grouped into separate coupled sets. Top reference node is given a value of 1 V and bottom reference node is grounded.

Solution

- Choose analysis type – modal or harmonic.

- Modal analysis yields the mode shapes and corresponding resonant frequency values of the geometry. The modal extraction method is Block Lanczos and the analysis range is defined by a starting and ending frequency – these values are on the order of a GHz for the MEMS geometry.

- Harmonic analysis produces the electrical transfer function of the model. The harmonic solution method is designated as "full" and a sparse equation solver is used. Solver parameters include the frequency sweep range and the number of sub-steps to be analyzed within that range. A greater number of sub-steps results in a finer frequency sweep – the frequency step is the smallest when sweeping across the primary mode (i.e. longitudinal) of the geometry. The individual values of the harmonic sweep represent the frequencies of the sinusoidal potential function used to drive the model. The magnitude of the forcing function is 1 V.

Post-Processor

- Choose post-processor type – general or time.

- General post-processor is used for reviewing the modal analysis results. The mode shapes of the geometry are animated and the longitudinal mode is identified by its displacement and frequency. The modal frequencies are then input into an array, which is used in the harmonic analysis.

- The time post-processor is employed to determine the electrical response of the geometry as it varies with frequency. The charge is calculated as the reaction force at the driven reference node on the top surface of the model. The charge is then multiplied by the frequency to obtain a value for the current produced in the device. The impedance is calculated as the drive voltage (i.e. 1 V) divided by the current, and the transfer function is generated by graphing the impedance versus frequency. If an S-parameter transfer function is desired, the voltage across the load resistor is obtained instead of the charge. The output voltage ratio, calculated as the reciprocal of this load resistor voltage, is used to determine the corresponding S_{21} values.

References

[1]   Nguyen, C.T.C., "Frequency-Selective MEMS for Miniaturized Low-Power Communication Devices," *IEEE Transactions on Microwave Theory and Techniques,* Vol. 47, No. 8, Aug. 1999, pp. 1486-1503.

[2]   Kang, J., "Piezoelectric MEMS Resonator Characterization and Filter Design," The Charles Stark Draper Laboratory, Inc., CSDL-T-1469, Cambridge, MA, March 2004.

[3]   Diamantis, S., Ahmadi, M., Jullien, G.A., and Miller, W.C., "A Programmable MEMS Bandpass Filter," *Proceedings of the Forty-Third Midwest Symposium on Circuits and Systems,* IEEE, Lansing, MI, Aug. 2000, pp. 522-525.

[4]   Nilsson, J.W., Electric Circuits, 3rd Ed., Addison-Wesley, Reading, MA, 1990, pp. 506-509.

[5]   Antkowiak, B., Gorman, J.P., Varghese, M., Carter, D.J.D., and Duwel, A.E., "Design of a High-Q, Low-Impeance, GHz-range Piezoelectric MEMS resonator," *The 12th International Conference on Solid-State Sensors, Actuators, and Microsystems (Transducers),* Boston, MA, June 2003, pp. 841-846.

[6]   Demirci, M.U., Abdelmoneum, M.A., Nguyen, C.T.C., "Mechanically Corner-Coupled Square Microresonator Array for Reduced Series Motional Resistance," *The 12th International Conference on Solid-State Sensors, Actuators, and Microsystems (Transducers),* Boston, MA, June 2003, pp. 955-958.

[7]   Lakin, K.M., "Bulk Acoustic Wave Coupled Resonator Filters," *International Frequency Control Symposium and PDA Exhibition,* IEEE, 2002, pp. 8-14.

[8]   Lakin, K.M., Belsick, J., McDonald, J.F., and McCarron, K.T., "High Performance Stacked Crystal Filters for GPS and Wide Bandwidth Applications," *Ultrasonics Symposium,* IEEE, 2001, pp. 833-838.

[9]   Carter, D.J.D., Kang, J., White, D., Duwel, A.E., "Fabrication and Measurement of an IC-Compatible GHz-Range Piezoelectric Longitudinal Bar Resonator," *Solid-State Sensor, Actuator, and Microsystems Workshop,* Hilton Head, South Carolina, June 6-10 2004.

[10]   Lakin, K.M., "Modeling of Thin Film Resonators and Filters," IEEE MTT-S International Microwave Symposium Digest, Albuquerque, NM, pp. 149-152., June 1992.

[11] Lakin, K.M., Kline, G.R., McCarron, K.T., "High-Q Microwave Acoustic Resonators and Filters," *IEEE Transactions on Microwave Theory and Techniques*, Vol. 41, No. 12, Dec. 1993, pp. 2139-2145.

[12] Lakin, K.M., Kline, G.R., McCarron, K.T., "Development of Miniature Filters for Wireless Applications," *IEEE Transactions on Microwave Theory and Techniques*, Vol. 43, No. 12, Dec. 1995, pp. 2933-2939.

[13] Bannon III, F.D., Clark, J.R., and Nguyen, C.T.C., "High Frequency Microelectromechanical IF Filters," IEEE, Univ. of Mich, Ann Arbor, MI, 1996.